TESTS FOR DETERMINING FAILURE CRITERIA
OF CERAMICS UNDER BALLISTIC IMPACT

Final Report

Richard W. Klopp, Research Engineer III
Donald A. Shockey, Associate Director
Poulter Laboratory

June 1992

U.S. ARMY RESEARCH OFFICE

Contract Number DAAL03-88-K-0200

SRI International
333 Ravenswood Avenue
Menlo Park, CA 94025-3493

DTIC
SELECTE
OCT 22 1992
S D

92-27560

THE VIEW, OPINIONS, AND/OR FINDINGS CONTAINED IN THIS
REPORT ARE THOSE OF THE AUTHOR(S) AND SHOULD NOT BE
CONSTRUED AS AN OFFICIAL DEPARTMENT OF THE ARMY
POSITION, POLICY, OR DECISION, UNLESS SO DESIGNATED BY
OTHER DOCUMENTATION.

REPORT DOCUMENTATION PAGE

Public reporting burden for this collection of information is estimated to average 1 hour per response, including the time for reviewing instructions, searching existing data sources, gathering and maintaining the data needed, and completing and reviewing the collection of information. Send comments regarding this burden estimate or any other aspect of this collection of information, including suggestions for reducing this burden, to Washington Headquarters Services, Directorate for Information Operations and Reports, 1215 Jefferson Davis Highway, Suite 1204, Arlington, VA 22202-4302, and to the Office of Management and Budget, Paperwork Reduction Project (0704-0188), Washington, DC 20503

1. AGENCY USE ONLY (Leave blank)	2. REPORT DATE June 1992	3. REPORT TYPE AND DATES COVERED Final Technical Report, 10/01/88 to 02/29/92

4. TITLE AND SUBTITLE

Tests for Determining Failure Criteria of Ceramics under Ballistic Impact

5. FUNDING NUMBERS

DAAL03-88-K-0200

6. AUTHOR(S)

Richard W. Klopp and Donald A. Shockey

7. PERFORMING ORGANIZATION NAME(S) AND ADDRESS(ES)

SRI International
333 Ravenswood Avenue
Menlo Park, CA 94025-3493

8. PERFORMING ORGANIZATION REPORT NUMBER

SRI Project 6795

9. SPONSORING/MONITORING AGENCY NAME(S) AND ADDRESS(ES)

U.S. Army Research Office
P.O. Box 12211
Research Triangle Park, NC 27709-2211

10. SPONSORING/MONITORING AGENCY REPORT NUMBER

ARO 26173.4-MS-A

11. SUPPLEMENTARY NOTES

12a. DISTRIBUTION/AVAILABILITY STATEMENT

Approved for public release; distribution unlimited.

12b. DISTRIBUTION CODE

13. ABSTRACT *(Maximum 200 words)*

A three-year Balanced Technology Initiative (BTI) program to develop tests for determining the failure criteria of ceramics under ballistic impact is described. The phenomenology of the penetration of a confined ceramic block by a long rod penetrator was established by examining the fracture damage in targets after ballistic testing. The material properties that govern the penetration resistance of ceramics were deduced. Two plate impact tests—the high-strain-rate pressure/shear test and the symmetric pressure/shear test—were then developed to measure the granulation and granular flow properties of candidate armor ceramics at strain rates and pressures representative of those at the tip of an advancing penetrator. In the development of the tests, a laser-Doppler velocimeter was applied for the first time to measure the transverse motion of the target plate. The tests were applied to aluminum nitride, boron carbide, and Coors AD-85 and AD-995 aluminas; and the resultant behaviors were compared. Two one-dimensional computational models, one based on a continuum Mohr-Coulomb description of the flow of granulated ceramic and the other (developed in a companion BTI project) based on the frictional sliding of blocks, were applied to interpret the symmetric pressure/shear tests, which revealed the near-penetrator failure behavior. The observations and data were used as input for two-dimensional penetration simulations using the block-sliding model.

14. SUBJECT TERMS			15. NUMBER OF PAGES 154
Ceramic armor Long rod penetrator	Mescall Zone Pressure-shear tests	Balanced Technology Initiative	16. PRICE CODE

17. SECURITY CLASSIFICATION OF REPORT	18. SECURITY CLASSIFICATION OF THIS PAGE	19. SECURITY CLASSIFICATION OF ABSTRACT	20. LIMITATION OF ABSTRACT
UNCLASSIFIED	UNCLASSIFIED	UNCLASSIFIED	UNCLASSIFIED

CLASSIFIED BY:

DECLASSIFY ON:

SUMMARY

The objectives of this three-year Balanced Technology Initiative program were to identify the material properties that govern the resistance of ceramics to penetration, develop tests for measuring these properties, and apply the tests to evaluate several ceramics that are candidates for armor application. This information is needed to design armor structures that can protect against advanced penetrators.

To identify the material properties governing penetration resistance, we needed to understand how ceramics resist penetration and how they fail. We sought this information by examining ceramic armor targets that had been penetrated or partially penetrated and reached the following conclusions:

- Penetration of a confined ceramic block by an impacting long rod projectile occurs by the comminution of a zone of the ceramic at the leading edge of the projectile and the flow of the fine fragments out of the projectile path. (We named this zone the Mescall zone in recognition of John Mescall, who postulated its existence based on his hydrocode calculations in the 1980s.)

- The material properties governing the penetration resistance of a confined ceramic block include the dynamic compressive strength, the comminution and granular flow resistance under high rate and high pressure conditions, and the abrasiveness of the ceramic fragments.

To develop tests for measuring these properties, we sought ways to produce conditions of stress, strain, and strain rate representative of those produced during penetration. By performing hydrocode calculations of simulated penetration scenarios, we found that stresses of several tens of kilobars and strain rates of 10^5/s were typical. We then analyzed several types of tests that produce appropriate conditions to determine their suitability for providing the granulation and flow properties of candidate armor ceramics. We chose three tests as most promising: (1) high strain-rate pressure/shear plate impact, (2) symmetric pressure/shear plate impact, and (3) explosively loaded contained rod impact.

We performed the high strain-rate pressure/shear (HSRP/S) plate impact test by impacting a thin specimen plate against a hard anvil plate inclined at an angle. This thin specimen plate was backed up by a thick, hard flyer plate, which created a state of high pressure and high shear strain rate in the specimen. The flyer and anvil plates were designed to remain

iii

elastic while the specimen deformed. During the early stages of the test, before release waves reach the center of the plate from the periphery, stress components in the specimen were inferred from the projectile velocity and particle velocities at the rear surface of the anvil. Thus, measuring particle velocity history at the rear surface allowed us to construct a shear stress-shear strain curve. The HSRP/S test was adapted to test aluminum nitride by substituting boron carbide for the usual steel flyers and anvils. The transverse particle velocity at the rear surface of the anvil was monitored by using a transverse displacement interferometer, which uses the interference of light beams of different Doppler-shifted frequencies to indicate the transverse velocity.

The HSRP/S test could not be used for specimens of the very strongest ceramics, such as SiC, B_4C, and TiB_2, because even stronger materials such as diamond or cubic boron nitride are required for the flyers and anvil plates. The second test method, the symmetric pressure/shear (SP/S) test, circumvented this requirement by impacting a ceramic anvil in a pressure/shear configuration with a flyer composed entirely of the same ceramic. In this test the impact velocity and angle and the histories of normal and transverse particle velocity at the target rear surface were measured. These histories were compared with those from a numerical simulation using a postulated material model, which was iteratively modified until the experiment and the simulation agree. If the match is good, the model is at least valid for the test conditions. The SP/S test is not so easy to analyze as the HSRP/S test and provides the shear stress-strain curve only indirectly, but it nevertheless allows very strong ceramics to be evaluated under conditions of high confining pressure and strain rate representative of armor penetration.

The SP/S test was applied to aluminum nitride, boron carbide, and Coors AD-85 and AD-995 aluminas. In our adaptation of the test, the transverse rear-surface particle velocity of the target plates was measured by using a laser-Doppler velocimeter (LDV) rather than a transverse displacement interferometer. To our knowledge, this is the first application of LDV in shock physics experiments. The LDV has the advantage of not requiring a diffraction grating on the rear surface of the target; a diffraction grating is difficult and expensive to etch onto ceramic, but it is required (and must survive shock loading) when using the traverse displacement interferometer.

We tried several rod impact configurations in an attempt to develop a test simpler than the pressure/shear tests. Ceramic rods were surrounded by metal or plastic containment and impacted axially with explosively driven flyer plates. The confinement successfully elevated the mean stress in the deforming ceramic. Unfortunately, we were unsuccessful in recovering the

rods or containment to measure posttest deformation. Although some contained-rod impact configuration could be made to work, we did not pursue this problem further.

Both types of pressure/shear experiments revealed a wide range of mechanical response among the ceramics tested. The transverse velocity for AlN nearly reached the elastic level, whereas the velocity for B_4C was only 35% of the elastic level. For AlN and B_4C, velocities decayed with time; for AD-85 and AD-995 Al_2O_3, velocities increased with time. The former behavior is characteristic of faster decay waves overtaking the initial shear wave from behind, whereas the latter behavior is characteristic of slower following waves. The different ceramics seem to have different mechanisms for failure and postfailure flow, and these mechanisms operate at different threshold loads.

Two one-dimensional computational models were developed to infer strength behavior from the symmetric pressure/shear particle velocity records. One model is based on a continuum Mohr-Coulomb description of the flow of granulated ceramic, and the other is based on frictional sliding of blocks. With the exception of AlN tested in SP/S, the shear strengths inferred from the pressure/shear tests were lower than the strengths reported by others. We think the reason is that we have essentially measured the response of comminuted ceramic, which may be appropriate for evaluating materials for armor applications. The longitudinal wave, which is strong enough to cause damage even in compression, runs ahead of the shear wave. The shear wave, which we measured, is always running through damaged material.

The Mohr-Coulomb simulations reproduced the transverse velocity histories at least qualitatively and, in the cases of AlN tested in HSRP/S and AD-85 and AD-995 Al_2O_3 tested in SP/S, quantitatively. The simulations were able to predict the SP/S response of AD-995 from the SP/S response of AD-85, but were unable to predict the SP/S response of AlN from the HSRP/S results. We concluded that the results of the computations are valid at least (perhaps only) for the conditions of a given test. Further work is needed to refine these models.

We established at the outset that any tests for measuring the ballistic behavior of armor ceramics must measure their behavior under penetration conditions. Both the HSRP/S and SP/S tests have met this requirement, because mean stresses and strain rates characteristic of the Mescall zone were achieved in both. Thus we conclude that pressure/shear tests in these two configurations with rear surface laser diagnostics and with appropriate constitutive analysis are suitable for measuring the high pressure, high strain rate comminution and granular flow properties of armor ceramics.

Future work should focus on resolving certain measurement issues in the tests and refining the simulation models. Further work is also needed to design a simple, inexpensive test for examining ceramics under penetration conditions. Although the pressure/shear tests described here were successful, they require a sophisticated gas gun facility with accompanying interferometers and high-speed recording equipment. We recommend that the search for a simpler test begin with investigation of the cylindrical cavity expansion test. A simpler static test may be possible, if a large enough mean stress can be applied, but a dynamic test may be necessary to produce such a large mean stress.

CONTENTS

ILLUSTRATIONS

TABLES

ACKNOWLEDGMENTS

Chapter 1

INTRODUCTION

Armors that incorporate ceramics are known to provide higher resistance to penetrators than metallic armors. However, designing armor packages having optimal performance is difficult because the reasons for the enhanced ballistic protection are only partly understood. To attain the information necessary to design superior armor, new tests are needed that measure the ceramic properties that govern penetration resistance. Simple ballistic tests can only rank the various ceramics and armor configurations; they do not provide the information necessary to guide the development of ceramic microstructures or armor geometries.

OBJECTIVES

The objectives of this project were to identify the material properties that govern the resistance of ceramics to penetration, develop tests for measuring these properties, and apply the tests to evaluate several candidate ceramics.

APPROACH

As the first step, we sought to understand the phenomenology of failure under ballistic penetration conditions. After reviewing the classified and unclassified literature to assess the current knowledge, we obtained penetrated and partially penetrated ceramic armor targets (in conjunction with a related, parallel project[1]) and sectioned and examined them to determine the mechanisms of penetration. We then performed hydrocode calculations of ceramic armor penetration to determine the conditions of stress, strain, and strain rate produced during penetration. These calculations were necessarily qualitative because accurate material models, a goal to be attained at the end of the project, were unavailable.

Once the mechanisms and conditions of failure and postfailure flow were determined, we began to consider test techniques that could invoke the salient material failure mechanisms under representative load conditions in well-controlled ways. We further considered diagnostic techniques that could measure the governing stress, strain, and strain rate variables. Given the high deformation rates involved in penetration, our attention naturally focused on impact and

1

explosive loading tests. We analyzed several candidate tests, including normal and slanted plate impact, rod impact, and cylindrical cavity expansion.

We chose three candidate tests as the most promising: (1) high strain-rate pressure/shear plate impact, (2) symmetric pressure/shear plate impact, and (3) explosively loaded contained rod impact. We implemented each test and, from the results, decided whether to pursue each technique further. We had the most success with the pressure/shear tests and so applied most of our developmental effort to them.

In Chapter 2, we present a qualitative and quantitative picture of the conditions ahead of an advancing penetrator. In Chapter 3, we describe the high strain-rate and symmetric pressure/shear techniques and the analyses used to extract the data. Next, we present the results of tests on aluminum nitride (AlN), two grades of alumina (Al_2O_3), and boron carbide (B_4C), followed by a comparison of these results with those obtained by others using different testing techniques and with results obtained for silicon carbide (SiC). In Chapter 4, we describe the other candidate tests considered and present simple analyses of them. We also describe a brief investigation we undertook on penetrator erosion phenomenology. Conclusions and recommendations are presented in Chapter 5. The Appendix contains copies of papers we published on this project, along with a list of presentations.

Chapter 2

PENETRATION PHENOMENOLOGY

QUALITATIVE PENETRATION CONDITIONS

When an approaching penetrator initially contacts a block of ceramic, a dynamic Hertzian contact stress wave field is generated. The material's ability to resist this initial part of the attack is therefore governed by its dynamic hardness.[2] If the penetrator can apply more stress than the strength associated with the dynamic hardness of the target, it will advance into the ceramic. Further advance requires that the ceramic be moved out of the penetrator path. In metal armor, most of this movement is accommodated by dislocation plasticity, but in ceramics, although the initial movement may be accompanied by dislocation plasticity,[3] too few slip systems are available for sustained plasticity. Therefore, the large deformations required to move material out of the penetrator path are accommodated by the sliding and flow of microscopic fragments.[2] Thus, the material's ability to resist granulation is an important material property, as is its ability to resist granular flow.

For continued penetration through a thick, well-confined block of ceramic, the material ahead of the penetrator must be moved laterally, then opposite the direction of attack. In steady-state penetration, the fine ceramic fragments produced in the "Mescall" zone at the tip of the penetrator[4-6] (Figure 1) flow out of the penetrator's path. To an observer traveling with the interface between the penetrator and the ceramic (which may not be a sharp boundary), a stream of comminuted ceramic appears to approach, then divide and bypass the observer's position. Likewise, penetrator material appears to approach from behind, divide, and reverse direction as the penetrator is eroded. The deformation of penetration is expected to occur under conditions of high mean stress and high strain rates. Any tests for measuring the failure criteria of ceramic under ballistic penetration must exercise the material under such conditions. In this work, we concentrated on the material properties that govern the steady-state phase of penetration, namely, granulation and granular flow properties.

3

Impact Surface
Ejecta

Comminuted
" Mescall" Zone
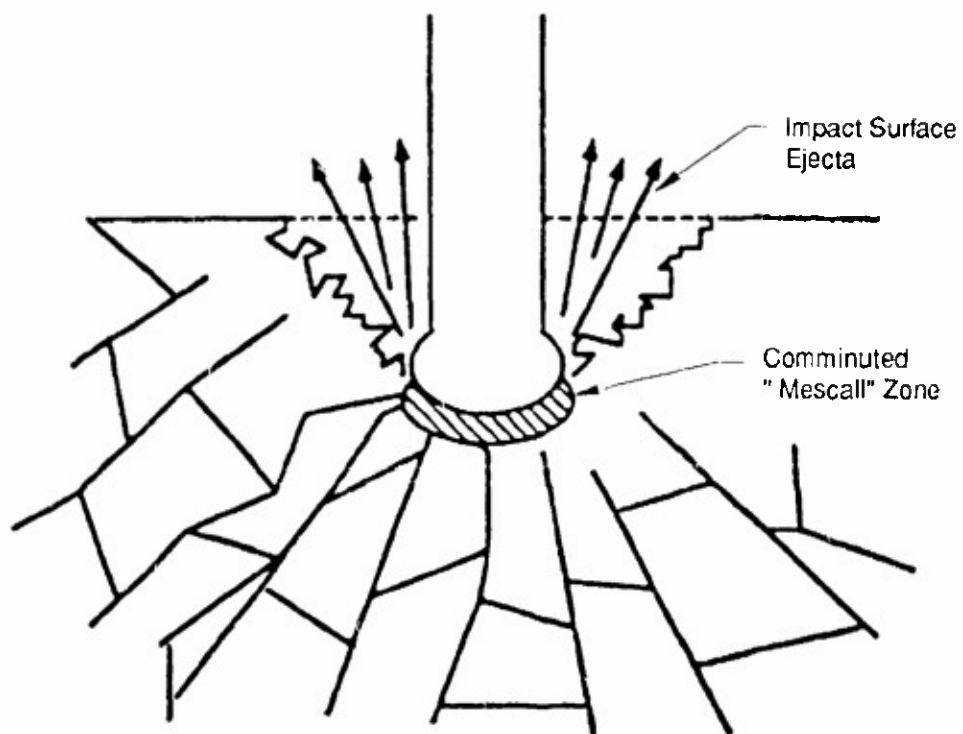
RM-7525-8

Figure 1. Cracking pattern in ceramic targets during the steady-state phase of
the penetration process.

4

QUANTITATIVE PENETRATION CONDITIONS

To fail and deform well-confined ceramic requires that a stress on the order of that required for yielding in uniaxial strain compression [i.e., the Hugoniot elastic limit (HEL)] be exceeded. To obtain a quantitative estimate of the conditions ahead of a penetrator, we used the model of Curran et al. for the motion of granular beds[4] in Cooper's two-dimensional Lagrangian hydrocode[7] and simulated the penetration of a 1.6-km/s tungsten rod into a block of aluminum nitride. The resulting contour plots of mean stress and effective strain rate are shown in Figure 2. Essentially, a material element ahead of a penetrator is deformed at a strain rate greater than 10^5 s^{-1} while under a mean stress of order of the HEL, 9 GPa[8] in this case. The results in Figure 2 are not strongly dependent on the details of the tungsten and ceramic material models.

The details of the loading path for a material element are complex, and complex loading paths induce complex responses, such as anisotropy, in the ceramic. In this work, the effects of complex loading paths are considered secondary. We attempted to develop tests that could duplicate simply the mean stress, strain rate, and strain conditions of penetration.
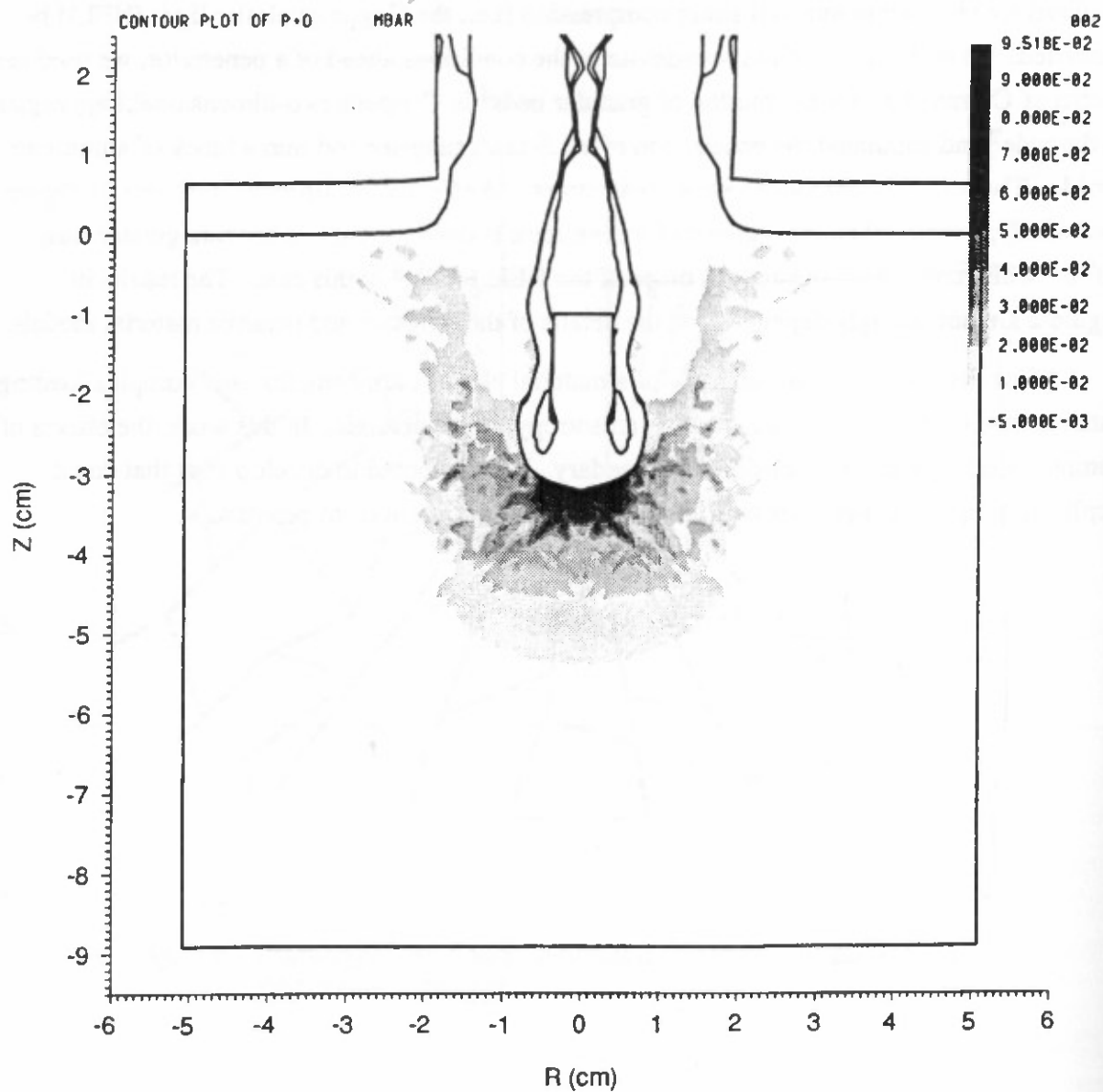
(a) Mean stress contours

RA-6795-36

Figure 2.   Simulation of 1.6-km/s tungsten rod penetrating confined AℓN.

6

CONTOUR PLOT OF EFFECTIVE SRATE 1/US

| | 004 |
| 4.493E-01 |
| 4.000E-01 |
| 3.500E-01 |
| 3.000E-01 |
| 2.500E-01 |
| 2.000E-01 |
| 1.500E-01 |
| 1.000E-01 |
| 5.000E-02 |
| 2.377E-05 |
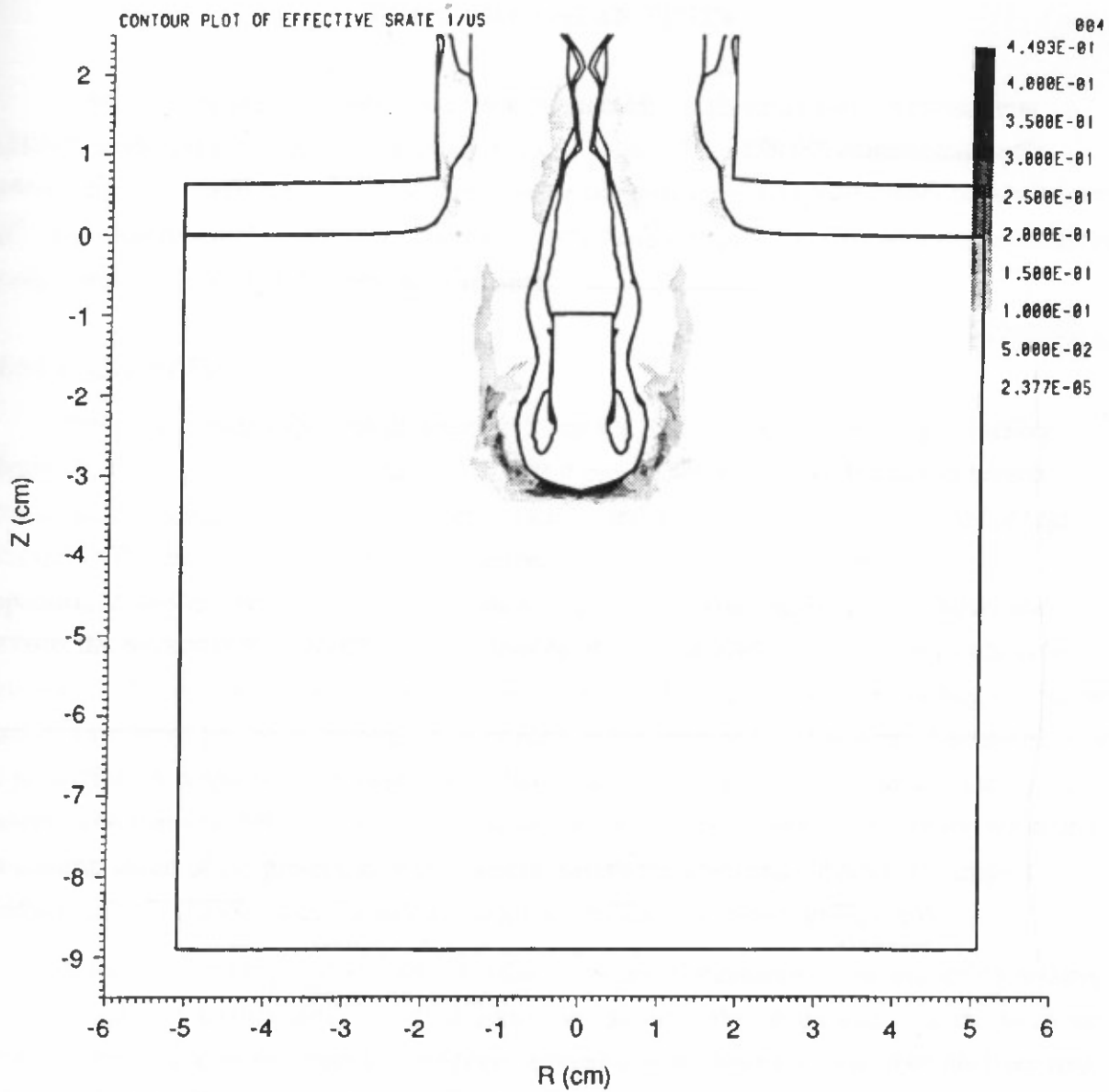
(b) Effective strain rate contours

RA-6795-37

Figure 2.   Simulation of 1.6-km/s tungsten rod penetrating confined A ℓ N. (concluded)

7

Chapter 3

PRESSURE/SHEAR TESTS

Two types of pressure/shear tests were conducted: high-strain-rate pressure/shear (HSRP/S) tests and symmetric pressure/shear (SP/S) tests. The HSRP/S experiments were performed on AlN, and the SP/S experiments were performed on AlN, two grades of Al_2O_3, and B_4C. The experimental results were compared with those obtained for SiC, with results obtained by other workers, and with ballistic performance.

GENERAL EXPERIMENTAL SETUP

The plate impact experiments were performed at SRI's $2\frac{1}{2}$-inch-bore gas gun facility (Figure 3). This gun is capable of launching 230-g projectiles to 1 km/s. It has two breech mechanisms: a wraparound type for lower velocities and a rapid-opening-valve type for high velocities. The breech mechanisms are described by Erlich[9] in a publication included in the Appendix. A key on the side of the projectile engages a slot broached in the gun barrel and prevents the projectile from rotating, thus allowing oblique/parallel impact experiments to be performed. The velocity of the projectile is measured just before impact by recording the contact times of four wires placed in its path. A flyer plate in the form of a disk is carried on the nose of the projectile. A target or anvil plate, also a disk, is situated in an evacuated tank at the gun's muzzle. The tank and barrel are evacuated to below 100 mTorr to prevent the compression of a gas column ahead of the projectile, which would disturb the anvil and lubricate the impact interface. The HSRP/S projectile and the target assemblies are shown in Figure 4.

In the experiments reported here, the diameters and thicknesses of the impacting ceramic plates were chosen so that the first unloading wave to arrive at the center was from the anvil rear surface. The release waves from the periphery arrived slightly later and that from the flyer free surface still later. The flyer, anvil, and (in the case of HSRP/S) specimen plates were made flatter than 0.6 μm over a 40-mm diameter to ensure wave planarity.
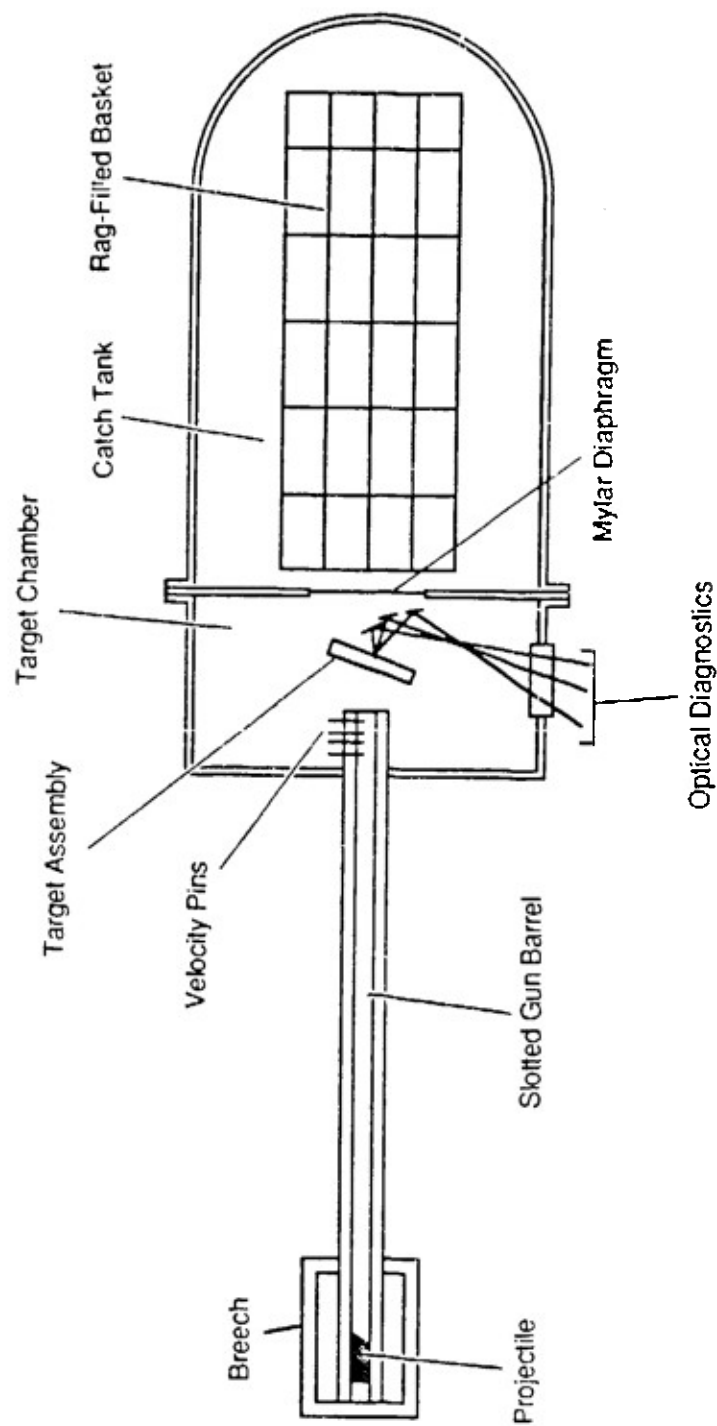
Figure 3. Schematic of SRI's 2.5-inch gas gun facility.

RA-6413-4A

10

Figure 4. HSRP/S projectile and target assemblies.

11

Four pairs of electrical contact pins were located near the edge of the anvil at the 3, 6, 9, and 12 o'clock positions (Figure 4). Single gold contact pins were evaporated onto the anvil; pairs of contact pins were evaporated onto the specimen or flyer impact face, aligned so that they would short across the paired pins and pads on the anvil at impact. The times of electrical contact indicated the "tilt" or deviation from simultaneity (lack of parallelism) of the impact across the face of the target plate. When the anvil was placed in the gun target chamber, it was aligned parallel to the face of the projectile within 0.08 mrad, by using either a newly developed interferometric technique[10] or the optical technique of Kumar and Clifton.[11]

Signals from the projectile velocity contact pins, the tilt pins, and the interferometer photodetector output were recorded on a 4-channel, 500-megasample/s transient digitizer and analog oscilloscopes. The analog data were reduced by magnifying and digitizing the oscilloscope photographs and processing the resulting computer files.

HIGH-STRAIN-RATE PRESSURE/SHEAR TEST

High-strain-rate pressure/shear plate impact testing is a relatively new technique[12-14] that has been applied to metals to obtain stress-strain curves at shear strain rates greater than 10^5 s^{-1} under high and controllable levels of nearly hydrostatic pressure. The method is based on concepts drawn from plate impac testing and Hopkinson bar experiments. From the former is taken the use of plane waves generated by parallel impact, so that a one-dimensional wave theory is applicable and the interpretation of experimental results is simplified. From the latter comes the concept of using elastic "probes" to sandwich and deform a thin specimen and to condu t specimen loads and velocities to a remote location for measurement.

High-strain-rate pressure/shear impact testing is performed by impacting a thin specimen plate against a hard anvil plate inclined at an angle, θ, as shown in Figure 5. This thin specimen plate is backed up by a thick, hard flyer plate, which creates a state of high pressure and high shear strain rate in the specimen. The flyer and anvil plates are designed to remain elastic while the specimen deforms; during the early stages of the test, before release waves reach the center of the plate from the periphery, stress components in the specimen can be inferred from the projectile velocity and particle velocities at the rear surface of the anvil. Thus, measuring a history of particle velocity at the rear surface allows us to construct a shear stress-shear strain curve.
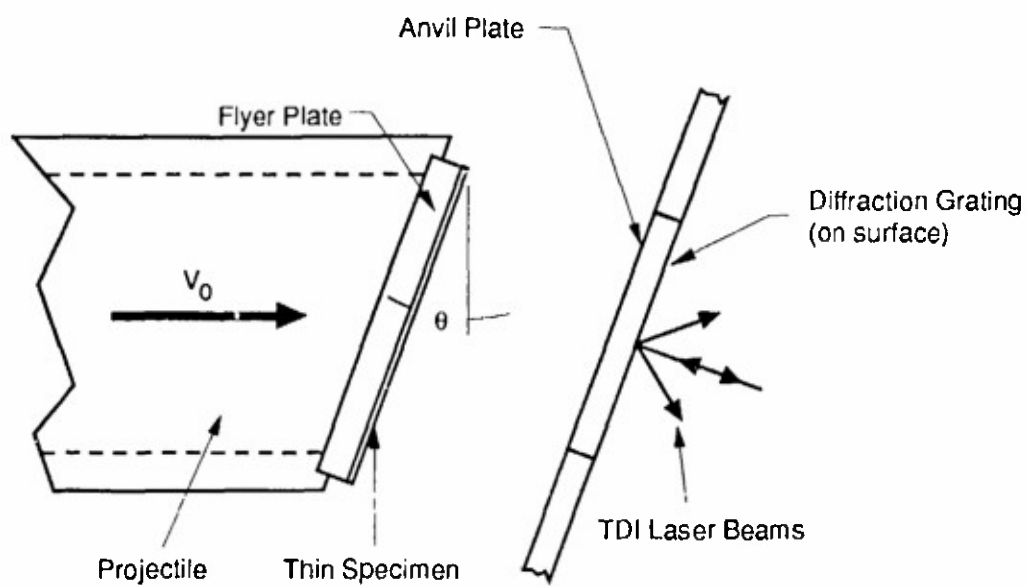
Figure 5. Configuration for HSRP/S experiment.

RM-6413-3A

13

In the early stages of the test, waves reverberate in the specimen (Figure 6). Because these waves are plastic, they are quickly dispersed and the stress state in the specimen becomes nominally homogeneous. The out-of-plane shear and normal stress components are the same as those in the elastic plates. Because the specimen's elastic resistance to volume change will not allow a normal difference in velocity to be maintained across the specimen, the homogeneous normal stress in the specimen quickly "rings up" to the normal stress that would exist if the flyer and anvil impacted in the absence of the specimen. Thus, if the flyer and anvil are made from the same material, the stress component normal to the specimen surface, σ, is given by

$$\sigma = \frac{1}{2} \rho c_1 u_0 \tag{1}$$

where ρ is the density of the elastic plates, c_1 is the elastic longitudinal wave speed, and u_0 is the component of projectile velocity normal to the plates. Computations verify that the hydrostatic pressure in the specimen is nearly equal to the negative of the normal stress.

A finite transverse difference in velocity can be maintained across the specimen for the duration of the experiment. Thus, the shear stress need not ring up to the level that would exist in the absence of the specimen. The shear stress component, τ, at the surface of the specimen is the same as that in the elastic anvil, which is related to the transverse particle velocity, v, in the anvil by

$$\tau = \rho c_2 v \tag{2}$$

where c_2 is the elastic shear wave speed in the flyer and anvil. Because the anvil remains elastic, v is exactly half the velocity at the rear, free surface of the anvil, v_{fs}. Thus,

$$\tau = \frac{1}{2} \rho c_2 v_{fs} \tag{3}$$

The nominal shear strain rate in the specimen, $\dot{\gamma}$, is given by the transverse velocity difference across the specimen divided by its thickness; that is,

14
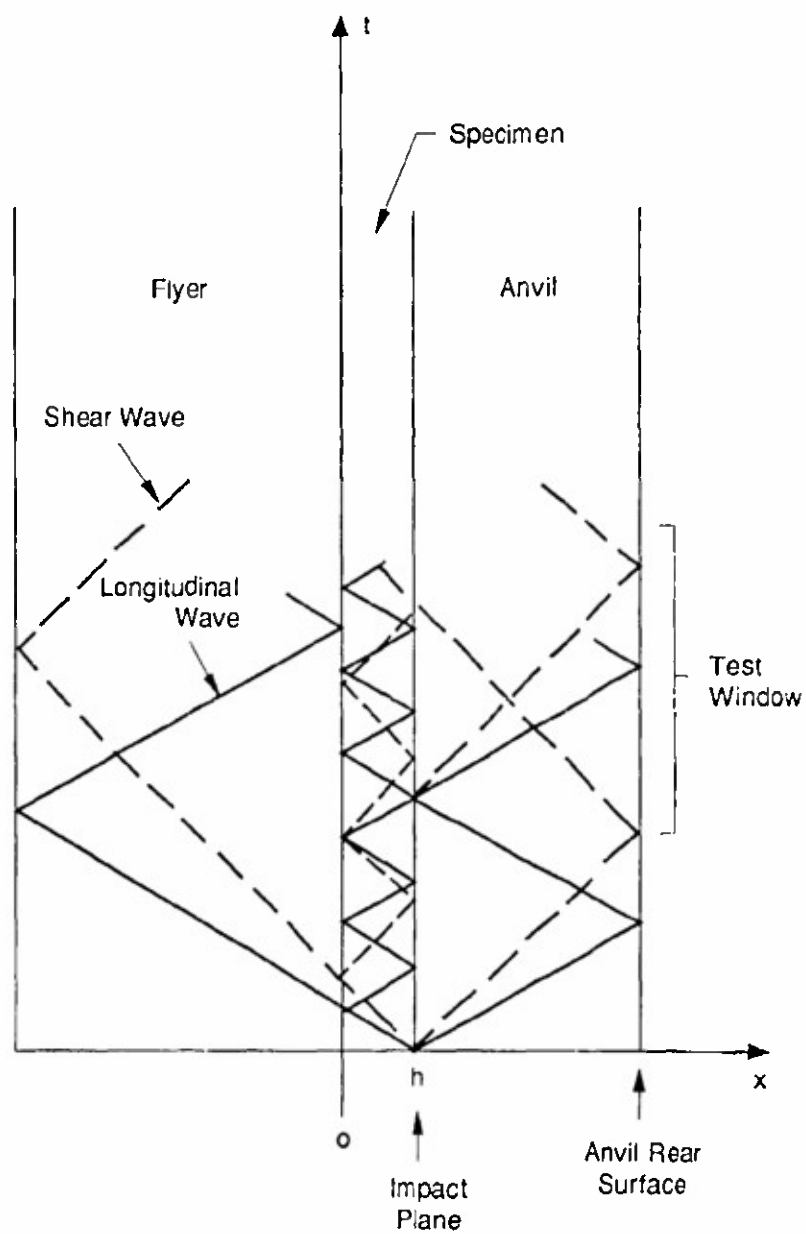
RM-6795-39

Figure 6.   HSRP/S t-x diagram showing waves reverberating in
the specimen.

Elastic wavefronts only are shown in the specimen.

15

$$\dot{\gamma} = \frac{v_F - v_A}{h} \qquad (4)$$

where v_F and v_A are the flyer and anvil particle velocities adjacent to the specimen and h is the thickness. If the flyer and anvil remain elastic, $v_F - v_A = v_0 - v_{fs}$, where v_0 is the component of projectile velocity transverse to the plates. Thus,

$$\dot{\gamma} = \frac{v_0 - v_{fs}}{h} \qquad (5)$$

By integrating Eq. (5) over time, we obtain the nominal shear strain in the specimen, and combining the strains with the stresses from Eq. (3) allows us to construct a stress-strain curve.

In the HSRP/S experiments, the transverse particle velocity at the rear surface of the anvil was monitored by using a transverse displacement interferometer (TDI). This device, developed by Kim et al.,[15] uses the interference of light beams of different Doppler-shifted frequencies to indicate the transverse velocity. The TDI is shown schematically in Figure 7. The interferometer consists of a beam of laser light directed at normal incidence onto a diffraction grating applied to the rear surface of the anvil. The grating is oriented so that the diffracted beams, which are spaced symmetrically about the surface normal, are in the plane of the transverse velocity component to be measured. A pair of diffracted beams with equal angles on each side of the normal are selected and mixed with a system of mirrors and a beam-splitter and projected onto a photodetector. When the rear surface of the anvil plate moves transversely, the two selected diffracted beams are Doppler-shifted, one to a higher frequency and one to a lower. When these beams are mixed, beating occurs at a frequency proportional to the transverse velocity. The transverse displacement, δ, per beat cycle is

$$\delta = \frac{d}{2n} \qquad (6)$$

where d is the pitch of the diffraction grating and n is the diffraction order of the chosen beams. We used first-order ($n = 1$) diffracted beams and a 5-μm-pitch grating in the experiments reported here. The TDI is insensitive to the normal motion of the plate.

16
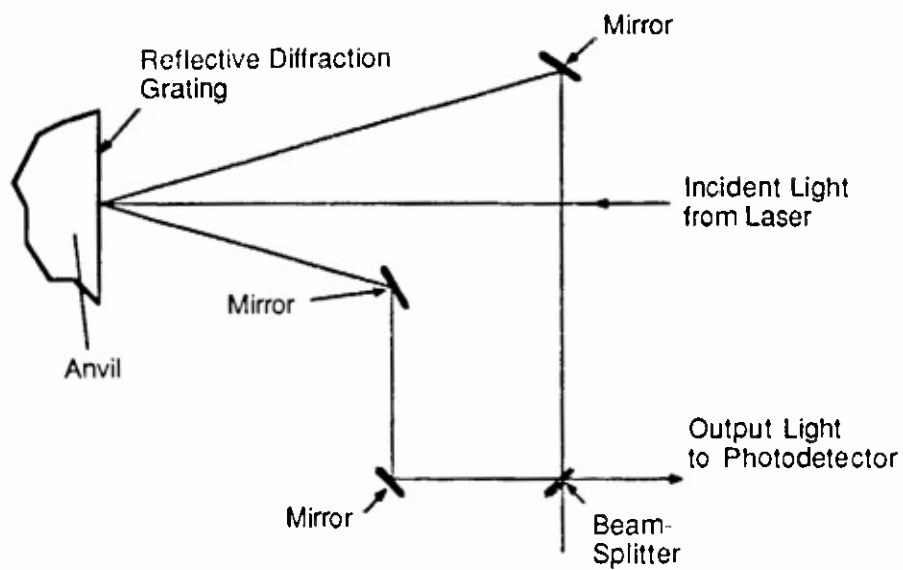
Figure 7.   Transverse displacement interferometer.

17

In the first HSRP/S experiment on AlN, the flyer and the specimen were disks 55 mm in diameter with thicknesses of 5.3 and 0.58 mm, respectively; in the second experiment the specimen thickness was 0.60 mm. The anvils were disks 41 mm in diameter and 4.8 mm thick. The flyers and the anvils were made from hot-pressed B_4C, and the specimens were AlN.

The specimen was glued to the flyer at the periphery, and the flyer-specimen assembly was then glued to the nose of a projectile cut at an angle of 20 degrees. Small relief holes were drilled in the hollow projectile to allow it and the specimen-flyer interface to be evacuated at the same time as the breech, barrel, and target chamber of the gun.

The TDI diffraction grating was applied to the anvil by vapor-depositing a platinum mirror and copying a master 200-lines/mm ($5-\mu m$-pitch) Ronchi ruling onto the polished rear surface with photoresist. The anvil plate was glued into the center of a larger polymethyl methacrylate (PMMA) disk, which was in turn supported by the gun's target holder mechanism.

SYMMETRIC PRESSURE/SHEAR TEST

Experimental Technique

A key requirement in the HSRP/S test is that the flyer and anvil plates that sandwich the specimen not yield. This requirement cannot be met for specimens of the very strongest ceramics, such as SiC, B_4C, and TiB_2, unless diamond or cubic boron nitride flyers and anvils are used. An alternative technique must therefore be considered. A good alternative is the symmetric pressure/shear (SP/S) test,[11] in which an anvil is impacted in a pressure/shear configuration with a flyer of the same material (Figure 8). While not nearly so easy to analyze as the high-strain-rate pressure/shear test, the symmetric pressure/shear test can still provide similar conditions of high confining pressure and strain rate. In this test, the impact velocity and angle and the histories of normal and transverse particle velocity at the target rear surface are measured. These histories are compared with those from a numerical simulation using a postulated material model, which is iteratively modified until the experiment and the simulation agree. If the match is good, the model is at least valid for the test conditions.

At impact in the SP/S test, plastic longitudinal and shear waves propagate forward into the anvil and backward into the flyer (Figure 9), carrying information about the plates' plastic response. The shear wave is especially telling of the deformational behavior, whereas the

18
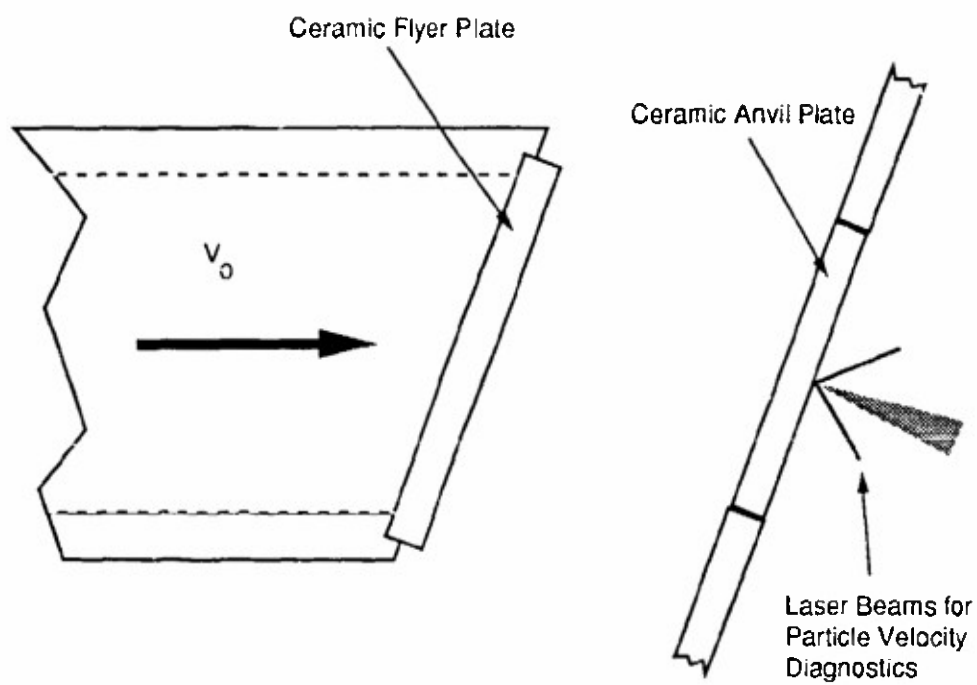
Figure 8.   The symmetric pressure/shear experiment.
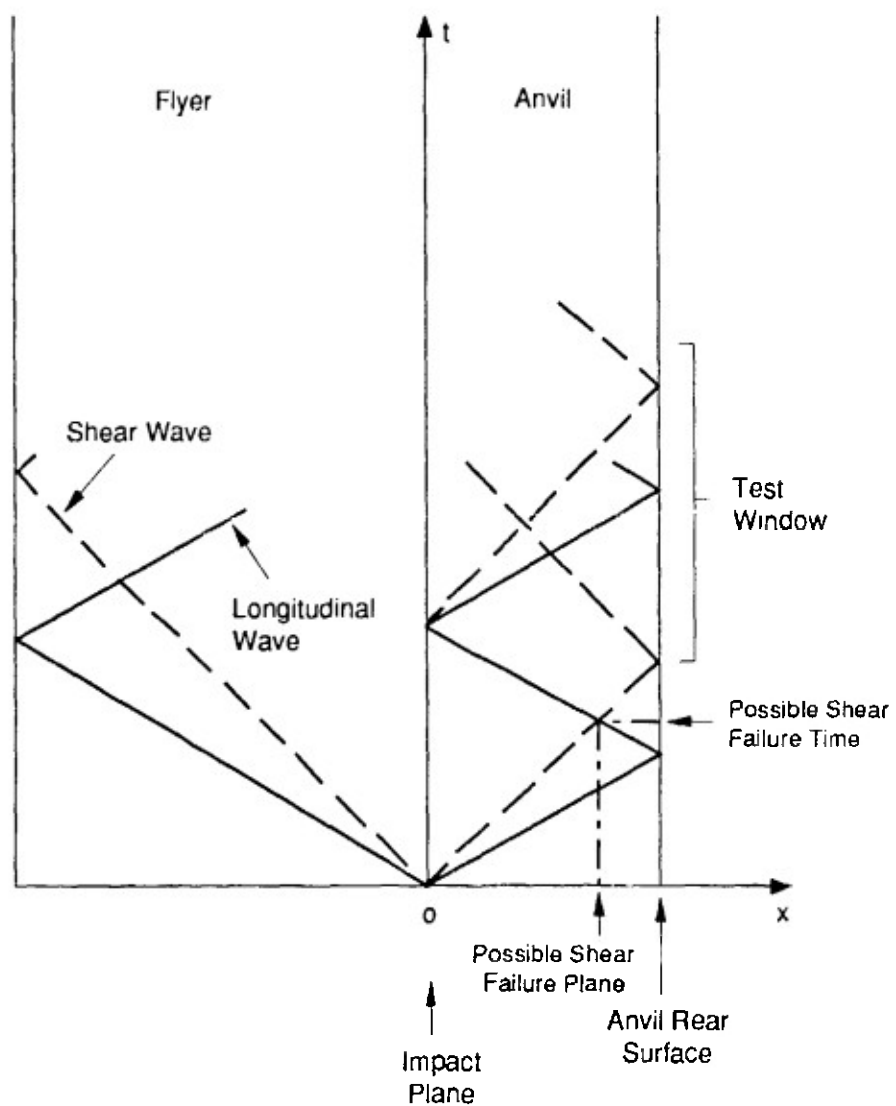
RM-6795-40

Figure 9.   SP/S t-x diagram showing elastic wavefronts only.

20

longitudinal wave is largely dominated by volumetric, nearly elastic behavior. We chose to measure only the transverse velocity history in our experiments.

Although the laser-Doppler velocimeter (LDV) has been in use for nearly 30 years to measure the velocity of fluid-entrained particles and solid surfaces,[16] its use for plate impact experiments was not suggested until the TDI was introduced.[15] To our knowledge, we are the first group to implement it. When the TDI system is used, a diffraction grating must be applied to the anvil rear surface and the grating must survive for the duration of the experiment. At the high-impact velocities necessary for yielding the stronger ceramics, there is doubt about whether a polymer photoresist grating can survive and the expense of etching the grating directly into the ceramic is currently prohibitive. One solution to this problem is to confine the grating behind a window of sapphire, as described by Espinosa and Clifton.[17] Another solution is to dispense with the grating and use an LDV system.

A schematic of our LDV system, TSI Model 9100-3, is shown in Figure 10. A collimated beam of single-wavelength (not necessarily single-frequency) laser light is split by the beam-splitter into two parallel beams that are made to pass through an objective lens, which focuses them to narrow waists and causes them to cross, forming an ellipsoidal measurement volume. When the collimation of the incoming beam is correct, the location of the waists and the center of the intersection region coincide and a group of planar, parallel, equispaced interference fringes is formed within the volume. The fringes are perpendicular to the plane of the intersecting beams and parallel to a plane containing the bisector of the angle between the beams.

There are two ways to illustrate how an LDV works. Both ways lead to the same equation relating light modulation frequency to target transverse velocity. An analogy to the first view is to think of a flashlight moving behind a picket fence. Consider a light-scattering object moving through the measurement volume. Light will scatter strongly from the object when it is in a bright fringe plane and weakly (not at all, ideally) when it is in a dark fringe plane. The modulation frequency of the scattered light will be the object speed divided by the fringe spacing, which is given by

$$d_f = \frac{\lambda}{2 \sin \kappa} \tag{7}$$

From Laser

Splitter

Lens

Moving Target

Scattered Light

Photo-Tube

Target Surface

Planar Fringes
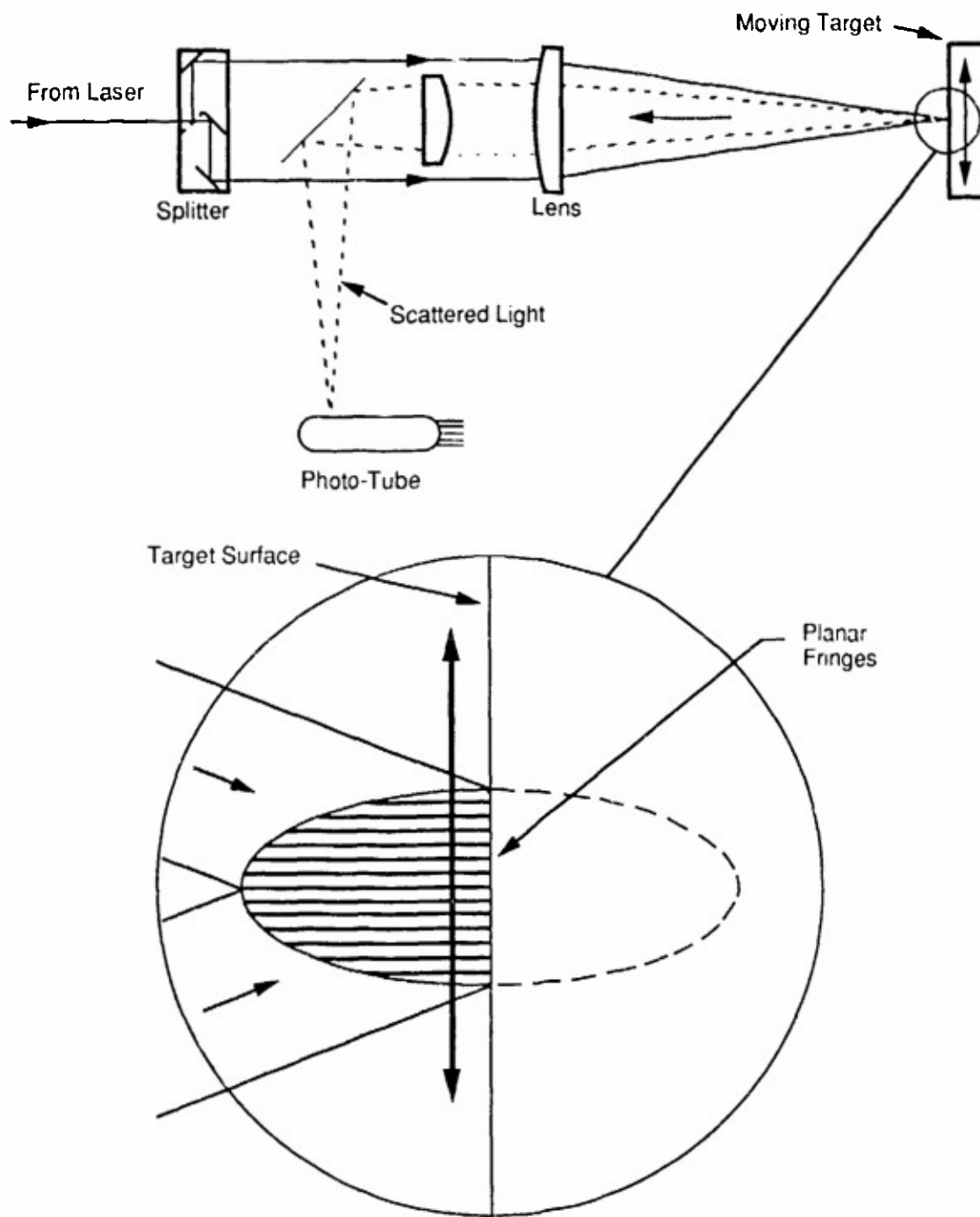
RAM-8521-79A

Figure 10. The laser Doppler velocimeter (LDV) system.

22

where λ is the wavelength of the laser light and 2κ is the beam crossing angle. Thus,

$$\tan \kappa = \frac{d}{2F} \tag{8}$$

where d is the beam spacing entering the objective and F is the objective focal length. Thus, the frequency, f, for a given velocity is

$$f = \frac{2v \sin \kappa}{\lambda} \tag{9}$$

The other, equivalent way to understand how an LDV works is to consider the interference of light scattered from each intersecting beam. The light scattered from one beam will be Doppler-shifted fast, the other will be slow, and the mixed light will interfere with a beat frequency given by Eq. (9).

Like the TDI, the LDV is insensitive to the normal motion of the anvil. Unlike the TDI, however, the LDV is also insensitive to target tilt or to the condition of the anvil rear surface as long as scattered light reaches the detector. Thus, the LDV can be applied in situations where the TDI cannot.

Analysis Techniques

The extraction of stresses, strains, and other mechanical variables from the transverse velocity history recorded in an SP/S test requires that the test be modeled with a postulated material model and that the model parameters be adjusted until the computed and measured velocity histories match. Then, the desired mechanical variables can be extracted from the simulation. We have used two models, one a continuum model that uses an elastic-viscoplastic, Mohr-Coulomb, dilatant flow law and the other a model that views the flow of ceramic as the movement of blocks within a fragment bed. Both models are fully described elsewhere[4,18] and will be only briefly outlined here; the description by Klopp and Shockey[18] is included in the Appendix.

The Mohr-Coulomb model's formulation follows that of Abou-Sayed and Clifton for aluminum,[19] which is in turn based on the viscoplastic formulation of Perzyna.[20] We have added comminution, dilatancy, and mean-stress-dependent yielding following the formulation used by Rudnicki and Rice.[21] The resulting constitutive equation has the form

23

$$\dot{\varepsilon}_{ij} = \frac{1+\nu}{E}\dot{\sigma}_{ij} - \frac{\nu}{E}\delta_{ij}\dot{\sigma}_{kk} + \left\langle \phi(\bar{\tau}, \bar{\gamma}^p, p, D)\right\rangle \frac{\partial f}{\partial \sigma_{ij}} \tag{10}$$

where $\dot{\varepsilon}_{ij}$ is the total strain rate, ν is Poisson's ratio, E is Young's modulus, δ_{ij} is the Kronecker delta, ϕ is the equivalent plastic strain rate, $\bar{\tau}$ is the effective shear stress, $\bar{\gamma}^p$ is the equivalent plastic shear strain, $p = -\sigma_{kk}/3$ is the negative of the mean stress or hydrostatic pressure, D is the amount of comminution, and f is a flow potential. The bracket function $\langle\phi\rangle$ returns the value of the function ϕ when it is positive, and zero otherwise. The effective stress is given in the usual way in terms of the deviatoric stress, $S_{ij} = \sigma_{ij} - \delta_{ij}\sigma_{kk}/3$: $\bar{\tau} = (\frac{1}{2}S_{ij}S_{ij})^{1/2}$. The overstress, $\bar{\tau} - \tau_y$, is proportional to the logarithm of the plastic strain rate. Thus,

$$\phi = \frac{\dot{\gamma}_0}{\sqrt{3}}\exp\left[\left(\frac{\bar{\tau}-\tau_y}{\tau_0}\right)^{1/m}\right] \tag{11}$$

The yield stress τ_y depends on the mean stress, amount of comminution, and strain hardening. When comminution is extensive, $D \approx 1$ and Mohr-Coulomb behavior described by $\tau_y = p\mu$ dominates, μ being the friction angle tangent. The amount of comminution evolves from 0 toward 1 at a rate given by the amount the second invariant of the total stress exceeds some constant limit.

$$\dot{D} = \frac{(I_2 - I_{LIM})}{\rho c_1^2 t_0}(1-D) \tag{12}$$

Here ρ is the density, c_1 is the longitudinal wave speed, and t_0 is a time constant. The choice of I_2 as the driving force for comminution is based on the notion that even purely hydrostatic loadings comminute polycrystalline ceramic. Hydrostatic loading causes comminution because neighboring grains often have different crystallographic orientations and, thus, different strain fields as a result of anisotropy. Cracks form when the stresses necessary to enforce the compatibility of these strain fields across grain boundaries exceed some failure stress. Recent work by Lankford[3] supplies strong microscopic evidence of grain boundary cracking caused by incompatible plastic strains within neighboring grains.

The constitutive Eq. (11), together with the momentum and compatibility equations, are rewritten as equations along characteristics. We solved these equations by using a modification of the method of Ranganath and Clifton.[22] The boundary conditions for the anvil plates are that

24

the rear surface is traction-free and the impact face has an imposed velocity of half the impact velocity.

The fragment bed (FRAGBED) model[4] is based on an analogy between fragment block sliding and dislocation theory. The basic relation is

$$d\gamma_i^p/dt = (\tau_i - \mu\sigma_{ni})/(\rho_s c_2^2 T) \tag{13}$$

where γ_i^p is the plastic strain on the ith slip plane; τ_i is the shear stress; μ is the tangent of the friction angle; σ_{ni} is the normal stress on the slip plane; ρ_s is the solid density; c_2 is the speed of shear waves; and $T = B/(2gf_ic_2)$, a time constant. B is the block dimension, g is a factor on the order of 1 relating the active slip system to the shear strain direction, and f_i is the fraction of blocks that have an adjacent vacancy large enough to allow slip.

The block sliding description is incorporated into a multiple-plane plasticity model[23] originally developed for brittle fracture and shear band problems. In addition to the block sliding description, the model includes a treatment of the creation and destruction of porosity via the competing processes of dilatancy and compaction. A Mie-Grüneisen relation is used for the pressure. Yield and tensile strengths are reduced by the developing fragmentation. The complete model was incorporated into a one-dimensional hydrocode, called COPS2, designed to model pressure/shear tests.

RESULTS

Pressure/Shear Tests

Selected physical properties and the source of the tested ceramics are shown in Table 1. The density and wavespeed values were provided by the suppliers.

The impact parameters for the three experiments on AlN are shown in Table 2. Two HSRP/S and one SP/S experiment were performed. The histories of transverse particle velocity, shear stress, and strain rate from the two HSRP/S experiments are shown in Figure 11, and the resulting shear stress-strain curves are shown in Figure 12. The polymer grating on the anvil in test AN-2 deteriorated so rapidly that only the first 4 (of perhaps 50) TDI interference fringes were captured. Thus, only the initial response is known. The extrapolation from the initial response, assuming no strain hardening, is shown by a dotted line. The history of transverse particle velocity from the subsequent SP/S experiment is shown in Figure 13.

25

Table 1

MATERIAL PROPERTIES OF TESTED CERAMICS

Material	ρ (g/cm^3)	C_1 (mm/μs)	C_2 (mm/μs)	Manufacturer	Manufacturer's Designation
AlN	3.26	10.8	6.2	Dow Chemical	Roklite 500 (carbothermally reduced, hot-pressed)
85% Al_2O_3	3.42	8.8	5.1	Coors	AD-85
99.5% Al_2O_3	3.81	10.3	6.2	Coors	AD-995
B_4C	2.51	13.5	8.5	Dow Chemical	Roklite 100 (hot-pressed)
SiC	3.10	11.2	7.3	Carborundum	Sintered α - SiC

Table 2

IMPACT PARAMETERS FOR AlN EXPERIMENTS

Experiment	Configuration[a]	V_o (mm/μs)	Specimen Thickness	Angle (degree)	Nominal Pressure (GPa)
AN-1	HSRP/s	0.672	0.577 mm	20	10.9
AN-2	HSRP/S	0.680	0.599 mm	20	11.1
AN-3	SP/S	0.696	N/A[c]	15	6.6[b]

[a] HSRP/S = high-strain-rate pressure/shear (Figure 5)
   SP/S = symmetric pressure/shear (Figure 8)
[b] Pressure varies significantly in SP/S.
[c] There is no specimen in an SP/S test, only flyer and anvil.

26
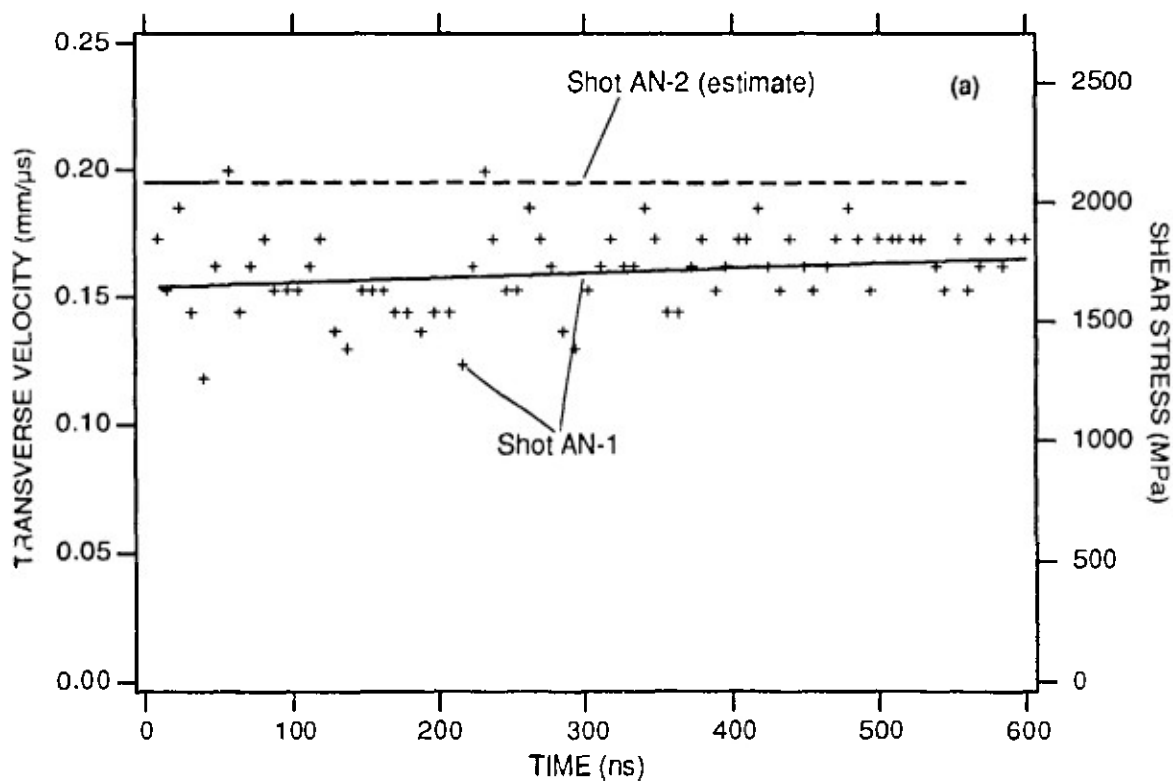
(a) Transverse velocity and shear stress histories
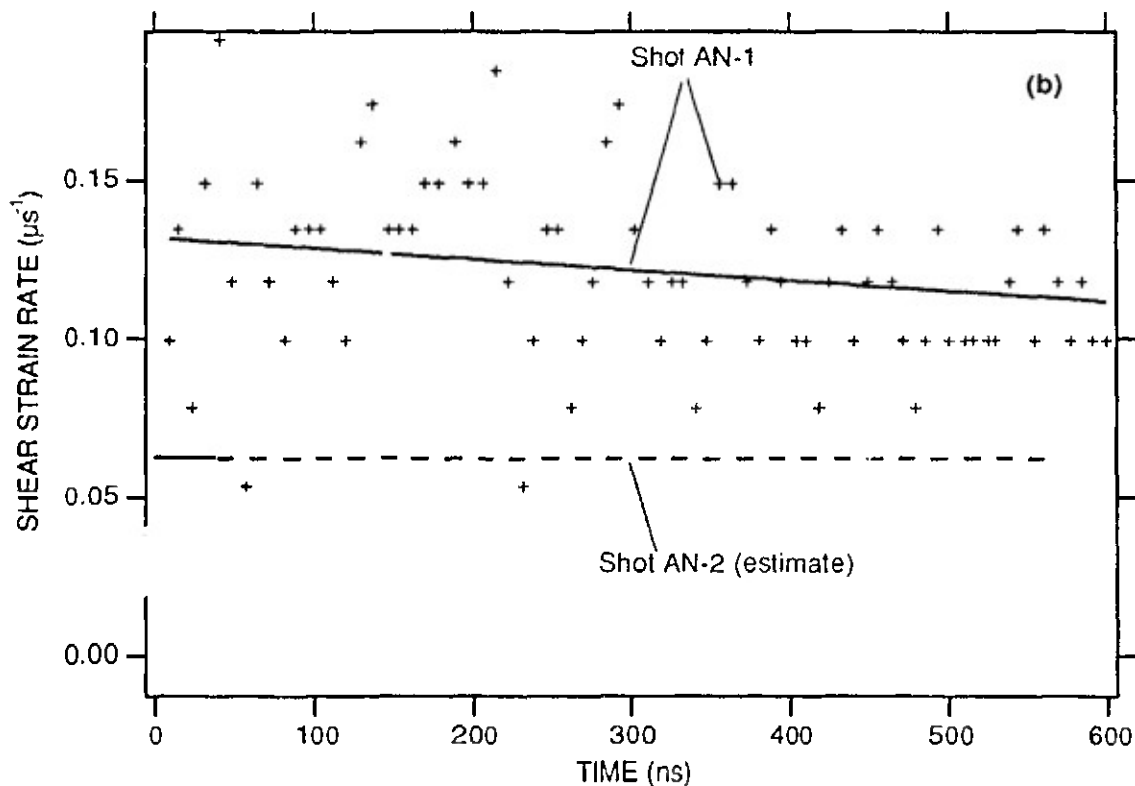
(b) Strain rate history

RAM-6795-41

Figure 11.   Results from HSRP/S tests on AlN.

27
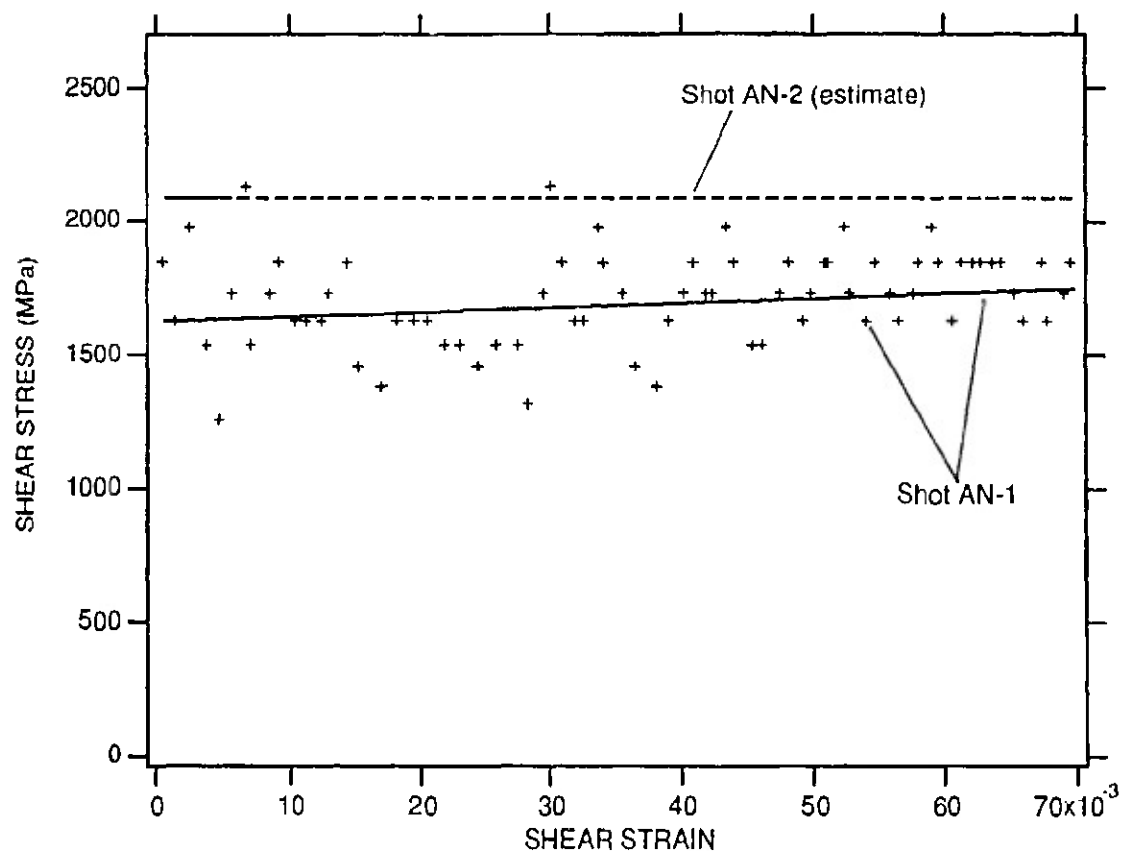
Figure 12. Stress-strain curves from HSRP/S tests on AIN.
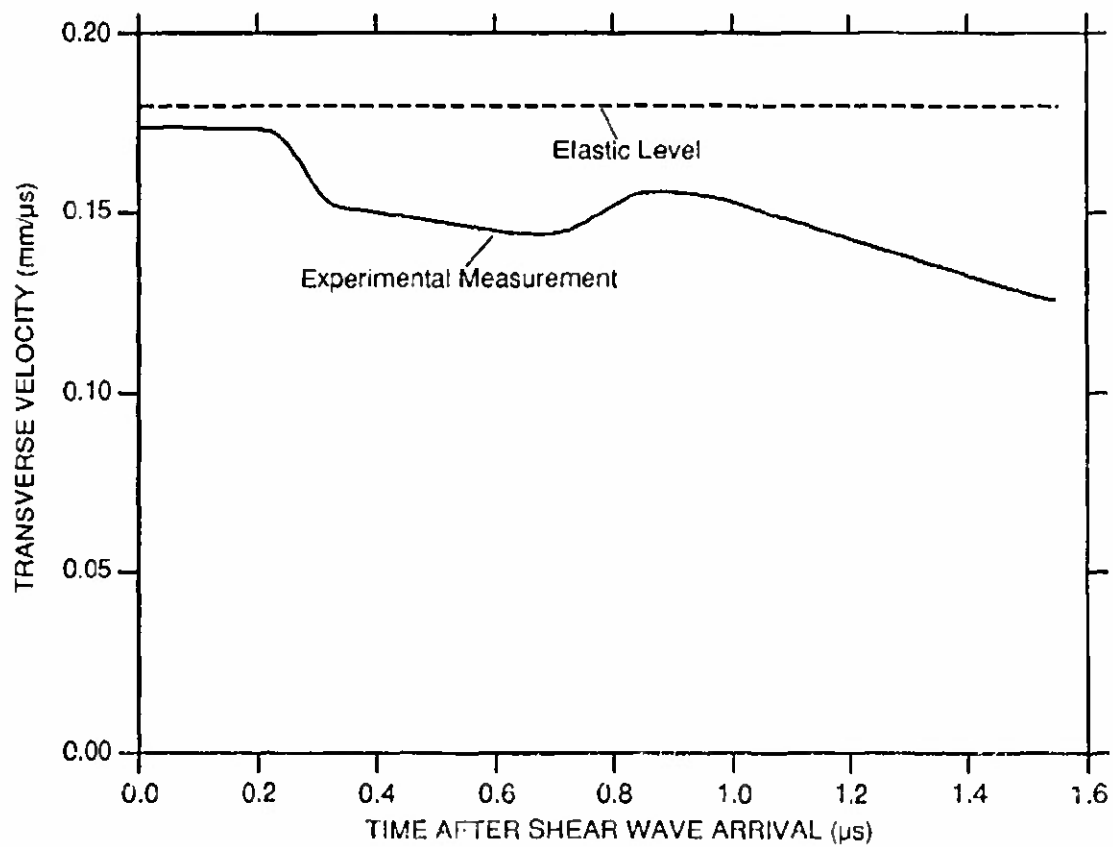
Figure 13.   Transverse velocity history from SP/S experiment on AlN.

The impact parameters for the three SP/S experiments on Al_2O_3 are shown in Table 3. One Coors AD-85 and two Coors AD-995 (Coors Porcelain Co., Golden, Colorado) specimens were tested. The resulting transverse velocity histories are shown in Figure 14. In Shots AO-1 and AO-2, the impact faces were polished to a $\approx$6-nm RMS finish as measured by a profilometer. In Shot AO-3, the impact faces were roughened by sandblasting to help preclude slip. The RMS roughness of the sandblasted surface was not measured, but a scanning-laser microscope profile of the surface shows that sandblasting created pits $\approx$5 μm in diameter, $\approx$1 μm deep, spaced $\approx$15 μm apart on the previously nearly pit-free surface.

The impact parameters for the SP/S experiment on B_4C are shown in Table 4, along with the impact parameters from the two HSRP/S experiments on AlN in which the flyer and anvil plates sandwiching the specimen were B_4C. The reason for including these results will become apparent in the Discussion; the B_4C in the HSRP/S tests may have failed. The resulting transverse velocity history from the SP/S experiment is shown in Figure 15.

Analyses

The stress-strain-pressure behavior measured in the two HSRP/S experiments on AlN were used to predict the results of the SP/S experiment on AlN. Shot AN-1 was simulated by using the Mohr-Coulomb model, and parameters were adjusted to match the measured response, as shown in Figure 16. The final parameters for AlN and the other ceramics tested are shown in Table 5. The result of modeling the AlN SP/S test by using the AlN HSRP/S parameters is shown in Figure 17. The prediction of the FRAGBED model is also shown. Clearly, both models significantly underpredict the measured transverse velocity. The reasons for this underprediction will be presented in the Discussion.

The Mohr-Coulomb model parameters used to model Shot AO-1 on AD-85 Al_2O_3 are also shown in Table 5, and the calculated transverse velocity is shown as the lower dashed curve in Figure 18. Those same parameters, when used to model Shots AO-2 and AO-3 on AD-995, give the upper dashed curve in Figure 18.

Table 5 also gives the Mohr-Coulomb model parameters for B_4C that result in a decaying velocity history, Figure 19. The velocity history is qualitatively similar to that measured in Shot BC-1, Figure 15, but the amplitude and decay rate are not the same. We expect that further iteration would produce parameters providing a better match to the experimental history.

30

Table 3

IMPACT PARAMETERS FOR SP/S EXPERIMENTS ON Al_2O_3

Experiment[a]	Material	V_o (mm/μs)	Impact Face
AO-1	AD-85	0.421	Polished
AO-2	AD-995	0.595	Polished
AO-3	AD-995	0.596	Roughened

[a] All at θ = 15 degrees, all symmetric pressure/shear.

Table 4

IMPACT PARAMETERS FOR SP/S EXPERIMENT ON B_4C

Experiment[a]	V_o (mm/μs)	Configuration[b]
BC-1	0.939	SP/S
BC-2	0.672	BSP/S
BC-3	0.680	BSP/S

[a] All θ = 15 degrees.

[b] SP/S = symmetric pressure/shear
BSP/S = symmetric pressure/shear with AlN buffer.
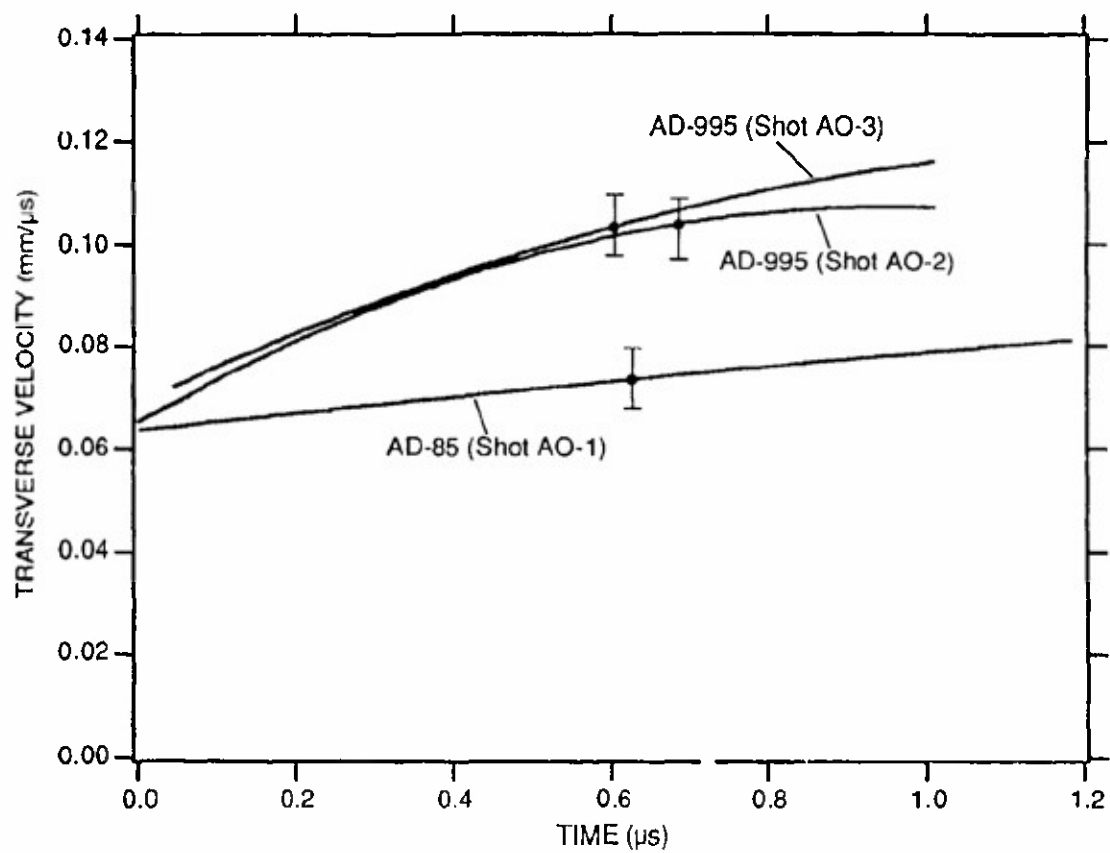
Figure 14. Transverse velocity-time histories from SP/S experiments on AD-85 and AD-995 Al_2O_3.

RAM 6795-44

32
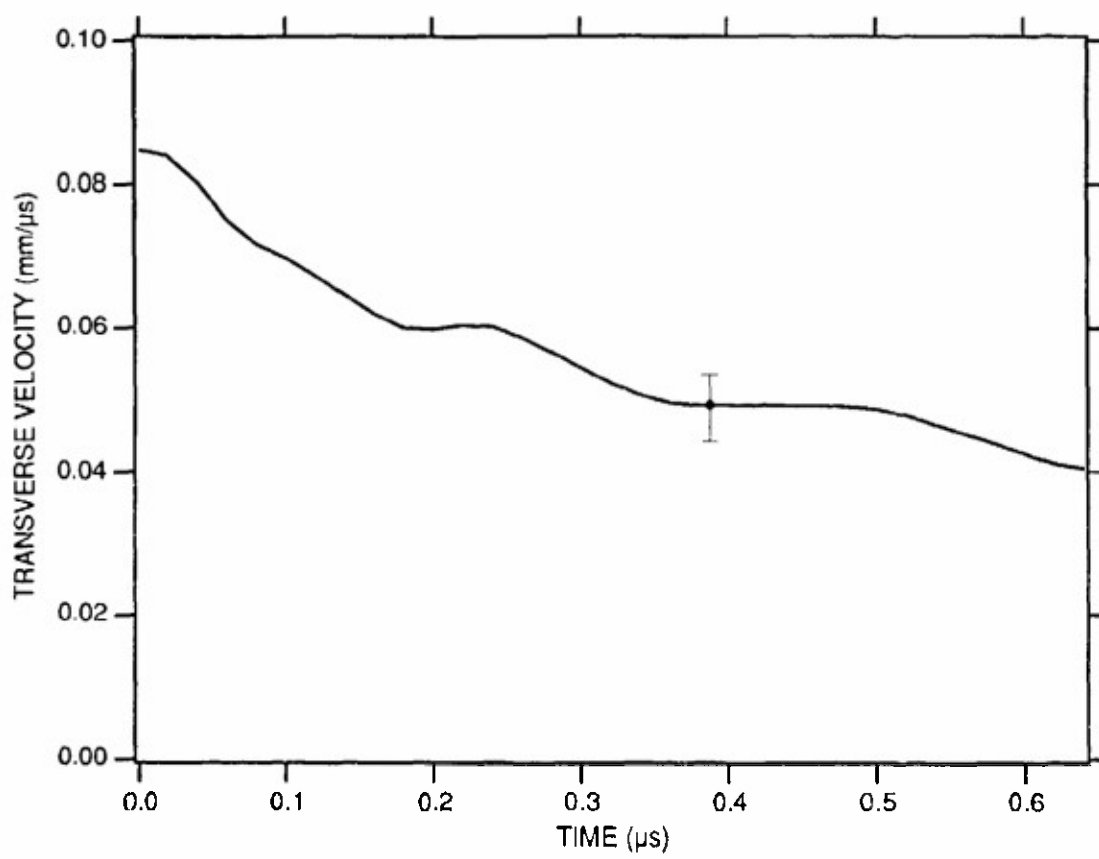
Figure 15. Transverse velocity history from SP/S experiment on B$_4$C.

33
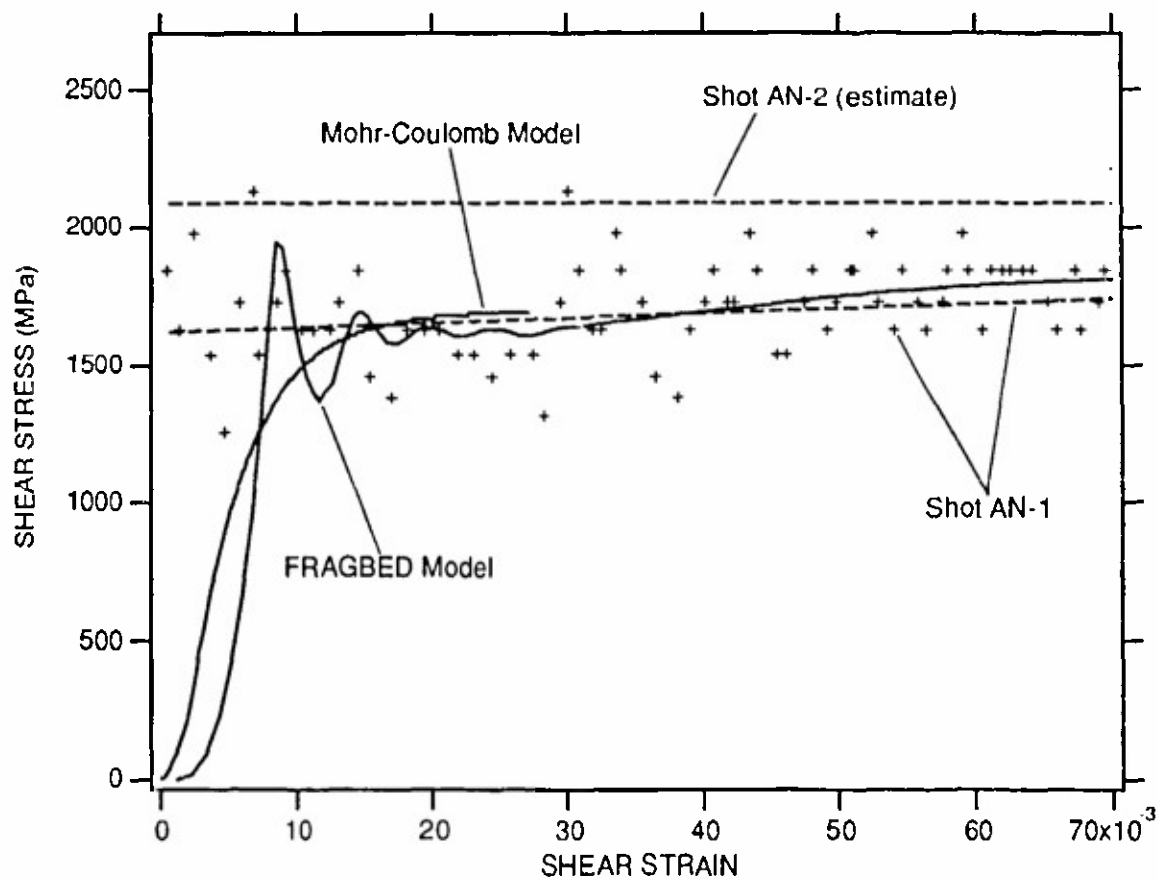
Figure 16.   Mohr-Coulomb and FRAGBED simulations of AIN HSRP/S results.

RAM-6795-46

34

Table 5

SIMULATION PARAMETERS FOR VARIOUS CERAMICS

		AlN	AD-85 & AD-995 Al_2O_3	B_4C
Density (kg/m^3)	ρ	3.26	3.42	2.51
Longitudinal wave speed ($mm/\mu s$)	c_1	10.8	8.8	13.7
Shear wave speed ($mm/\mu s$)	c_2	6.2	5.1	8.5
Initial yield stress (GPa)	τ_{yo}	1.6	3.52	10.0
Friction coefficient	μ	0.057	0.23	0.45
Shear modulus (GPa)	G	126.0	88.0	181.5
Poisson's ratio	ν	0.25	0.25	0.19
Mean stress at HEL (GPa)	P_{HEL}	5.0	3.39	6.8
Shear stress at HEL (GPa)	τ_{HEL}	3.0	2.03	6.4
Square root of second stress invariant at damage limit (GPa)	I_{LIM}	7.0	4.8	3.1
Strain rate constant (s^{-1})	$\dot{\gamma}_o$	0.11	3.0	1.0
Shear stress constant (MPa)	τ_o	1.2	1.5	0.5
Strain rate power	m	2.0	2.0	2.0
Pressure constant (GPa)	P_o	1.0	1.0	1.0
Time constant (ns)	t_o	0.1	1.0	0.1
Hardening modulus (GPa)	h	1.14	10.0	10.0
Dilatancy ratio	β	0.2	0.2	0.2

35
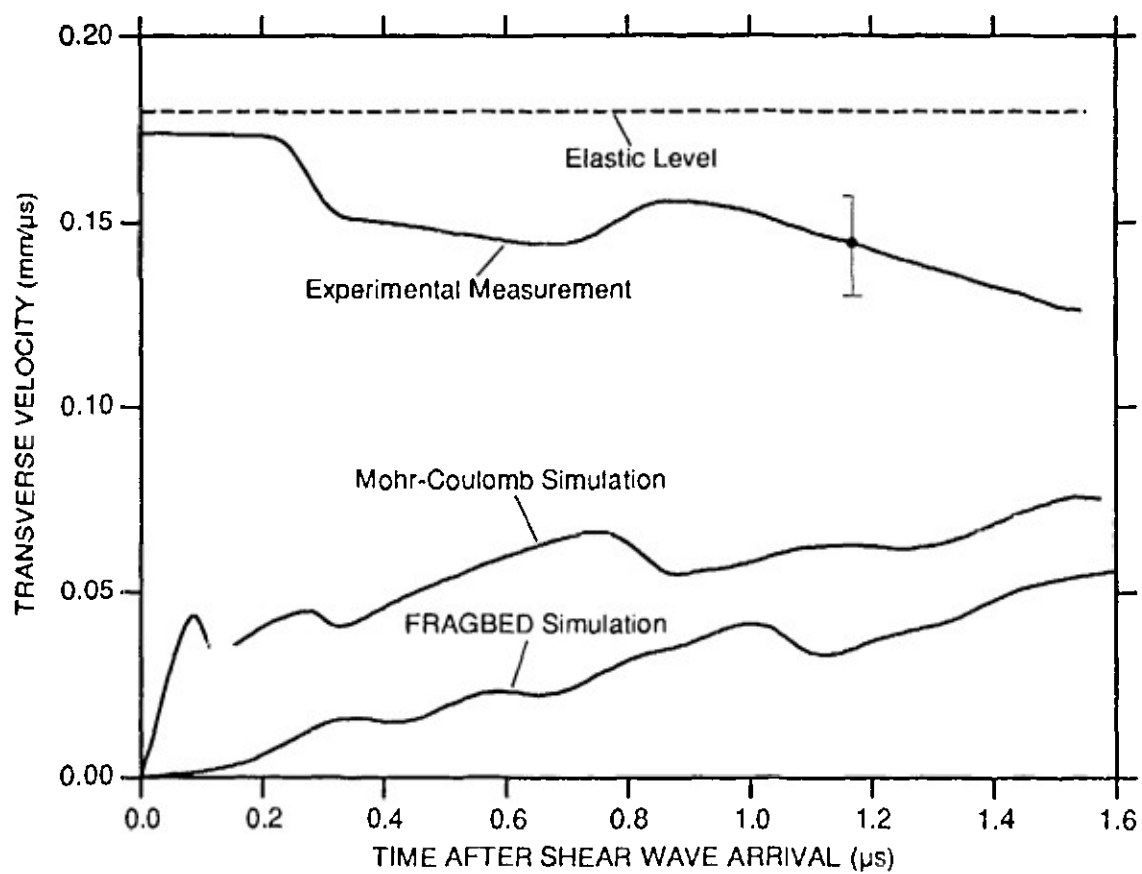
RAM-6795-47

Figure 17. Result of simulating an SP/S experiment on AIN using parameters inferred from HSRP/S experiments.

36
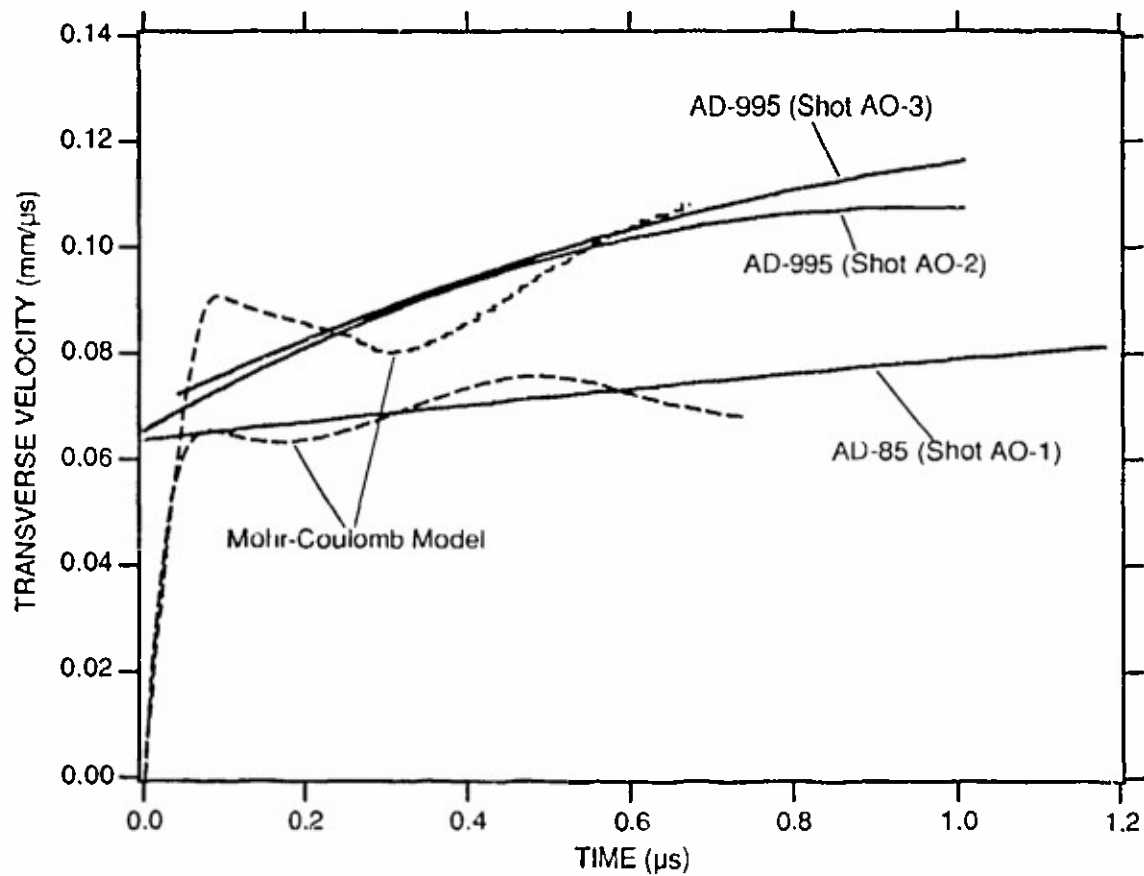
RAM-6795-48

Figure 18. Results of simulating SP/S experiments on Al_2O_3 using the Mohr-Coulomb model.

AD-85 strength parameters were used to simulate the AD-995 experiments.

37
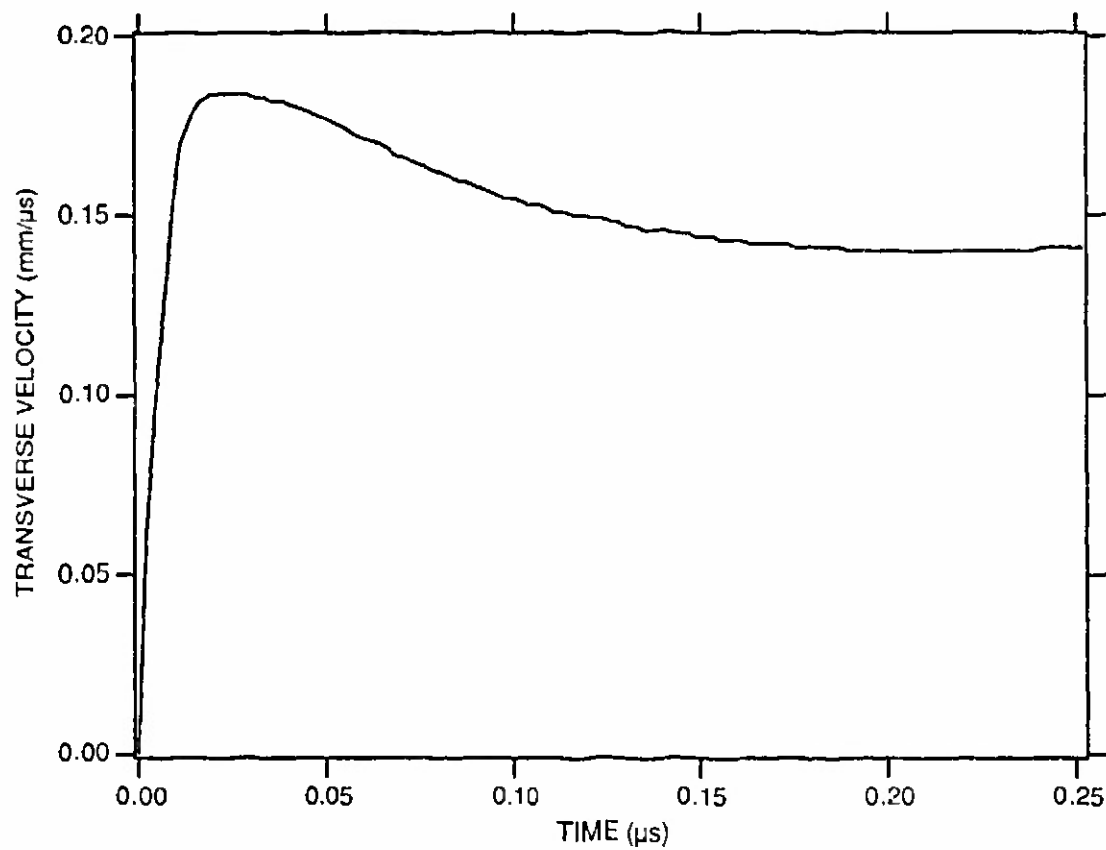
RAM-S795-49

Figure 19. Mohr-Coulomb simulation of B_4C SP/S experiment.

38

DISCUSSION

Table 6 summarizes the Mohr-Coulomb properties of the ceramics in terms of the friction coefficient and the shear strength at the applied mean stress, i.e., a slope and intercept inferred from the simulations. To facilitate comparison, Table 6 also presents the properties in terms of the shear strength at a mean stress of 5 GPa. The fact that the strengths regularized to 5 GPa mean stress are all (but one) nearly the same is remarkable but possibly misleading; the strengths were not measured at 5 GPa and would possibly be different had they been measured at 5 GPA mean stress. Likewise, the fact that all but one of the friction coefficients (slopes) in Table 6 are equal to 0.23 is misleading: except for the AlN HSRP/S simulation, we did not explore other values. There is nothing to suggest that the value 0.23 is unique. Failure surfaces with high slope and low intercept might serve just as well as failure surfaces with low slope and high intercept.

The pressure/shear experiments have revealed a wide range of mechanical response among the ceramics tested. The transverse velocity for AlN nearly reached the elastic level, whereas the velocity for B_4C was only 35% of the elastic level. For AlN and B_4C, velocities decayed with time; for AD-85 and AD-995 Al_2O_3, velocities increased with time. The former behavior is characteristic of faster decay waves overtaking the initial shear wave from behind, whereas the latter behavior is characteristic of slower following waves. The different ceramics seem to have different mechanisms for failure and postfailure flow, and these mechanisms operate at different threshold loads.

Figures 20 and 21 summarize the HSRP/S and SP/S results obtained for AlN and AD-85 and AD-995 Al_2O_3. The data are presented in terms of equivalent shear strength as a function of pressure, deduced from the Mohr-Coulomb model parameters, assuming 10^5 s^{-1} shear strain rate, 0.05 equivalent plastic strain, full damage, and a mean stress around the average attained in simulating a particular test. Figure 20 includes results for AlN obtained by Heard and Cline[24] using quasistatic compression, by Lankford[25] using a split-Hopkinson pressure bar, and by Grady[26] and Rosenberg et al.[27] using normal plate impact. Figure 21 includes the results for AD-85 obtained by Yeshurun et al.,[28] Wilkins,[29] and Gust and Royce[30] and the results for AD-995 obtained by Gust and Royce.[30] Figure 22 includes the results for B_4C obtained by Grady,[26] Wilkins,[29] and Rosenberg and Yeshurun.[31] Figure 23, from Klopp and Shockey,[18] shows similar results obtained by Johnson et al.,[32] by Grady,[26] Kipp and Grady,[8] and Klopp and Shockey[18] on silicon carbide (SiC).

39

Table 6

SUMMARY OF RESULTS—INFERRED MOHR-COULOMB
PARAMETERS FOR VARIOUS CERAMICS

	Friction Coefficient	Shear Strength (GPa)	Mean Stress (GPa)	Shear Strength at 5 GPa Mean Stress
AIN (HSRP/S)	0.057	1.8	11.0	1.4
AIN (SP/S)	0.23	4.9	6.6	4.5
AD-85	0.23	1.1	3.5	1.4
AD-995	0.23	1.8	6.5	1.5
SiC	0.23	1.3	4.0	1.5
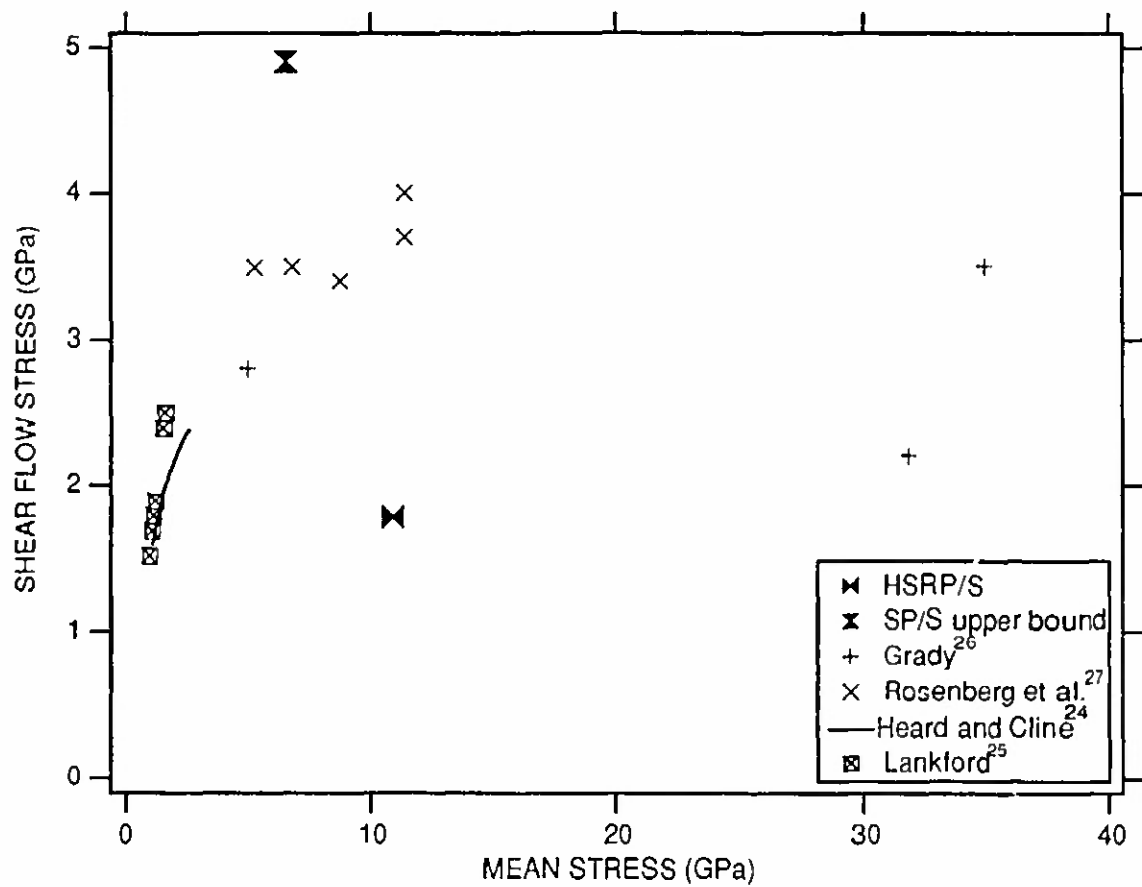
Figure 20.   Equivalent shear flow stress as a function of mean stress for AlN.

41
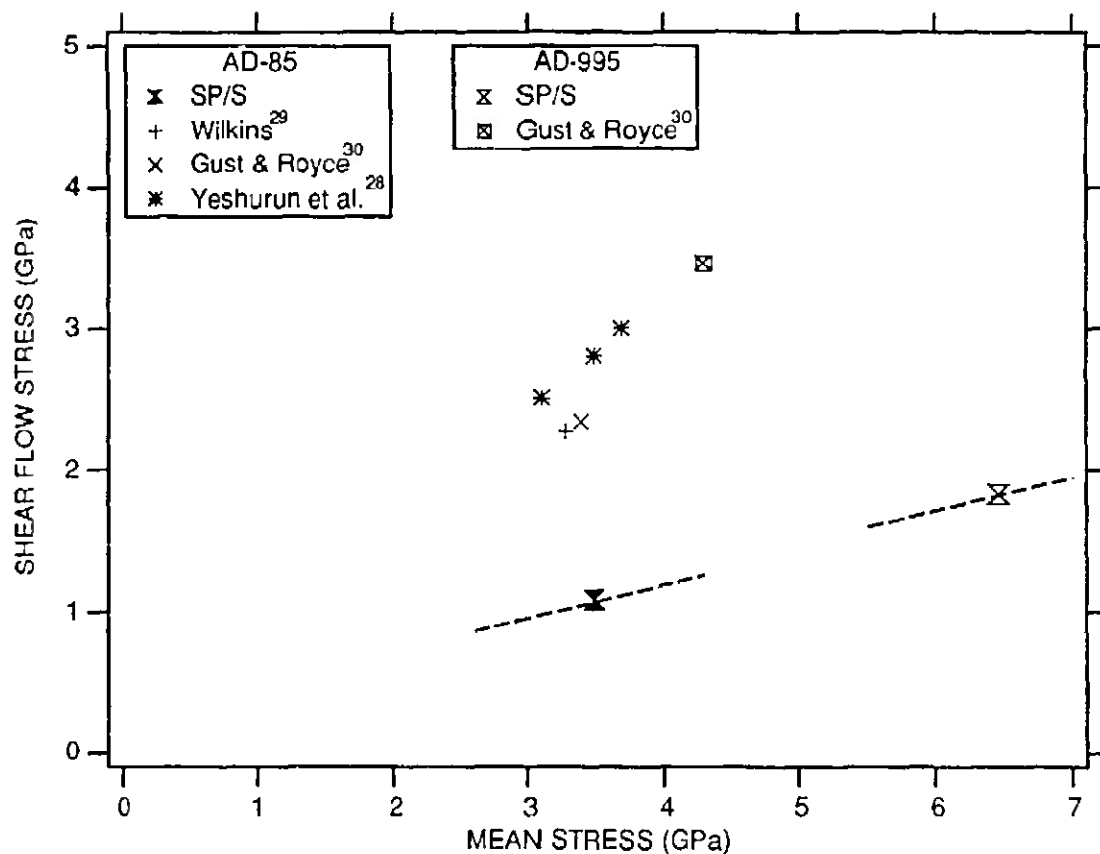
Figure 21.   Equivalent shear flow stress as a function of mean stress for AD-85 and
AD-995 Al_2O_3.

RAM-6795-52

42
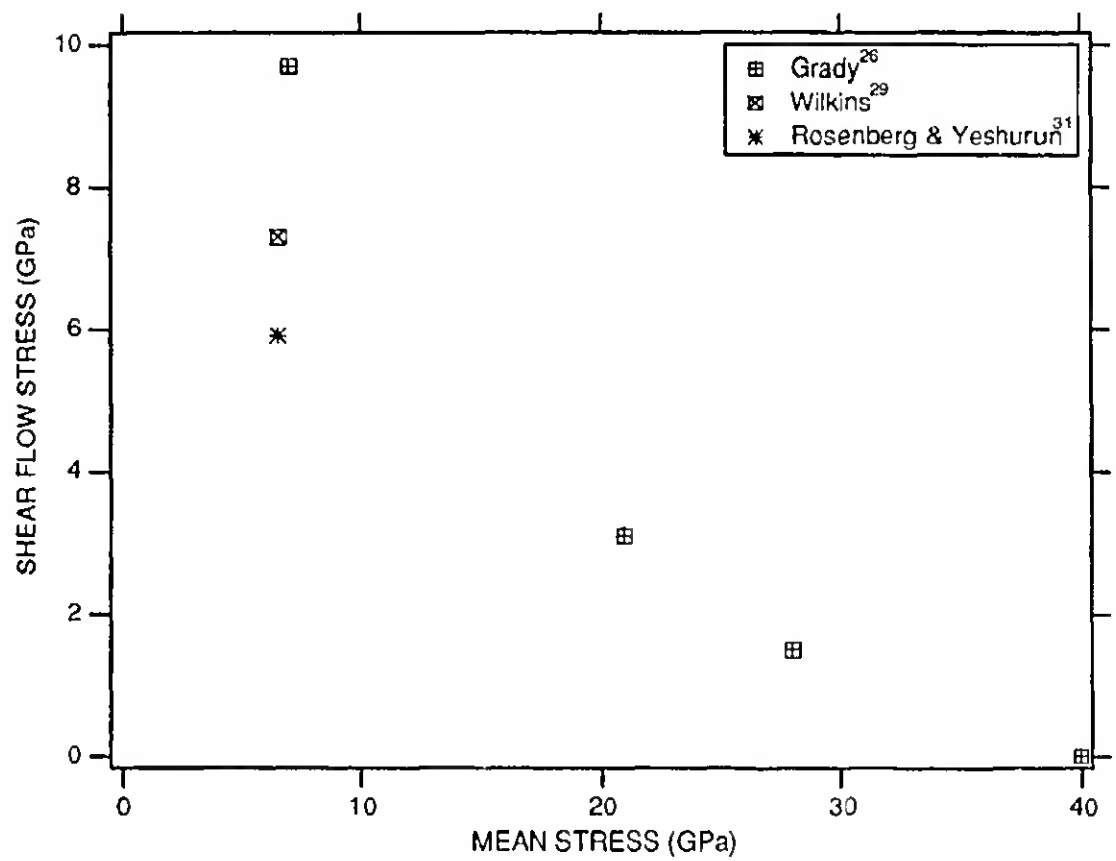
Figure 22. Equivalent shear flow stress as a function of mean stress for B₄C.
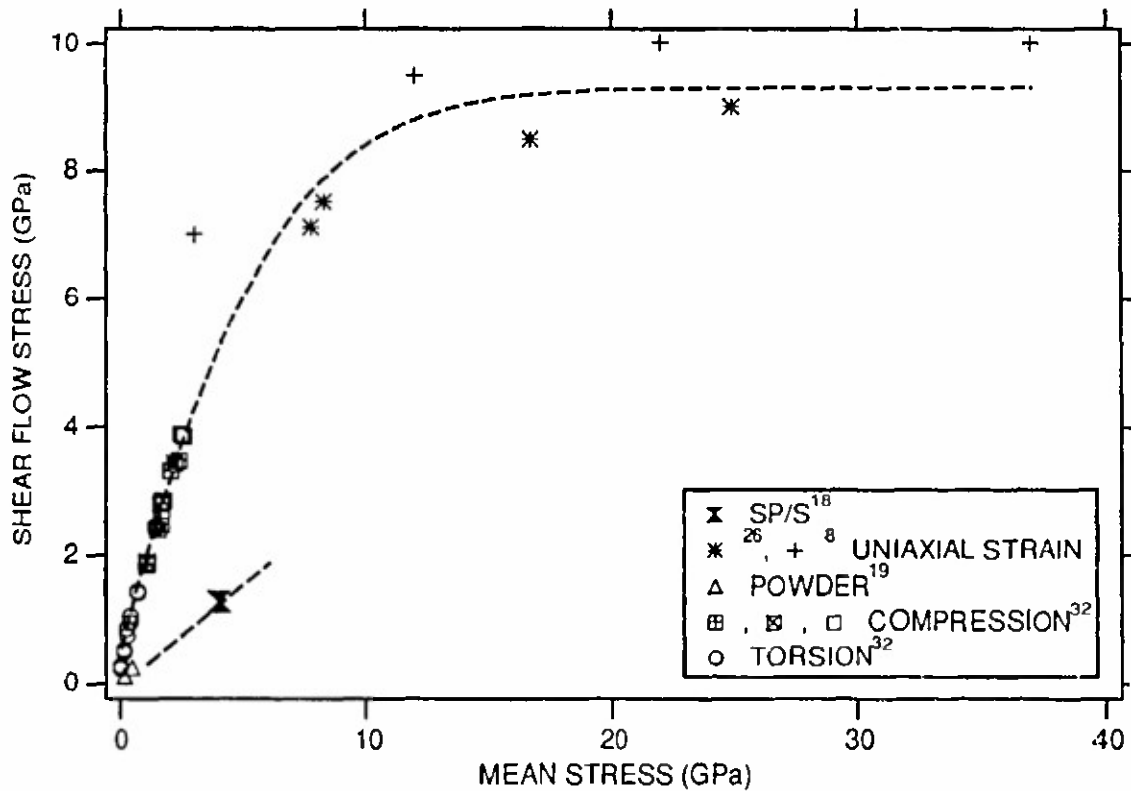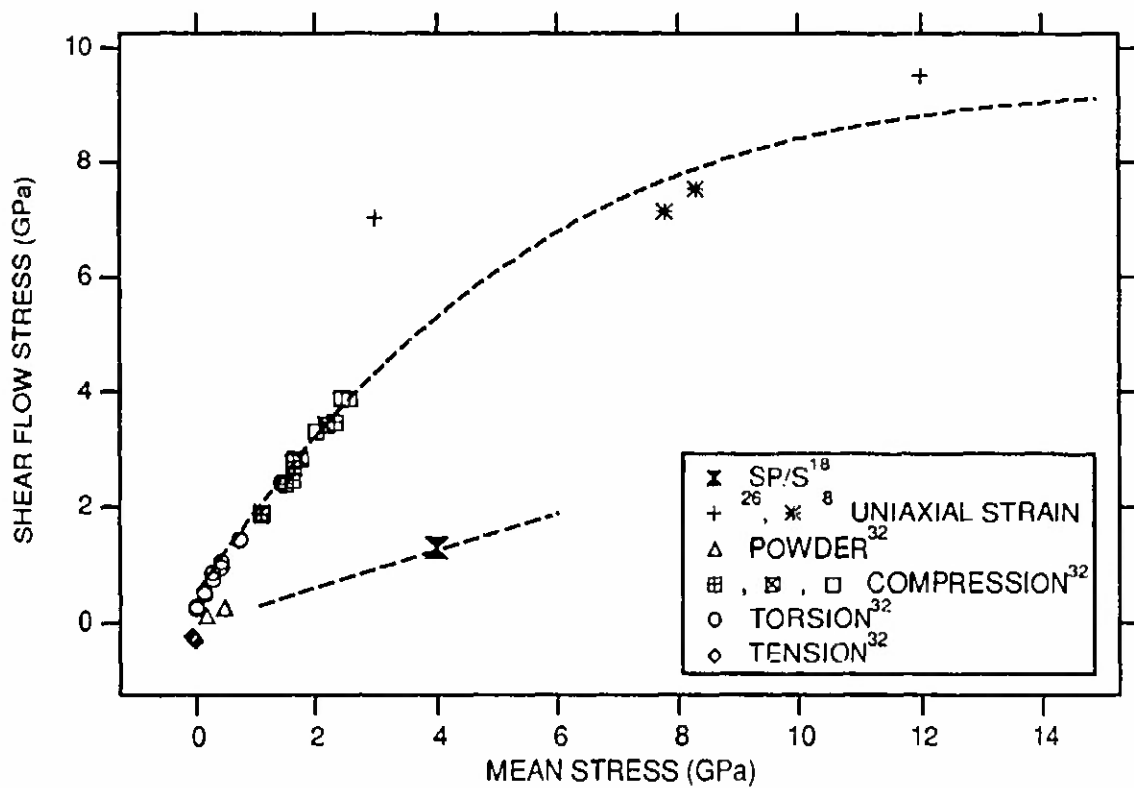
RAM-6795-54

43

Figure 23. Equivalent shear flow stress as a function of mean stress for SiC

From Reference 18.

44

From Figures 20 through 23, we conclude that, with the exception of AlN tested in SP/S, the shear strengths inferred from the pressure/shear tests are lower than the strengths reported by others. As suggested by Klopp and Shockey,[18] we think the reason is that we have essentially measured the response of comminuted ceramic. The longitudinal wave, which is strong enough to caus. damage even in compression, runs ahead of the shear wave. The shear wave, which we measured, is always running through damaged material. Thus, the mean-stress-strength behavior of SiC, for example, measured in pressure/shear is closer to lying along a line through the points of Johnson et al.[28] for ball-milled SiC than along the line connecting data points for intact ceramic (Figure 23).

We established at the outset that any tests for measuring the ballistic behavior of armor ceramics must measure their behavior under penetration conditions (at least until such tests show that ballistic behavior is independent of certain penetration conditions). Both the HSRP/S and SP/S tests have met this requirement, because mean stresses and strain rates characteristic of the Mescall zone were achieved in both. For example, the nominal mean stress and strain rate in the HSRP/S tests on AlN were 11 GPa and 1.3×10^5 s^{-1}, respectively, and Figure 24 shows that the mean stress and plastic shear strain rate were 4 GPa and 1.0×10^4 s^{-1}, respectively, obtained from the Mohr-Coulomb simulation of the SP/S test on AD-85.

The Mohr-Coulomb simulations can reproduce the transverse velocity histories at least qualitatively and, in the cases of AlN tested in HSRP/S and AD-85 and AD-995 Al$_2$O$_3$ tested in SP/S, quantitatively. Matching the AlN and AD-85 velocity histories was essentially a curve-fitting exercise. However, the inability of the simulation to predict the SP/S response of AlN from the HSRP/S results and its ability to predict the SP/S response of AD-995 from the SP/S response of AD-85 are significant.

The response of AlN inferred from the HSRP/S tests is soft. The response inferred from the SP/S test is hard. Since it is unlikely that the SP/S test could indicate a response that is too hard (too high a transverse velocity), the HSRP/S results should be questioned. There are several reasons why an HSRP/S test might indicate too low a transverse velocity and, hence, too soft a response: (1) the impact interface may have slipped and transmitted too little traction into the anvil, (2) the B$_4$C flyer and anvil may have failed in compression by fracturing or yielding in the interior, and (3) the rear surface of the anvil under the TDI diffraction grating or the grating itself may have failed in shear. The evidence supports the third possibility more than the others.

45
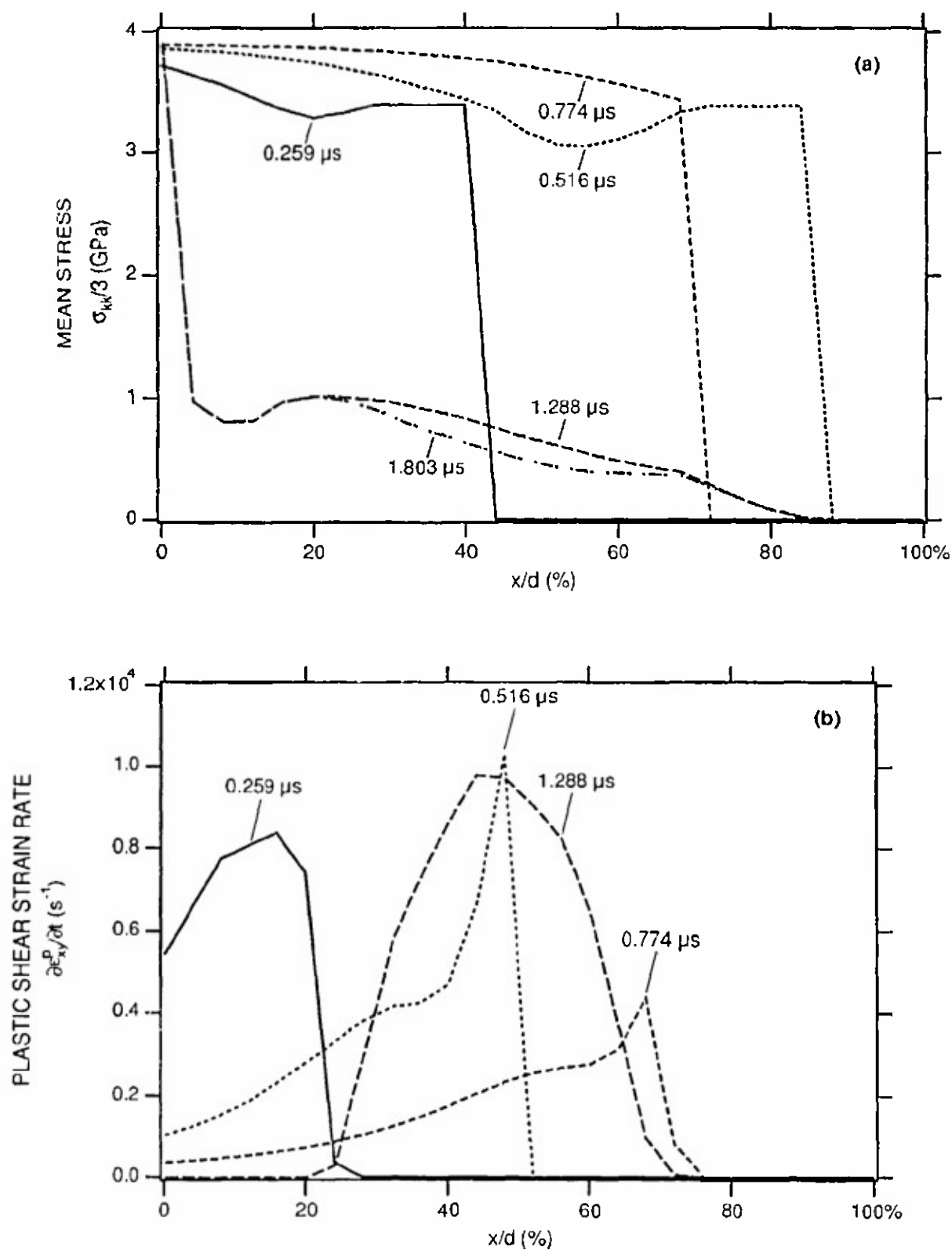
Figure 24.   Mean stress and x - y plastic shear strain rate within the
             anvil at selected times.

46

The evidence against slip is that both polished and sandblasted AD-995 gave the same response (Figure 14). We would expect that, if slip were occurring, changing the frictional characteristics of the impact interface would make a difference. The frictional characteristics of AlN against B_4C may be different from those of AD-995 against itself. The fact that two HSRP/S tests on AlN gave nearly the same response further suggests, however, that slip was not occurring. Slip is probably highly sensitive to cleanliness, roughness, gun chamber vacuum, and projectile blow-by, and these conditions were not identical in the two tests.

The second possibility, that the B_4C failed in compression in the interior, would require that it had been loaded beyond the failure limit in compression/shear. The failure limit of B_4C in uniaxial strain compression, the HEL, is reportedly greater than 14 GPa.[29] The maximum equivalent shear stress that could have been applied to the B_4C, assuming the AlN specimen did not yield, was around 5.4 GPa, whereas the failure limit, assumed to be the equivalent shear stress at the HEL, was around 6.2 GPa. Thus, the B_4C probably did not fail in compression in the interior.

The third possibility, that the B_4C failed near the diffraction grating, seems the most likely. The B_4C probably failed in tension on 45-degree planes when the initial shear wave ran into the unloaded region near the back surface,[17] as indicated in Figure 9. In all the experiments, the 45-degree tensile stresses far exceeded the preshocked spall strengths reported by Grady.[26] In addition, the FRAGBED model includes a simple tension cutoff failure model. In a simulation of AlN loaded in SP/S, the model predicts tensile failure near the location indicated in Figure 9 and the anvil rear surface ends up moving at a greater normal velocity than the normal component of the projectile velocity. Nevertheless, the results show that all the ceramics maintained at least some shear strength after high-amplitude shock and release.

The fact that the same model parameters can match both the AD-85 and AD-995 responses does not mean they have the same mechanical properties. AD-85 is well known to be weaker than AD-995. If the AD-85 had been tested at the same impact velocity (595 instead of 421 m/s) as the AD-995, presumably the AD-85 rear-surface velocity would have been lower. The match between the results shows the fallacy of using the models to extrapolate away from the conditions of a given test. The results are valid at least—perhaps only—for the conditions of a given test. Extrapolation using the current model is not warranted.

47

Chapter 4

OTHER TECHNIQUES

ROD IMPACT

The rod impact technique, or Taylor test, has been applied to metals,[33] polymers,[34] and ceramics.[35] In the test, a circular rod about 4 to 6 diameters long is impacted axially against a "rigid" wall or another like rod. The deformed profile of the rod is recorded with a framing camera[33] or determined posttest, and this profile is compared with that predicted from analysis. The material model in the analysis is adjusted until the analytical and experimental profiles match. The main advantage of the rod impact test over plate impact tests is that less sophisticated experimental facilities are required. The main disadvantage is that the loading on the rod is unknown and complicated and must be inferred from computations, making the quantitative determination of material properties difficult.

Another disadvantage is that the stress state in the rod impact test is nearly uniaxial, and therefore the mean stress can never significantly exceed the deviatoric stress, unlike the stress state ahead of a penetrator. Thus, to be relevant to armor penetration measurements, the test must be modified to increase the mean stress. The modification we used was to contain the rod within a cylinder of another material, thereby constraining radial expansion of the rod.

We simulated a contained rod impact test with a hydrocode and deduced that the stress and strain paths were similar to those occurring ahead of a penetrator. We then performed several rod impact experiments in which a ceramic rod was surrounded by a metal or PMMA and metal containment. Two examples are shown in Figure 25. The ends of the assemblies were impacted by explosively accelerated plates. Because the ceramic rod was unlikely to be recoverable for examination posttest, we hoped that the profile would be recorded in the bore of the containment.

We tried the first configuration shown in Figure 25 (a) and found that, indeed, the rod could not be recovered; the containment also was not recoverable. In an attempt to capture and preserve the ceramic, we designed a blunt tapered flyer that was supposed to explosively weld itself to the containment cylinder (Figure 25b). However, either the flyer velocity was too low relative to its strength or the taper angle was wrong; in any case, welding did not occur.
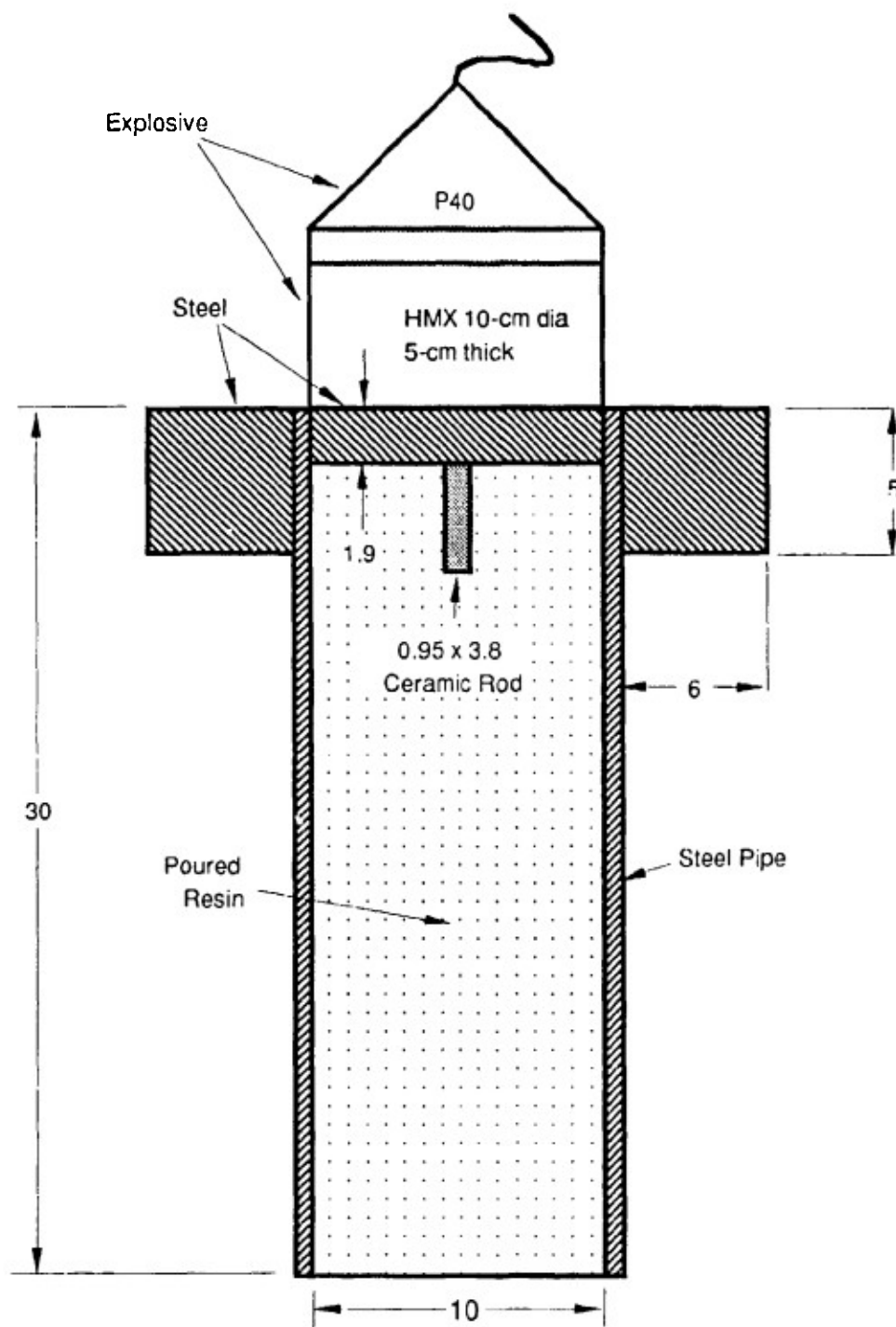
Pipe suspended in a barrel of water.

(a) Resin confinement

RAM-6795-55

Figure 25. Rod impact configurations.

(All dimensions in centimeters)

50

$V_o \approx 1000$ m/s

11.2

Mild Steel

5.1

15°

5.1 Initial
Standoff

R = 2.6

R = 1.6

Epoxy

Ceramic

10

16.8

Foam

Mild Steel

11.1

Mild Steel
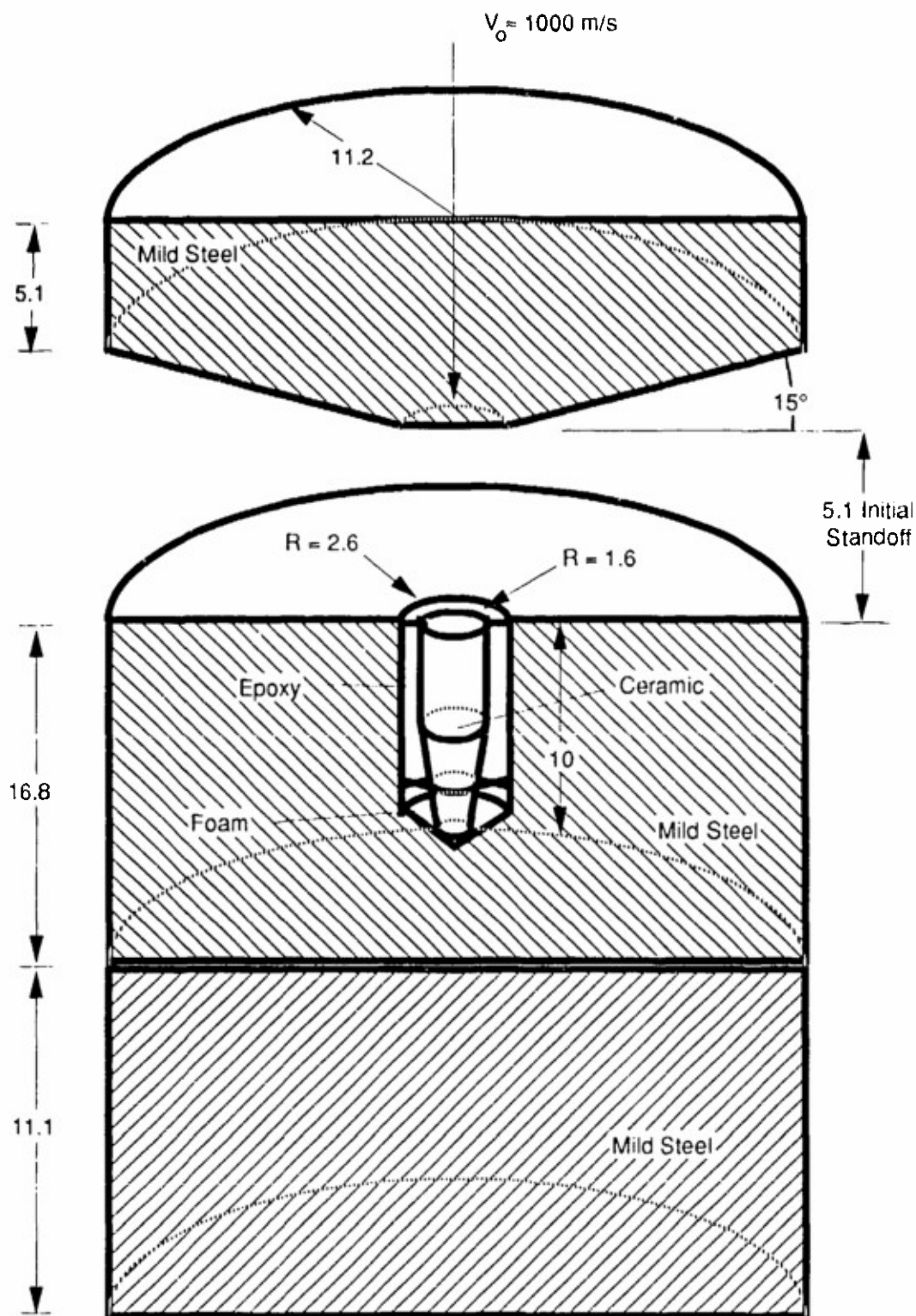
(b) Self-welding confinement.

RAM-6795-56

Figure 25. Rod impact configurations. (Concluded)

(All dimensions in mm)

51

Although some contained-rod impact configuration could be made to work, we did not pursue this problem any further.

CAVITY EXPANSION

The success of cavity expansion analyses[36-38] of modeling penetration suggests that cavity expansion tests would exercise a material under penetration conditions. We have analyzed the expansion of a Mohr-Coulomb (presumably ceramic) cylinder confined within an elastic/ plastic (presumably metal) cylinder (Figure 26), subjected to monotonically increasing internal pressurization. Our analysis is based on Hill's[39] analysis of the expansion of a monolithic tube and is valid from the initial yielding of the ceramic to complete yielding of the metal confinement. We provide relations for the radius of the elastic-plastic boundary, when in either the ceramic or the metal confinement, and the outer radius of the confinement as a function of the internal pressure. The loading is assumed to be quasi-static, plane strain, and the ceramic and metal are modeled as elastic-perfectly-plastic. The Lamé elastic constants for the ceramic and metal are, respectively, λ, μ and λ_s, μ_s. Postyield, the ceramic is assumed to obey a Mohr-Coulomb flow law with a tension cutoff and the metal is assumed to obey Tresca's flow law.

In Figure 26, a and b are the inside and outside radii, respectively, of the ceramic cylinder, and b and d are the inside and outside radii, respectively, of the metal confinement. The radius of the elastic-plastic boundary is c. The yield condition of the ceramic is shown graphically in Figure 27. For monotonic pressurization, stress states are on the branch

$$\sigma_{\theta\theta} = m\sigma_{rr} + Y_T \tag{14}$$

where m is the slope defined in Figure 27, Y_T is the tension cutoff, and σ_{rr} and $\sigma_{\theta\theta}$ are the radial and tangential stress components, respectively. The yield condition is equivalent to

$$\tau \leq fP + T, \tag{15}$$

where τ is the maximum in-plane shear stress, P is the negative of the in-plane mean stress, f is the tangent of the friction angle, and T is the cohesion in shear.

$$m = \frac{1-f}{1+f} \tag{16}$$
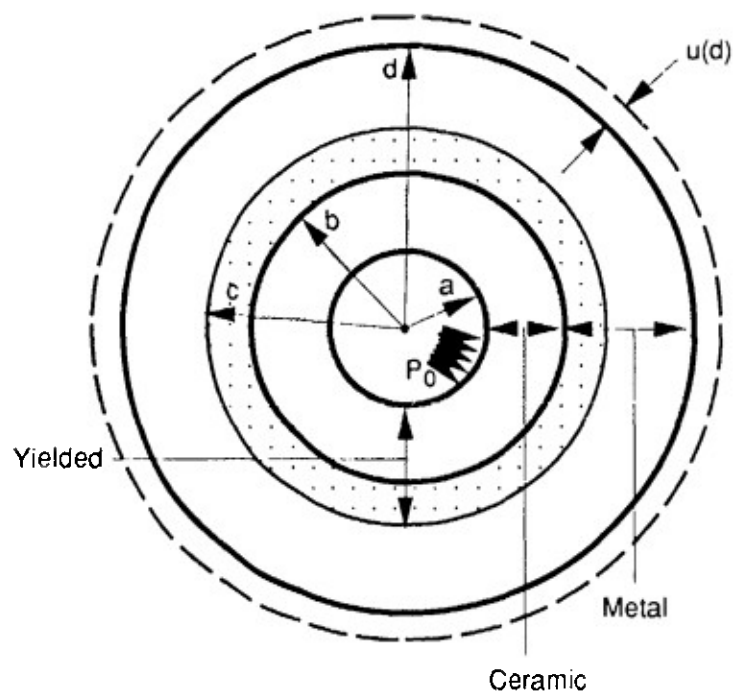
Figure 26. Schematic of cylindrical cavity expansion test.
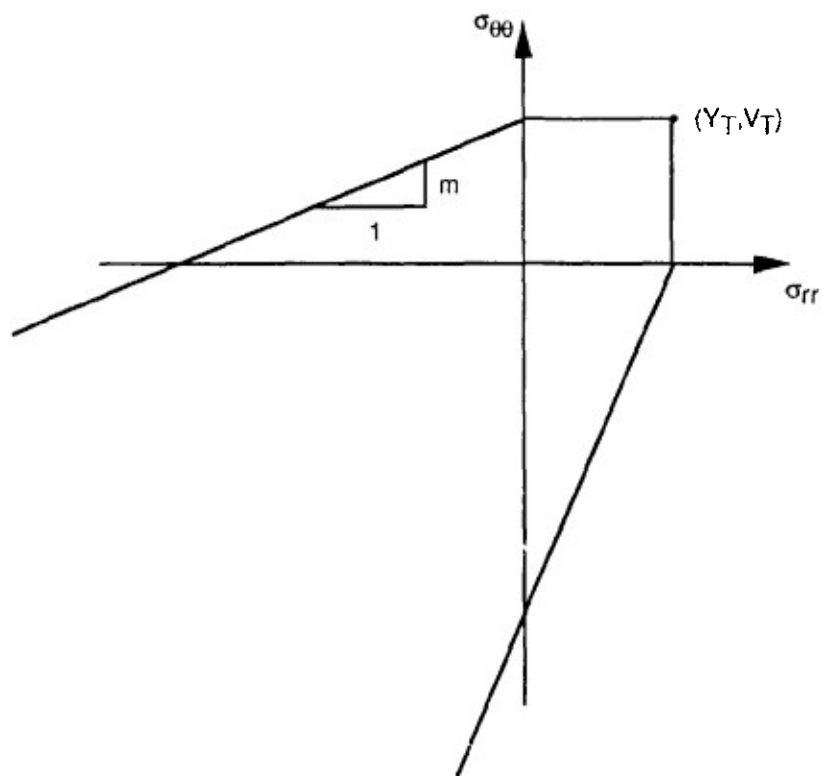
Figure 27. Yield surface for the ceramic in the $\sigma_{rr}-\sigma_{\theta\theta}$ plane.

and

$$Y_T = \frac{2T}{1+f} \qquad (17)$$

The boundary conditions are that $\sigma_{rr} = -P_0$ at $r = a$ and $\sigma_{rr} = 0$ at $r = d$. Further conditions necessary for solving the problem are that the material just inside $r = c$ is at incipient yield and that tractions are continuous across $r = c$. When the elastic-plastic boundary is in the ceramic, the values of c are the roots of

$$-(P_0 + \frac{Y_T}{1-m})(1-m)a^{1-m}c^{m+1} - (P_0 + \frac{Y_T}{1-m})(1+m)a^{1-m}c^{m-1}\hat{d}^2 + Y_T\hat{d}^2\frac{2}{1-m} = 0 \quad (18)$$

where $\hat{d}^2 = \Gamma d^2$ and $\hat{d}$ is the outside radius of a ceramic containment with elastic constants λ, μ equivalent to a metal containment of outside radius d with elastic constants λ_s, μ_s and

$$\Gamma = \frac{\left\{\left[(\lambda+\mu)-(\lambda_s+\mu_s)\right]\mu_s b^2 + (\lambda+\mu+\mu_s)(\lambda_s+\mu_s)d^2\right\}\mu b^2}{\left[\mu_s(\lambda_s+\mu_s+\mu)b^2 + (\mu-\mu_s)(\lambda_s+\mu_s)d^2\right](\lambda+\mu)d^2} \qquad (19)$$

The pressure for initial yielding of the ceramic (i.e., when $c = a$) is given by

$$P_{ya} = \frac{(a^2 - \hat{d}^2)Y_T}{\left[(m-1)a^2 - (m+1)\hat{d}^2\right]} \qquad (20)$$

and the pressure for final yielding of the ceramic ($c = b^-$) is given by

$$P_{yb^-} = \frac{\left\{\left(\frac{a}{b}\right)^{1-m}\left[(1+m)\hat{d}^2 + (1-m)b^2\right] - 2\hat{d}^2\right\}Y_T}{-(1-m)\left\{\left(\frac{a}{b}\right)^{1-m}\left[(1+m)\hat{d}^2 + (1-m)b^2\right]\right\}} \qquad (21)$$

The relation between the internal pressure and the change in the outside radius of the confinement, through final yielding of the ceramic, is given by

$$u = \frac{(\lambda + 2\mu)(\lambda_s + 2\mu_s)Y_T b^2 d}{D} \qquad (22)$$

55

where

$$D = 2(1-m)(\lambda + \mu)\left[\mu_s(\lambda_s + \mu_s + \mu)b^2 + (\mu - \mu_s)(\lambda_s + \mu_s)d^2\right] +$$
$$2(1+m)\frac{\mu}{c^2}\left\{\left[(\lambda + \mu) - (\lambda_s + \mu_s)\right]\mu_s b^4 + (\lambda + \mu + \mu_s)(\lambda_s + \mu_s)b^2 \ d^2\right\} \tag{23}$$

When the elastic-plastic boundary is in the metal, its radius is given implicitly by

$$c = \left\{\frac{2d^2}{Y_s}\left[Y_s \ln\left(\frac{c}{b}\right) + \frac{Y_T}{1-m} - \left(P_0 + \frac{Y_T}{1-m}\right)\left(\frac{a}{b}\right)^{1-m}\right] + d^2\right\}^{1/2} \tag{24}$$

The pressure for initial yielding of the confinement $(c = b^+)$ is given by

$$P_{yb^+} = \left[\frac{Y_T}{1-m} - \frac{Y_s}{2d^2}(b^2 - d^2)\right]\left(\frac{b}{a}\right)^{1-m} - \frac{Y_T}{1-m} \tag{25}$$

and the pressure for complete yielding of the confinement $(c = d)$ is given by

$$P_{yd} = \left[\frac{Y_T}{1-m} + Y_s \ln\left(\frac{d}{b}\right)\right]\left(\frac{b}{a}\right)^{1-m} - \frac{Y_T}{1-m} \tag{26}$$

Finally, the relation between internal pressure and the change in the outside radius of the confinement, through final yielding of the confinement, is given by

$$u(d) = \frac{c^2 d\left[Y_s \ln\left(\frac{c}{b}\right) + \frac{Y_T}{1-m} - \left(P_0 + \frac{Y_T}{1-m}\right)\left(\frac{a}{b}\right)^{1-m}\right](\lambda + 2\mu)}{2(\lambda + \mu)\mu(c^2 - d^2)} \tag{27}$$

Figure 28 shows the plastic zone radius and the confinement radial displacement as a function of the internal pressure for an example set of parameters, given in Table 7. Results are plotted for $f = 0.25, 0.5$, and 0.75. The plots show that, provided the metal confinement is well characterized, the frictional behavior of the ceramic can be inferred from measuring the change in the radius of the confinement or the plastic zone radius. Large relative changes in f lead to large relative changes in $u(d)$ for a given pressure.
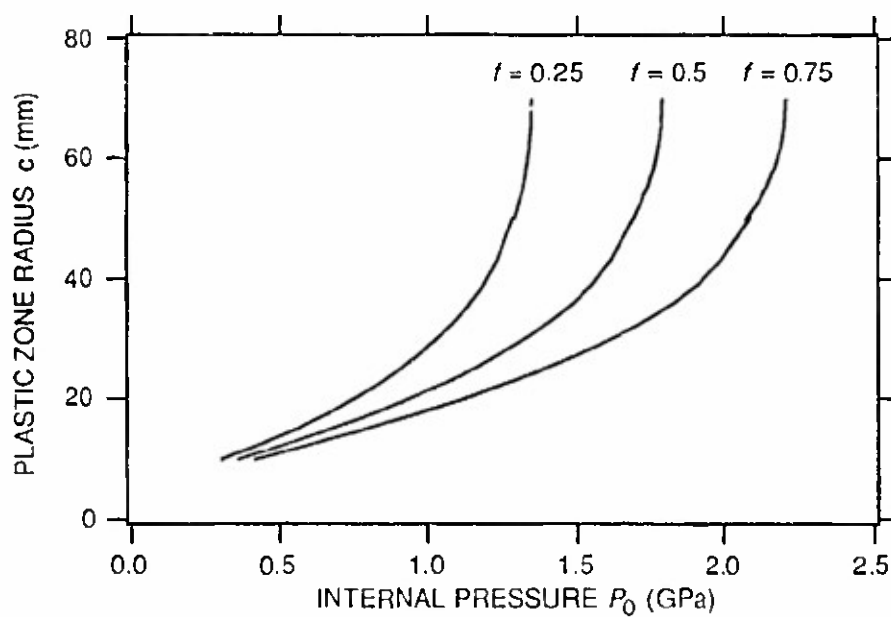
(a) Plastic zone radius
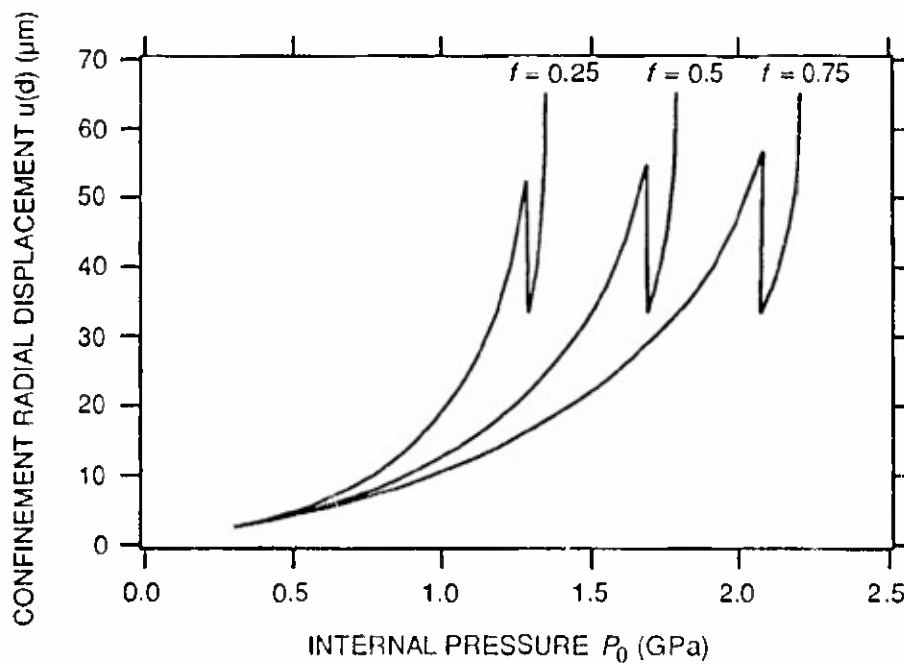
(b) Confinement radial displacement

Figure 28. Plastic zone radius and confinement radial displacement versus internal pressure.

57

Table 7

**PARAMETERS FOR CYLINDRICAL CAVITY
EXPANSION EXAMPLE PROBLEM**

Parameter	Value
a (mm)	10
b (mm)	50
d (mm)	70
λ (GPa)	115
μ (GPa)	147
λ_s (GPa)	119
μ_s (GPa)	80
Y_T (MPa)	500
Y_s (MPa)	350

The above analysis is strictly quasi-static. We would expect, however, that a dynamic analysis taking wave propagation into account would also show that $u(d,t)$ is sensitive to the internal pressure history. The dynamic analysis would apply when the internal pressure is supplied, for example, by the detonation of an explosive.

PENETRATION ARREST EXPERIMENTS

To understand ceramic penetration, we must also understand penetrator erosion. Much of the phenomenology of ceramic penetration can be obtained by sectioning ballistically tested targets. However, penetrators are often completely eroded or otherwise badly deformed after steady-state penetration and little information is available on erosion phenomenology. To better understand erosion, we designed 1/4-scale penetration experiments in which penetration would be arrested partway through the targets.

We shot 6-mm-diameter, 60-mm-long tungsten-nickel-iron (W-Ni-Fe) alloy rods with hemispherical tips into highly confined Coors AD-995 alumina ceramic targets, as shown in Figure 29. Targets were constructed by shrink-fitting steel rings around 25-mm-thick ceramic disks, stacking two such assemblies, and attaching front and back plates with bolts. The ceramic disks were made 13 μm thicker than the rings and 100 μm larger in diameter than the inside diameter of the rings, so that the disks were under an axial prestress of around 20 MPa and a radial prestress of around 500 MPa (both prestresses compressive). The steel parts were heat-treated to HRC 40 before assembly. Impact velocities were around 850 m/s.

Penetration was arrested partway through the targets as desired. The tail of the penetrator was visible through the hole in the cover plate. The ceramic was significantly dilated as evidenced by the bulging of the front plate, opening of gaps between the rings, and stretching of the bolts. Unfortunately, we did not have sufficient time or funds to section the targets and examine the penetrators. We recommend that sectioning be pursued in a future program. We have available several more AD-995 targets and targets of TiB_2. We also have six uranium-3/4% titanium (DU-3/4Ti) penetrators. By performing further experiments, we can compare the erosive properties of AD-995 and TiB_2 and the erosion resistance of DU-3/4 Ti and W-Ni-Fe alloys.

59

Steel Confinement   Ceramic

← 51 mm →

(a) Target

Entry Hole

Copper Sabot

6 mm

Tungsten Penetrator
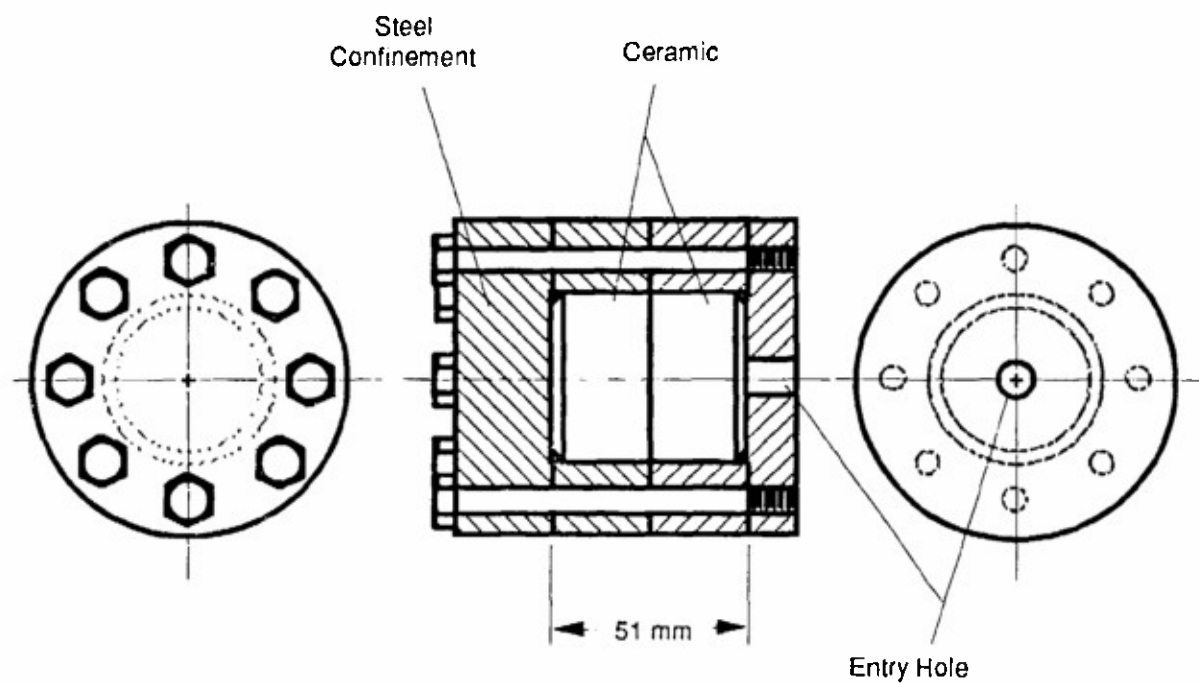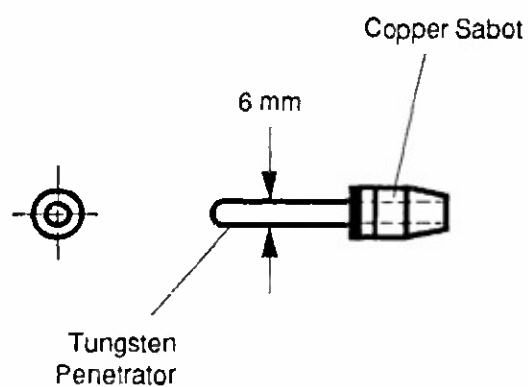
(b) Penetrator

RAM-6795-60

Figure 29. Apparatus for penetration arrest experiments.

60

Chapter 5

CONCLUSIONS AND RECOMMENDATIONS

CONCLUSIONS

From the results of the research performed in this program, we reached the following conclusions:

- Penetration of a confined ceramic block by an impacting long rod projectile occurs by the comminution of a zone of the ceramic at the leading edge of the projectile and the flow of the fine fragments out of the projectile path.

- The material properties governing the penetration resistance of a confined ceramic block include the dynamic compressive strength, the comminution and granular flow resistance under high rate and high pressure conditions, and the abrasiveness of the ceramic fragments.

- Pressure/shear tests in two configurations with rear surface laser diagnostics and with appropriate constitutive analysis are suitable for measuring the high pressure, high strain rate comminution and granular flow properties of armor ceramics.

RECOMMENDATIONS FOR FUTURE WORK

Our research on the phenomenology of penetration, the development of tests for measuring governing properties, and the application of those tests to candidate armor ceramics suggest many avenues for future research, in terms of both specific test techniques and armor design in general.

One issue that needs to be addressed is whether the pressure/shear anvils fail in 45-degree tension when the shear wave runs into uncompressed material. One way to remove doubt in future experiments is to simply prevent shear failure. A sapphire window placed behind the anvil, as implemented by Espinosa and Clifton,[17] delays longitudinal unloading and ensures that the shear wave always runs into compressed specimen material. Another way is to use in-material gages to make measurements nearer the impact plane than the potential shear failure plane. For nonconductive ceramics, the magnetic particle velocity technique developed by Gupta et al.[40] is a proven method for making such measurements. Both types of experiments are

recommended, because the latter technique cannot be applied to conductive ceramics such as TiB$_2$, whereas the former technique is restricted to cases in which the sapphire does not yield.

A second issue that should be addressed is whether slip occurs between the impacting plates. The magnetic particle velocity technique can also be applied to resolve this question. If slip is not occurring in a symmetric pressure/shear experiment, the particle velocity detected by a gage located on the impact face of the anvil will jump to half the impact velocity and remain there for the duration of the one-dimensional part of the experiment. Any variation in velocity, in an otherwise perfectly symmetric, planar impact, indicates that slip is occurring.

To reduce ambiguity in the measured stress-strain response of very hard ceramics like TiB$_2$, SiC, and B$_4$C, we recommend HSR pressure/shear experiments using flyer and anvil plates of cubic boron nitride (CBN). Since CBN has a higher Hugoniot elastic limit than these candidate armor ceramics, the flyer and anvil plates will remain elastic at the high impact velocities required to fail the specimen materials, allowing a direct determination of the stress-strain response. CBN is available relatively cheaply in disks 25 mm in diameter and 2 mm thick as a cutting tool material.

The fragmentation and flow models should be further developed. The Mohr-Coulomb model we used is largely empirical; how the parameters in the model relate to physical properties and processes in the material is unclear. The block-sliding model, FRAGBED, is more physically based, but is incomplete. We recommend that FRAGBED be modified to include details of the fracture and fragmentation process. The result will be improved understanding of fragment size and shape evolution, fragment interaction, and the possible interplay of plastic (dislocation-based) deformation and fragmentation. The relationship between model parameters and physics would be more clear. The model would be used for simulating both SP/S experiments and ballistic penetration.

Our data base of pressure/shear results is limited in the number of ceramics tested and the range of mean stress and strain rates covered. We recommend that additional pressure/shear tests be performed, particularly on ceramics of common interest to other investigators, such as AD-995, and to designers, such as TiB$_2$.

An investigation into penetrator erosion is recommended. The following questions needing to be addressed: What ceramic properties or ceramic fragment characteristics control penetrator erosion rates? How do abrasive wear and plastic flow relate to erosion? If sharp,

angular fragments erode penetrators better, what properties control fragment morphology, and can these properties be enhanced without degrading other important properties?

We still need a simple, inexpensive test that exercises ceramics under penetration conditions, because the pressure/shear tests described here require a sophisticated gas gun facility with accompanying interferometers and high-speed recording equipment. We recommend that the search for a simpler test begin with continued investigation of the cylindrical cavity expansion test. That test requires an explosives test capability and the capability to machine cylinders of armor ceramics, but no more sophisticated instrumentation than a micrometer is required to measure the diameter of the confinement before and after the test. Our results show that the granulation and flow properties of armor ceramics are relatively insensitive (compared with metals, say) to loading rate, but are sensitive to mean stress. Thus, a simpler static test may be possible, but only if sufficiently large mean stresses can be applied. A dynamic test may be necessary, if only to attain sufficiently large mean stress.

REFERENCES

1. D. A. Shockey, A. H. Marchand, J. E. Crocker, and R. W. Klopp, "Dynamic Failure Behavior of Ceramic Targets and Textured Tungsten Alloy Rods," Final Technical Report on Contract No. 9-X69-3295Z-1, Los Alamos National Laboratory, SRI Project 7525 (November 1991).

2. D. A. Shockey, A. H. Marchand, S. R. Skaggs, G. E. Cort, M. W. Burkett, and R. Parker, "Failure Phenomenology of Confined Ceramic Targets and Impacting Rods," *Int. J. Impact Eng.* **9**(3), 1 (1989).

3. J. Lankford, "The Compressive Strength of Strong Ceramics: Microplasticity versus Microfracture," *J. Hard Mater.* **2**, 55-77 (1991).

4. D. R. Curran, L. Seaman, T. Cooper, and D. A. Shockey, "Micromechanical Model for Comminution and Granular Flow of Brittle Material under High Pressure and High Strain Rate: Application to Penetration of Ceramic Armor," submitted to *Int. J. Impact Eng.* (1992).

5. J. Mescall and C. Tracy, "Improved Modeling of Fracture in Ceramic Armor," Proceedings of the 1986 Army Science Conference, U.S. Military Academy, West Point, 17-20 June 1986.

6. J. Mescall and W. Weiss, "Materials Behavior under High Stress and Ultrahigh Loading Rates–Part II," Proceedings of the 29th Sagamore Army Conference, Army Materials and Mechanics Research Center, Watertown, MA (1984).

7. T. Cooper, "A Computer Code for Numerical Simulation of Shock Waves in Fluids and Solids," Report DS 1980:16, Swedish Detonic Research Foundation, Stockholm, Sweden (1980).

8. M. E. Kipp and D. E. Grady, "Shock Compression and Release in High-Strength Ceramics," Sandia Report SAND89-1461•UC-704 (July 1989).

9. D. C. Erlich, "Adaptations to Existing Gas Guns to Increase Impact Velocity and Flyer Plate Diameter," Proceedings of the 42nd Aeroballistic Range Association Meeting, 21-25 October 1991, Adelaide, South Australia.

10. R. W. Klopp, "Fiber-Optic Interferometers," Poulter Laboratory Technical Report 001-89, SRI International, Menlo Park, California (1989).

11. P. Kumar and R. J. Clifton, "Optical Alignment of Impact Faces for Plate Impact Experiments," *J. Appl. Phys.* **48**, 1366-1367 (1977).

12. A. S. Abou-Sayed, R. J. Clifton, and L. Hermann, "The Oblique Plate Impact Experiment," *Exp. Mech.* **16**, 127-132 (1976).

13. C. H. Li, "A Pressure-Shear Experiment for Studying the Dynamic Plastic Response of Metals at Shear Strain Rates of 10^5 s^{-1}," Ph.D. Thesis, Brown University, Providence, Rhode Island (1981).

14. R. J. Clifton and R. W. Klopp, "Pressure-Shear Plate Impact Testing," *Metals Handbook*, Vol. 8., 9th ed. (ASM International, Metals Park, Ohio 1985), pp. 230-239.

15. K. S. Kim, R. J. Clifton, and P. Kumar, "A Combined Normal- and Transverse-Displacement Interferometer with an Application to Impact of y-Cut Quartz," *J. Appl. Phys.* 48(10), 4132-4139 (1977).

16. M. J. Rudd, "A New Theoretical Model for the Laser Dopplermeter," *J. Phys. E.* 2(2), 55-58 (1969).

17. H. D. Espinosa and R. J. Clifton, "Plate Impact Experiments for Investigating Inelastic Deformation and Damage in Advanced Materials," in *Experiments in Micromechanics of Failure-Resistant Materials*, K. S. Kim, Ed. (ASME, New York, 1991).

18. R. W. Klopp and D. A. Shockey, "The Strength Behavior of Granulated Silicon Carbide at High Strain Rates and Confining Pressure," *J. Appl. Phys.* 70(12), 7318-7326 (1991).

19. A. S. Abou-Sayed and R. J. Clifton, "Analysis of Combined Pressure-Shear Waves in an Elastic/Viscoplastic Material," *J. Appl. Mech.* 44, 79-84 (1977).

20. P. Perzyna, "Fundamental Problems in Viscoplasticity," *Adv. Appl. Mech.* 9, 243-377 (1966).

21. J. W. Rudnicki and J. R. Rice, "Conditions for the Localization of Deformation in Pressure-Sensitive Dilatant Materials," *J. Mech. Phys. Solids* 23, 371-394 (1975).

22. S. Ranganath and R. J. Clifton, "A Second-Order Accurate Difference Method for Systems of Hyperbolic Partial Differential Equations," *Comput. Methods Appl. Mech. Eng.* 1, 173-188 (1972).

23. L. Seaman, "Development of a Model for Shear Banding: SHEAR 3," Final Report, Vol. 2, Contract DAAK11-78-C-0115 to Ballistics Research Laboratory, SRI Project No. PYU-7893 (April 1983).

24. H. C. Heard and C. F. Cline, "Mechanical Behavior of Polycrystalline BeO, Al_2O_3, and AlN at High Pressure," *J. Mater. Sci.* 15(8), 1889-1897 (1980).

25. J. Lankford, personal communication (November 1989).

26. D. E. Grady, "Dynamic Material Properties of Armor Ceramics," Sandia Report SAND91-0147•UC-704 (March 1991).

27. Z. Rosenberg, N. S. Brar, and S. J. Bless, "Dynamic High Pressure Properties of AlN Ceramic as Determined by Flyer Plate Impact," submitted to *J. Appl. Phys.* (1992).

28. Y. Yeshurun, Z. Rosenberg, D. G. Brandon, and N. A. Travitzky, "Effect of Heat Treatment on the Dynamic Response of Commercial 85 wt% Al_2O_3," *Mat. Sci. and Engng.* **71**, 71-75 (1985).

29. M. L. Wilkins, "Use of Boron Compounds in Lightweight Armor," in *Boron and Refractory Borides*, V. I. Matkovich, Ed. (Springer-Verlag, Berlin, 1977).

30. W. H. Gust and E. B. Royce, "Dynamic Yield Strengths of B_4C, BeO, and Al_2O_3 Ceramics," *J. Appl. Phys.* **42**(1), 276-295 (1971).

31. Z. Rosenberg and Y. Yeshurun, "The Relation Between Ballistic Efficiency and Compressive Strength of Ceramic Tiles," *Int. J. Impact Engng.* **7**(3), 357-362 (1988).

32. G. R. Johnson, T. J. Holmquist, J. Lankford, C. E. Anderson, and J. Walker, "A Computational Constitutive Model and Test Data for Ceramics Subjected to Large Strains, High Strain Rates, and High Pressures," Final Technical Report for Optional Task 1, Department of Energy Contract DE-AC04-87AL-42550, Advanced Technology Assessment Center, Los Alamos National Laboratory (August 1990).

33. D. C. Erlich and P. Chartagnac, "Determination of Dynamic Flow Curve of Metals at Ambient and Elevated Temperatures by Rod Impact Techniques," *J. de Physique*, Colloque C5, supplément au no. 8, Tome 46, C5-455-462 (1985).

34. D. C. Erlich and L. Seaman, "Dynamic Failure of Energetic Propellants," SRI International unpublished results (1990).

35. N. S. Brar and S. J. Bless, in *Proceedings of the International Conference on Shock-Wave and High-Strain-Rate Phenomena in Materials* (EXPLOMET 90), M. A. Meyers, L. E. Murr, and K. P. Staudhammer Eds. (Dekker, New York, 1991).

36. R. F. Bishop, R. Hill, and N. F. Mott, "The Theory of Indentation and Hardness Tests," *Proc. Phys. Soc.* **57**, 147-159 (1945).

37. M. J. Forrestal, D. B. Longcope, and F. R. Norwood, "A Model to Estimate Forces on Conical Penetrators into Dry Porous Rock," *J. Appl. Mech.* **48**, 25-29 (1981).

38. A. L. Florence, P. R. Gefken, L. Seaman, D. R. Curran, and D. A. Shockey, "Computational Models for Armor Penetration," SRI International Technical Report on Project 8521, prepared for Alliant Techsystems, Inc., on Contract No. 635848-FN (January, 1992).

39. R. Hill, *The Mathematical Theory of Plasticity* (Oxford University Press, London, 1950).

40. Y. M. Gupta, D. D. Keough, D. F. Walter, K. C. Dao, D. Henley, and A. Urweider, "Experimental Facility to Produce and Measure Compression and Shear Waves in Impacted Solids," *Rev. Sci. Instrum.* **51**(2), 183-194 (1980).

Appendix
PUBLICATIONS AND PRESENTATIONS

**ADAPTATIONS TO EXISTING GAS GUNS TO INCREASE
IMPACT VELOCITY AND FLYER PLATE DIAMETER**

ADAPTATIONS TO EXISTING GAS GUNS TO INCREASE IMPACT VELOCITY AND FLYER PLATE DIAMETER

by

DAVID C. ERLICH

Poulter Laboratory

SRI International

333 Ravenswood Ave.

Menlo Park, Ca   94025

for

ABSTRACT

Adaptations were recently n..de to the two light gas guns at SRI International's
Poulter Laboratory to improve their versatility as research tools. An alternative breech plug
configuration was created for the smaller (2.5-in.-diameter) gas gun, resulting in a nearly
50% increase in impact velocity, and a new projectile/target/recovery system was designed
and built for use in the larger (4-in.-diameter) gas gun that allows planar impact of plates up
to 12 in. in diameter at relatively low velocities. This paper will briefly describe the two
gas guns, discuss the motivations for making the changes, then show in detail the design
and operation of the new configurations.

2.5-IN. GAS GUN: BREECH MODIFICATION
FOR HIGHER VELOCITIES

DESCRIPTION

SRI International's 2.5-in. gas gun has been in operation for about 30 years and was last modified in 1977. This modification involved slotting the barrel and adding to each projectile a key that rides in the slot, thus preventing projectile rotation and allowing planar impact of a slanted flyer and target with negligible tilt.

The standard wraparound breech configuration (shown in Figures 1 and 2a) has the projectile acting as the rapid-opening breech valve. With the projectile latched in place, the barrel ahead of and behind it is evacuated and the reservoir is pressurized to a maximum of ≈ 6000 psi. To activate a launch, the projectile is unlatched and high-pressure gas from the reservoir is allowed through the evacuation tube into the region behind the projectile, pushing it forward and unblocking the reservoir opening.

The projectile walls must be relatively strong (a minimum wall thickness of ≈ 5 mm of 7075-T6 aluminum in the region of the reservoir opening) to withstand the high pressure of the gas prior to launch; and therefore, the projectile is relatively heavy (from ≈ 500 to 1200 g). The results of the 549 tests performed from 1977 to 1989 are shown in Figure 2, plotted in terms of impact velocity (V) versus gas pressure divided by projectile mass (P/M). The highest impact velocity has been 677 m/s, using a custom projectile (with outrigger for slanted impact) designed for minimal mass. The projectile weighed 535 g, and the tests had a gas pressure of 5980 psi (P/M of 11.2).

3
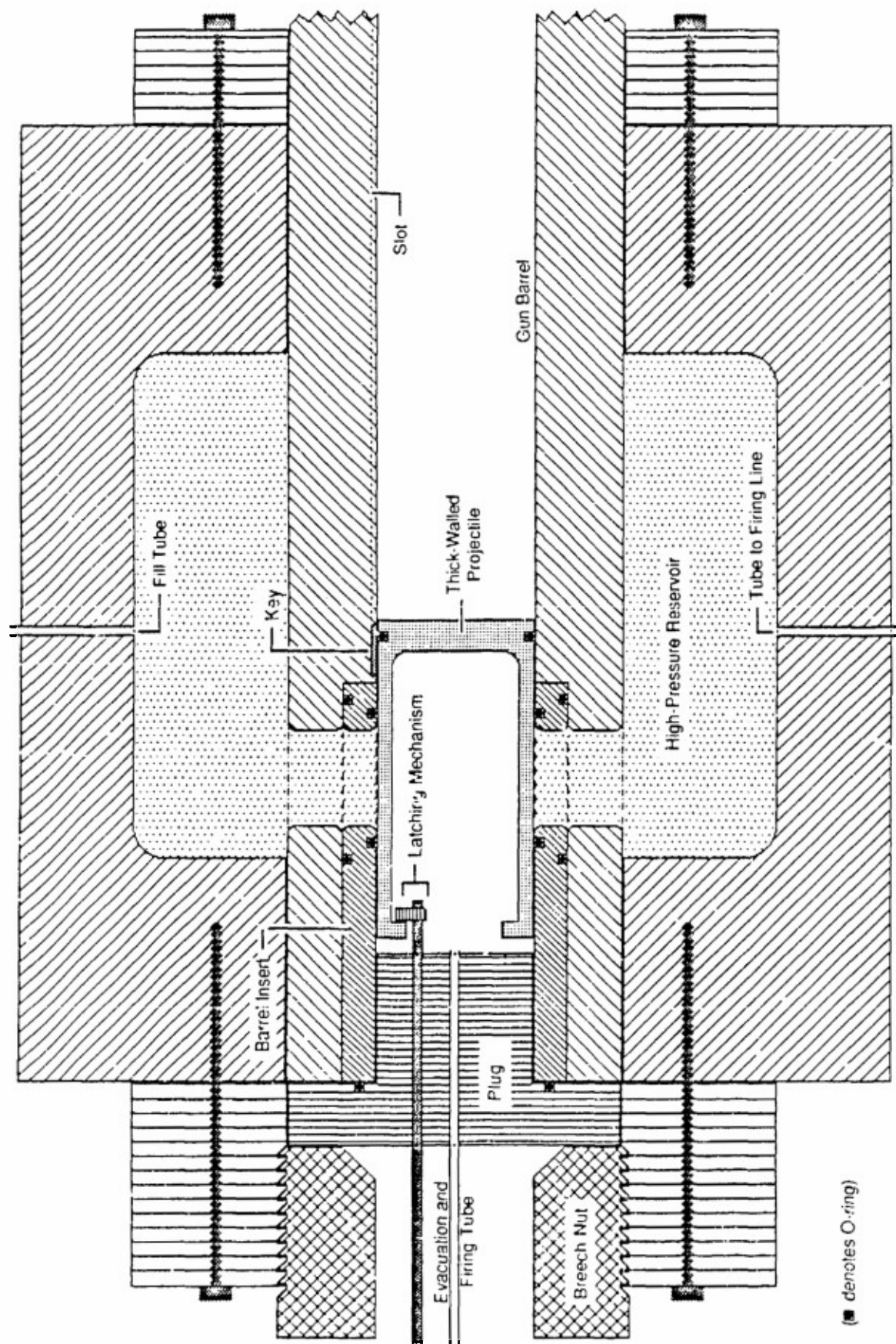
Figure 1. Standard wraparound breech configuration for 2.5 in. gas gun.

CAM 318543 1

Slot

Gun Barrel

Fill Tube

Key

Thick-Walled Projectile

Latching Mechanism

High-Pressure Reservoir

Tube to Firing Line

Barrel Insert

Plug

Evacuation and Firing Tube

Breech Nut

(■ denotes O-ring)

4

(a) Standard Wrap-around Breech (showing normal impact)

(b) New Higher-Velocity Breech (showing slanted impact)
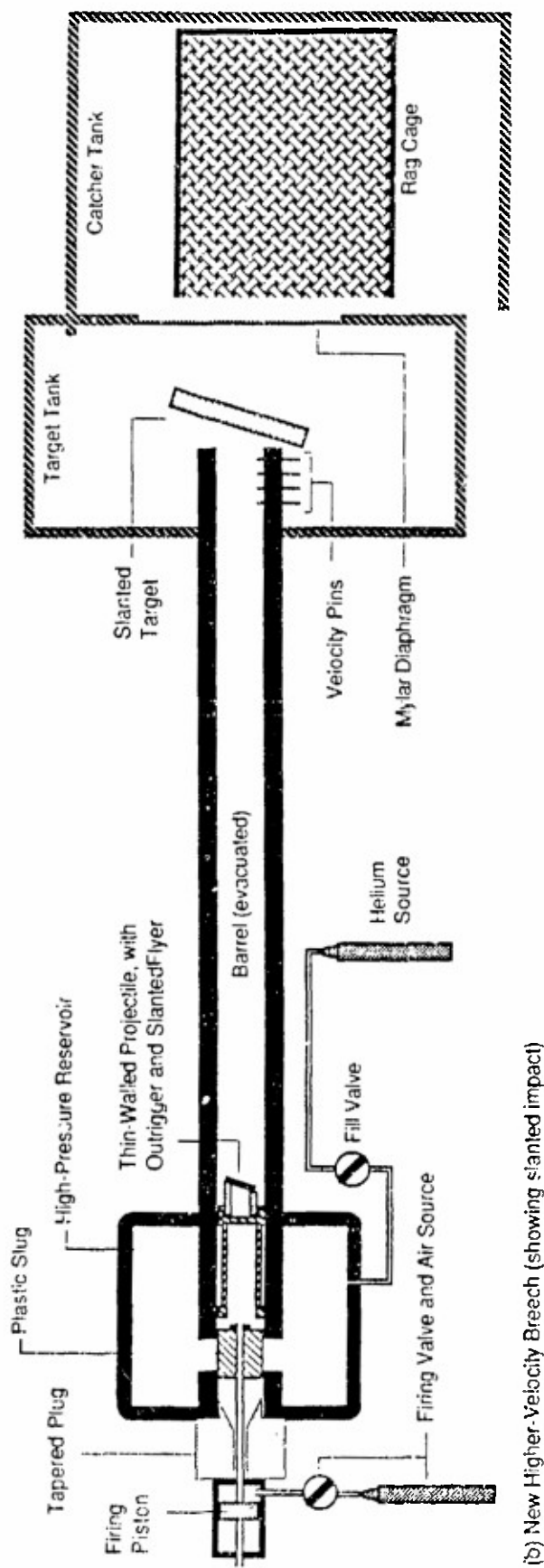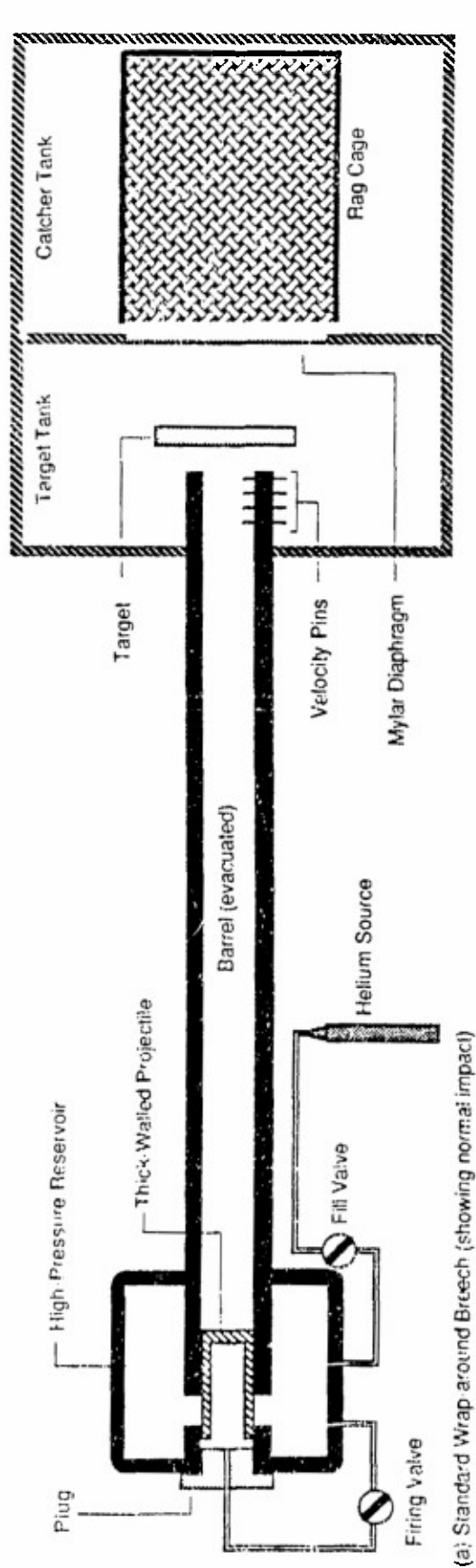
Figure 2. Schematic of alternative 2.5-in. gas gun breech configurations.

CAM-314543-2

5

MOTIVATION FOR CHANGE

Recently there has been interest in gas gun tests of high-strength ceramics, such as silicon carbide (SiC), boron carbide (B_4C) and titanium diboride (TiB_2), that have Hugoniot elastic limits (HEL) in the 150-kbar range. One such test, called the pressure-shear test,[*] involves slanted impact to produce shear stresses strong enough to yield the material. Back-surface interferometry is used to characterize the dynamic flow properties of the ceramic .

Impact velocities on the order of 900–950 m/s are required to obtain the desired stresses. Figure 3 shows an extrapolation of the V-P/M curves to 1000 m/s, using a power law fit to the lower-velocity data. The P/M value would need to increase by $\approx$150% (from $\approx$11 to $\approx$27) to obtain the 50% increase in V over the highest previously attained value of 677 m/s. Because we are already at the upper limit of gas pressure ($\approx$6000 psi), we must reduce the projectile mass by 60% (from $\approx$550 to $\approx$220 g).

After we examined many possibilities for redesigning the projectile (including changing the composition of the walls, reducing the wall thickness and filling the inside with a light foam, and ribbing the walls), it became clear that nothing would effect such a major reduction in the projectile mass as long as the projectile needed to withstand the 6000-psi gas pressure. We concluded that we had to redesign the breech configuration to eliminate the use of the projectile as a breech valve. We strived to minimize (1) the costs by using as many existing breech components as possible and (2) the time required to switch back and forth between the new and the old breech configurations.

---

[*]R. J. Clifton and R. W. Klopp, "Pressure-Shear Plate Impact Testing," in *Metals Handbook*, Vol. 8, 9th Edition, ASM International, Metals Park, Ohio (1985).
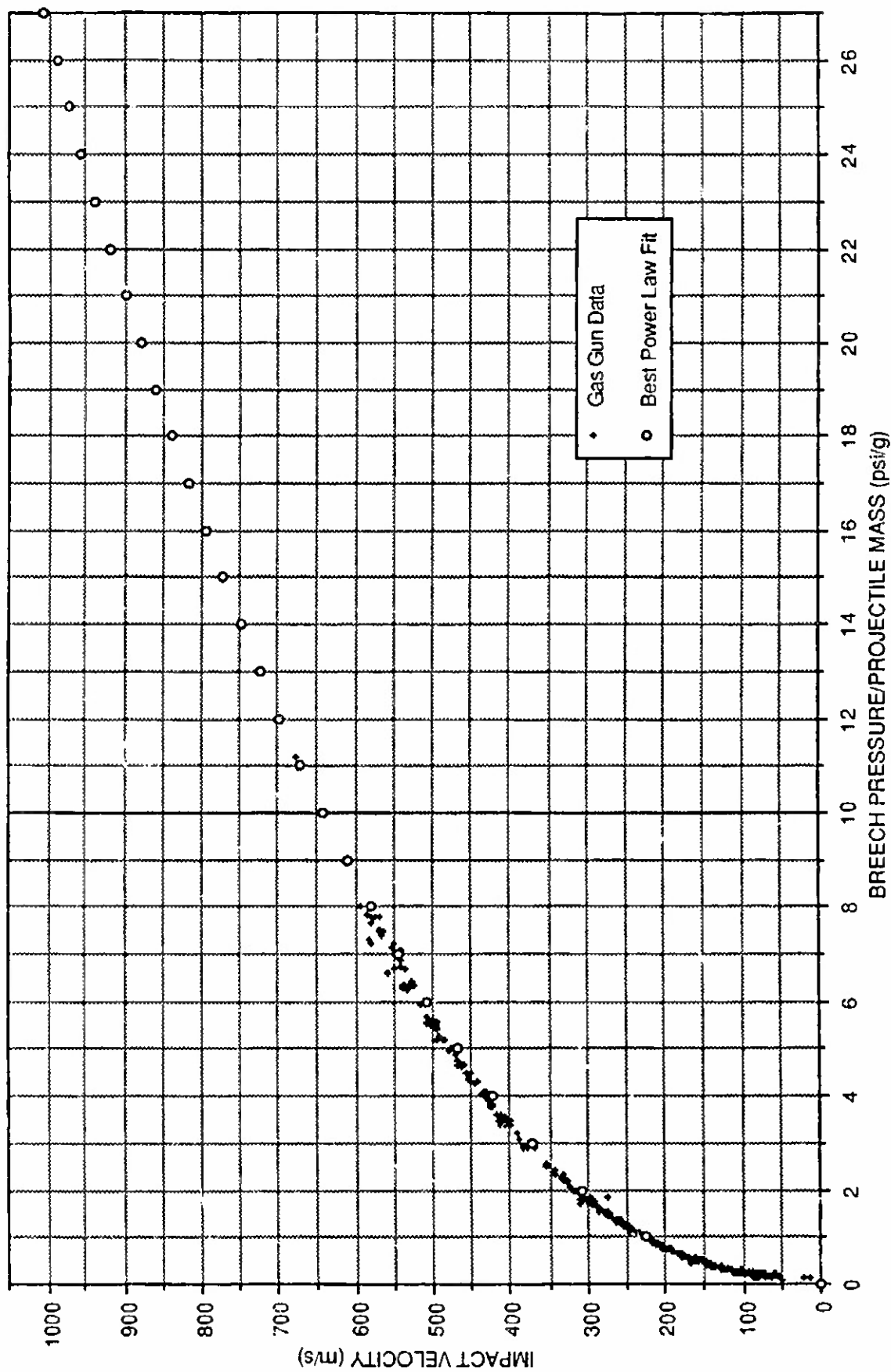
Figure 3. 2.5-in. gas gun: 1977-89 data and extrapolation to higher impact velocities.

CAM-318543-3

7

NEW HIGHER-VELOCITY BREECH CONFIGURATION

The newly designed and implemented higher-velocity breech configuration is shown in Figures 2b and 4. A solid polycarbonate cylinder replaces the projectile as the breech valve, while the projectile, a new ultralight, thin-walled design, is positioned in the barrel ahead of the reservoir opening. The plastic slug is attached by a tube to a piston in a cylinder outside the barrel. The tube, which is also used to evacuate the region behind the projectile, passes through a tapered high-strength steel breech plug.

The modifications were relatively inexpensive to implement, because only two components of the standard breech configuration needed to be replaced by machined parts. The barrel insert was redesigned to include a shoulder (against which the plastic slug and the projectile are positioned) and holes for the latching pins. A new tapered breech plug replaces the original plug.

When the gun is fired, compressed air pushes the piston, which pulls the front end of the plastic slug past the reservoir opening. At that point, high-pressure gas from the reservoir flows into the barrel, driving the plastic slug backward (further opening the reservoir) and, after enough pressure is attained to shear off the latching pins (a few hundred psi), propelling the projectile forward. The reservoir opening time is expected to be about the same for this configuration as for the standard wraparound breech. The plastic slug is severely deformed and is eventually stopped by the taper of the breech plug.

The ultralight projectile design is shown in Figure 5. The material is still 7075-T6 aluminum, but the wall thickness has been reduced to a mere 1.6 mm. The design allows the gas to flow to the outside as well as the inside of the wall, which serves simply as a guide to keep the front of the projectile ($\approx$5 mm thick, to withstand the high pressure) in alignment. The mass of the projectile shown in Figure 5 is about 235 g, depending on the

8
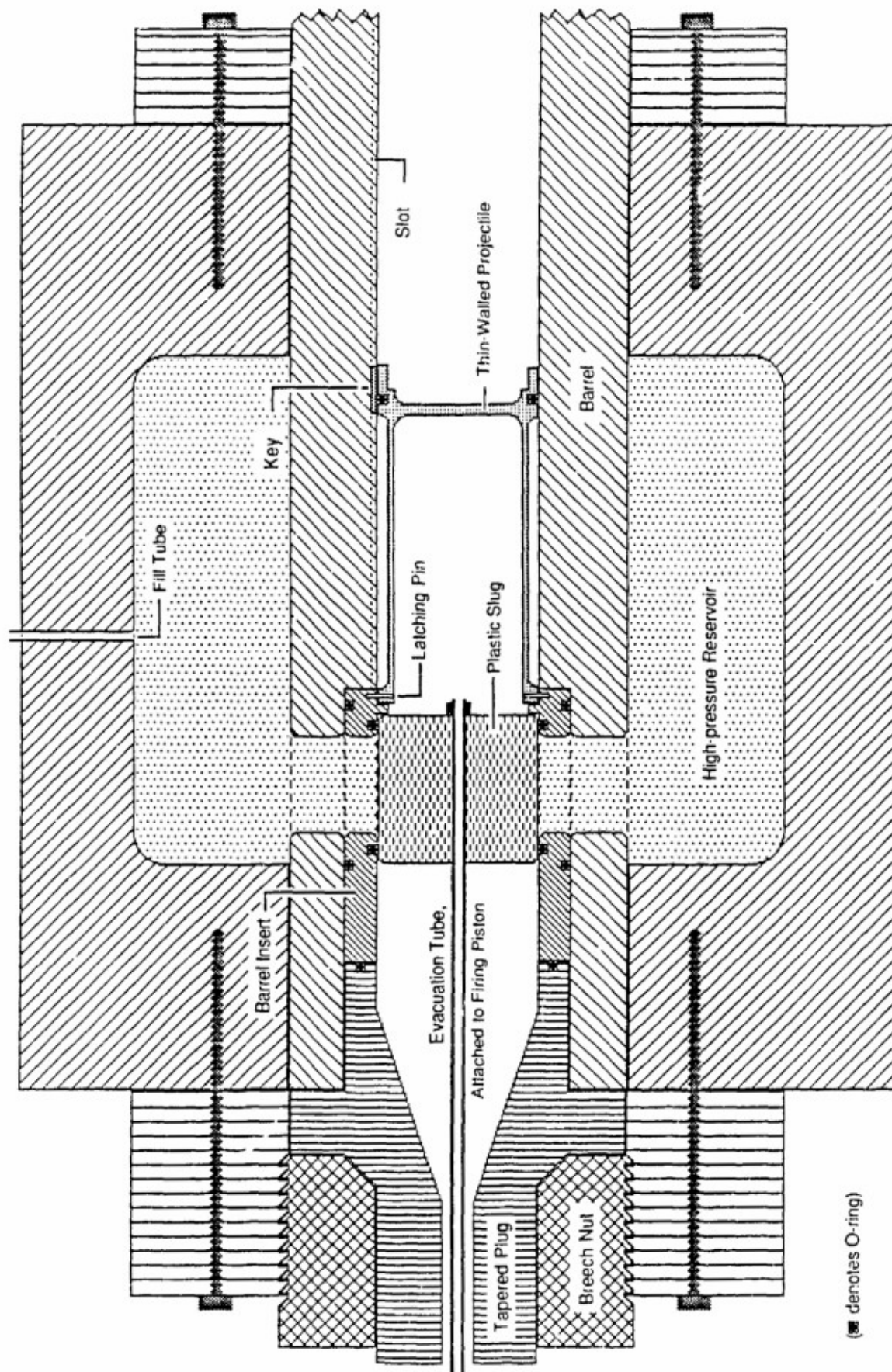
Figure 4. New higher-velocity breech configuration for 2.5-in. gas gun

Labels in figure:

Slot

Thin-Walled Projectile

Key

Barrel

Fill Tube

Latching Pin

Plastic Slug

High-pressure Reservoir

Barrel Insert

Evacuation Tube,

Attached to Firing Piston

Tapered Plug

Breech Nut

(▓ denotes O-ring)

CAM 31654-3 4

9
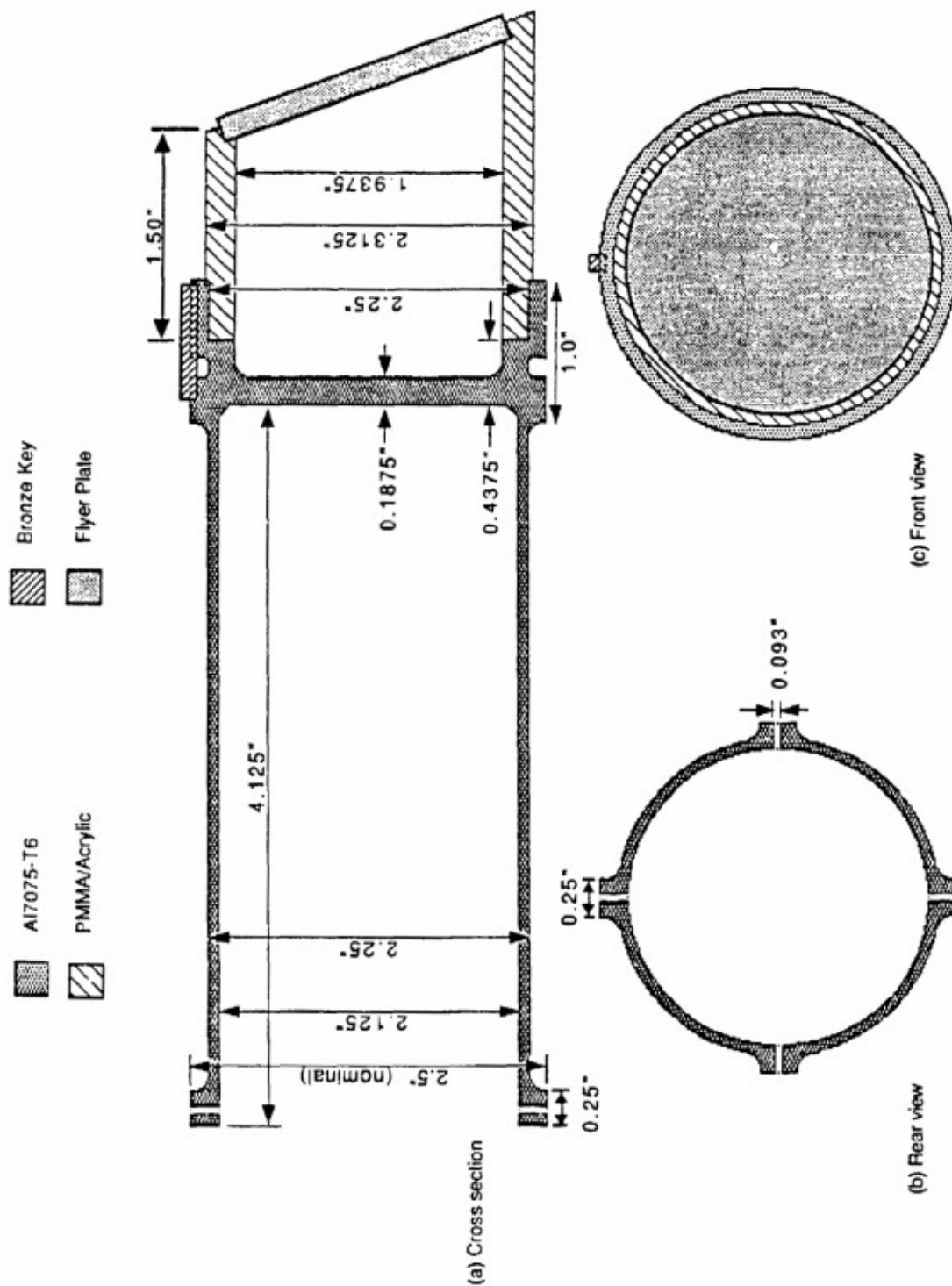
Figure 5. Ultralight projectile for 20 degree slanted impact using 2.5-in. gas gun higher-velocity breech system.

CAM-31854 3.5

(a) Cross section

(b) Rear view

(c) Front view

Bronze Key

Flyer Plate

Al7075-T6

PMMA/Acrylic

10

density and thickness of the flyer plate. Further reductions can be made by reducing the projectile's length and cutting holes in its side walls.

Thus far, four experiments have been performed with the new breech configuration, shown in Figure 6. The highest velocity attained has been 939 m/s, using a projectile with a mass of 223 g (breech pressure was 6090 psi, resulting in a P/M of 27.2 g). The velocity was a only a few percent below that predicted for the same P/M by the power law extrapolation from lower-velocity data. The measured impact tilt has been as low as 0.6 mRad, which is comparable to the best attained using the standard wraparound breech configuration.
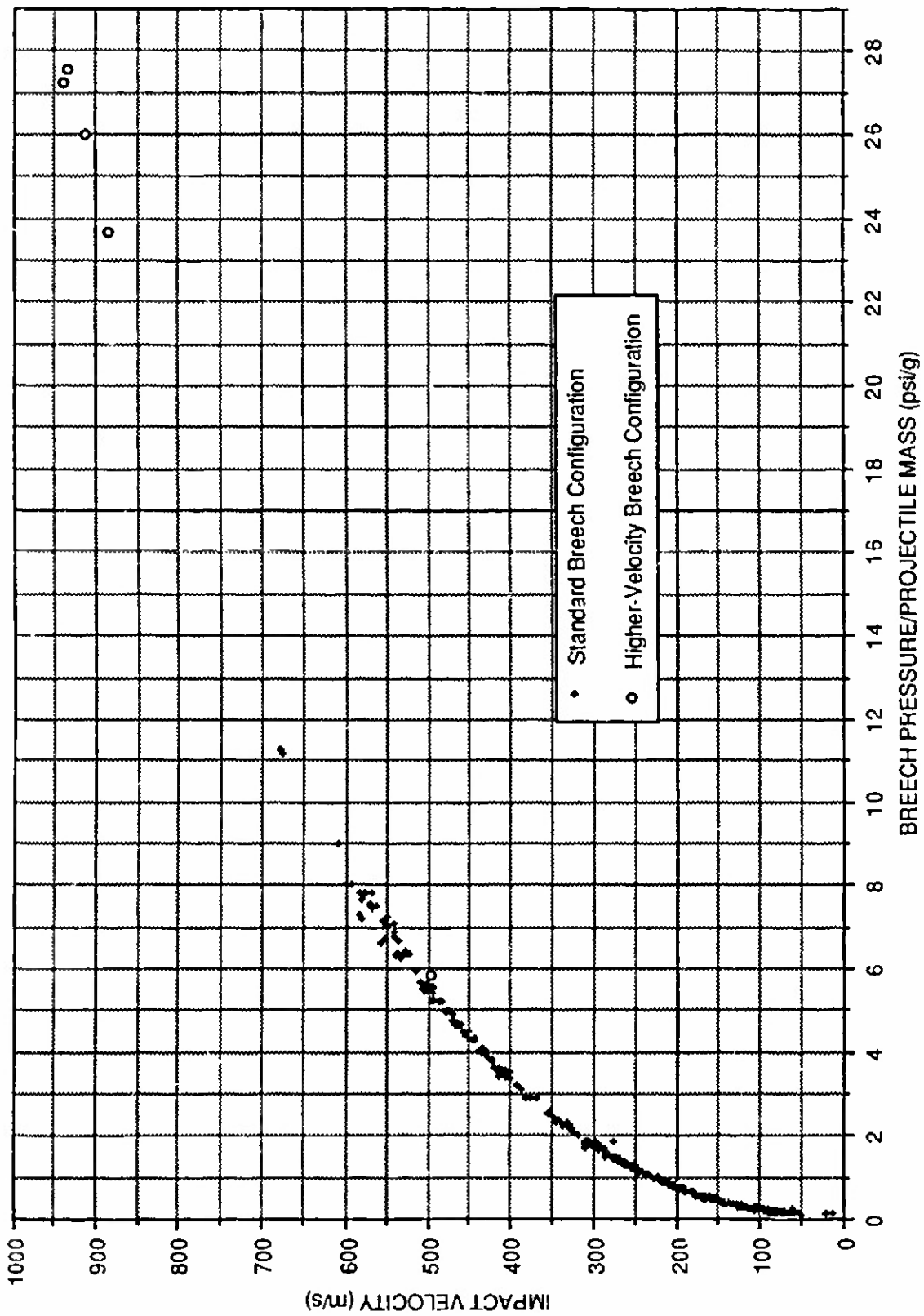
Figure 6. 2.5-in. gas gun data: both breech configurations (1977-1990).

CAM-318543-6

12

4-IN. GAS GUN: NEW SYSTEM FOR IMPACT OF 12-IN.-DIAMETER PLATES

DESCRIPTION

SRI International's 4-in.-diameter light gas gun has been in operation for about 20 years. Its ≈14-m-long barrel is unslotted, so the gun is suitable for normal impacts only. The gun produces impacts with uniaxial strain pulse durations (before impingement of radial release waves from the target or projectile periphery) as high as 10-15 μs, depending on the target material, which is enough for most laboratory shock wave experiments.

The gun has three different breech configurations to span a wide range in impact velocity. A standard wraparound breech system (Figure 7a), similar to that described above for the 2.5-in. gun but with a maximum reservoir pressure of 3000 psi, has yielded a peak impact velocity of approximately 875 m/s with standard thick-walled aluminum projectiles. A double-diaphragm breech (Figure 7b) with a maximum reservoir pressure of 6000 psi has yielded a peak impact velocity of nearly 1.5 km/s using custom lightweight projectiles of nylon and foam.

A third configuration, dubbed the "Monkey's Fist" (Figure 8), is used for impact velocities below about 150 m/s. It uses the wraparound breech reservoir, but the projectile is held near the muzzle end of the barrel at a distance of only 1 – 5 ft from the target. Shortening the distance of projectile travel allows us to use a higher gas pressure to accelerate the same mass to the same velocity, thus reducing the great effect of frictional losses.

The Monkey's Fist is attached by a strong flexible steel cable to the breech plug. Its hardened steel fingers grip the back end of the projectile while gas fills the reservoir and the

13

Figure 7. 4-in. gas gun breech configurations.

14

High-Pressure Line to Projectile Release Mechanism

Fill Tube

Plug

Breech Nut

High-Pressure Reservoir

4"

Gun Barrel (~45' long)

Projectile

Steel Cable

"Monkey's Fist" Projectile Holding and Release Mechanism

Target

Target Tank

1'-5"
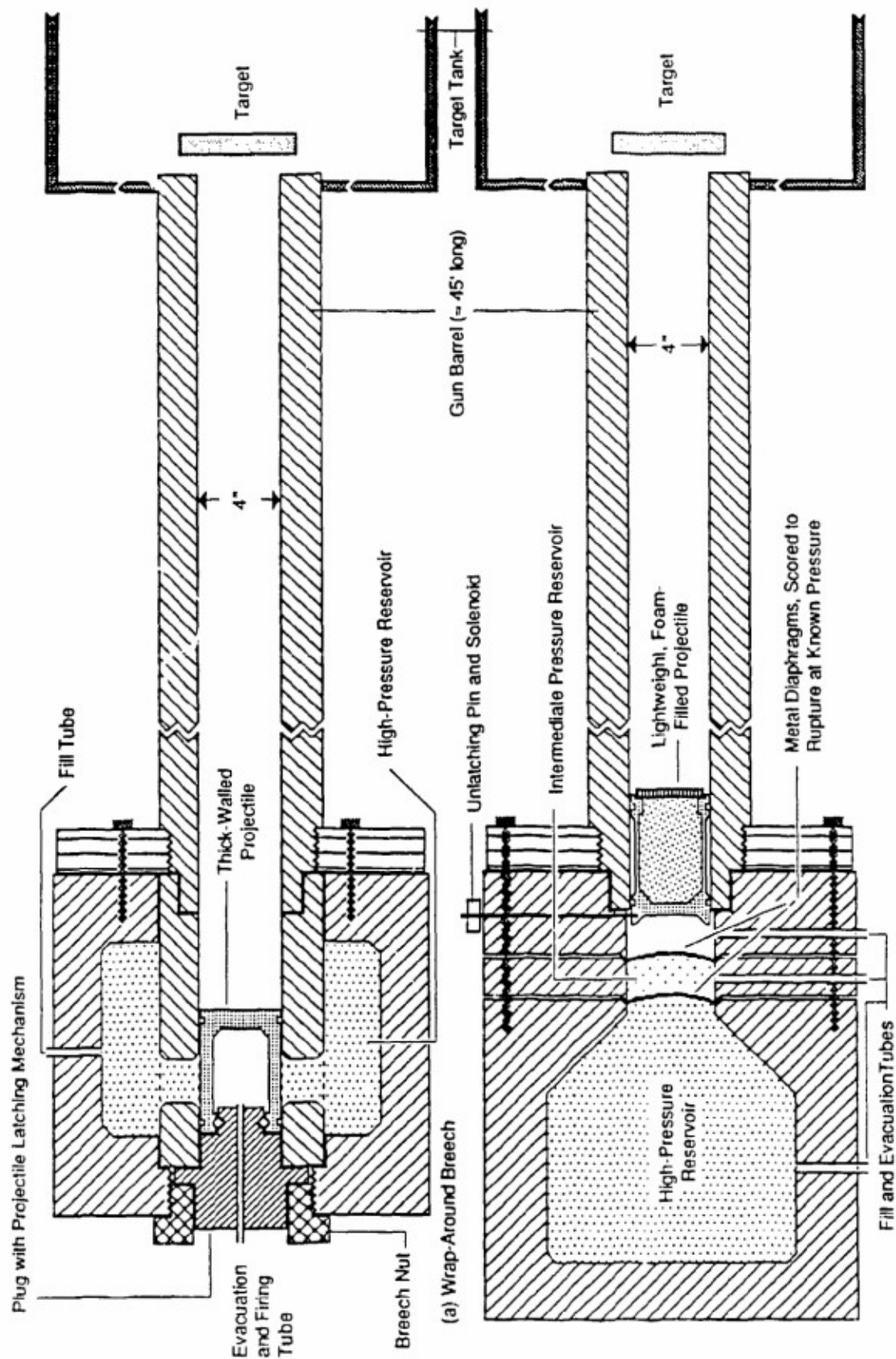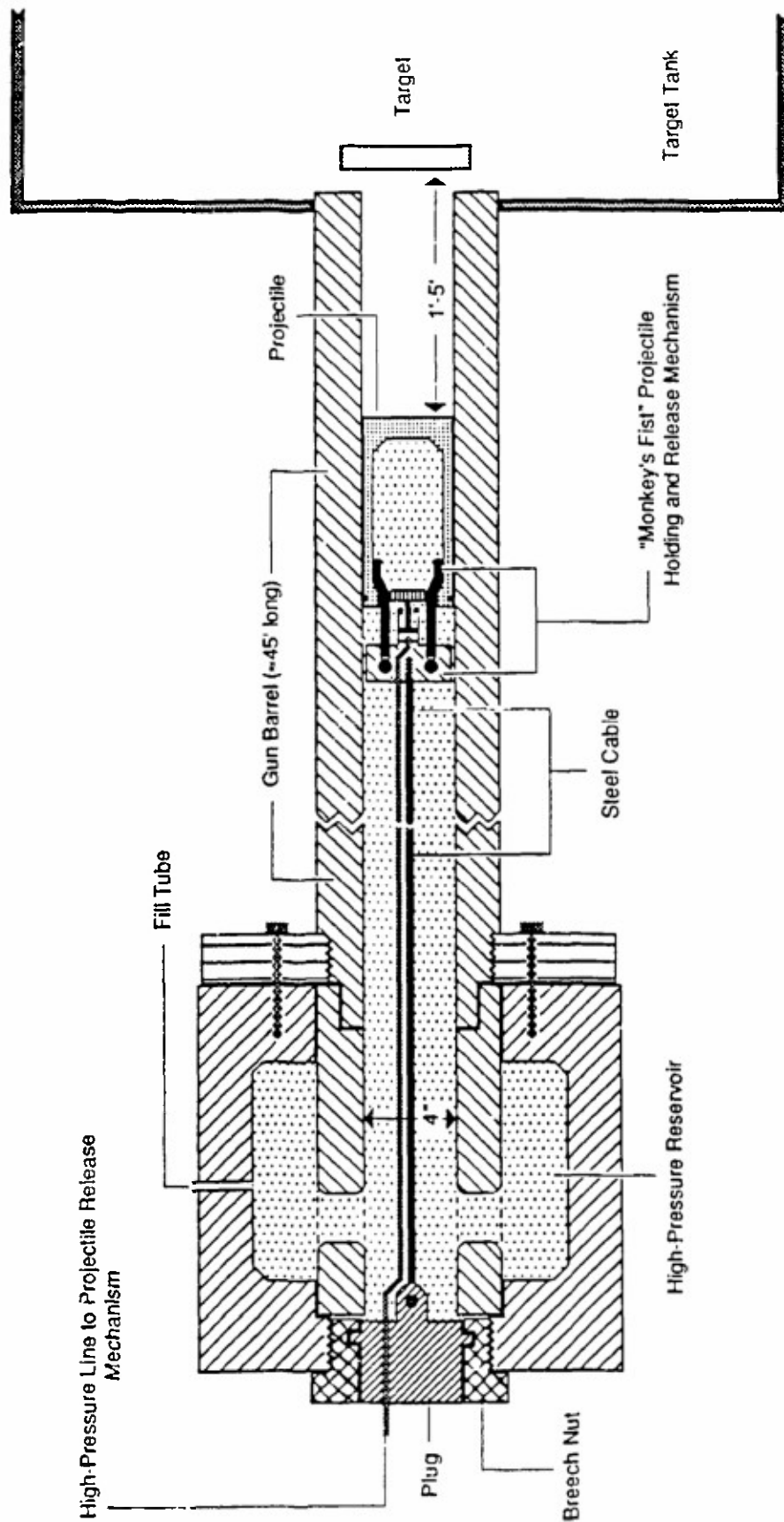
CAM-318543-8

Figure 8. 4-in. gas gun "Monkey's Fist" configuration for lower velocity impacts.

15

barrel region behind the projectile. A gas-driven piston is activated to launch the projectile, loosening the grip of the steel fingers. The Monkey's Fist system allows us to predict impact velocities as low as 50 m/s with less than 10% uncertainty and as low as 15 m/s with less than 20% uncertainty. In comparison, the wraparound breech system had velocity prediction uncertainties of 50% at 50 m/s and 75% at 15 m/s.

MOTIVATION FOR CHANGE

There has been significant interest over the last few years in stress gage validation for both *in situ* and underwater stress gage packages. These packages consist of one or more ytterbium or other stress transducers encapsulated within a metal jacket. A uniaxial strain pulse of 30–50 μs duration may be required to bring the gage and its jacket into stress equilibrium with the surrounding material. Because these gage packages are designed to operate in regions of relatively low stress, peak stress pulse magnitudes of interest for gage validation are from hundreds of bars to several kilobars.

Gage validation tests at SRI International have been performed using a 16-in.-diameter barrel H_2-O_2-gas-explosion gun located at the remote test facility. Although providing more than enough uniaxial strain pulse durations (flyer and target plates could be as large as 24 in. in diameter) for gage validation tests, the facility is relatively expensive to operate (the 16-in.-diameter by 24-in.-long projectiles are not reusable). Our goal therefore was to modify the 4-in.-gas gun to allow the planar impact of 12-in.-diameter plates. A 12-in.-diameter is enough to provide adequate uniaxial strain pulse durations for many applications. To minimize costs for both implementing these modifications and using the new configuration in testing, we planned to use as many of the existing 4-in. gas gun components as possible and to design the system so that the projectile could be reused.

LARGE DIAMETER PLATE IMPACT SCHEME

The new 4-in. gas gun configuration for impacting 12-in.-diameter plates is shown in Figures 9 and 10. The projectile consists of an 18-in.-long shaft that fits into the muzzle end of the barrel, a 12-in.-diameter by 1-in.-thick aluminum pusher plate bolted to the shaft, and a 12-in.-diameter flyer plate. Both the pusher and flyer plate are positioned in the target tank, with the impact end of the flyer plate located 9 in. from the target face. The projectile shaft and pusher plate are reusable from shot to shot, while a new flyer plate is bolted or glued onto the pusher plate.

The target, whose diameter is slightly larger than that of the flyer plate, is attached to a target holding and alignment fixture bolted to the floor. Velocity and tilt pin blocks may be attached to the front of the target.

The Monkey's Fist is used to hold and release the projectile in the same manner as described above for lower velocity tests. Because the projectile assembly is much heavier (as high as ≈ 20 kg) and the distance to impact shorter than in the usual Monkey's Fist arrangement, higher gas pressures are required to attain the same impact velocity in the new configuration. So the steel cable between the Monkey's Fist and the breech plug was replaced by a series of 10-ft-long by 1-in.-diameter high-strength steel rods, joined together by connectors and pretensioned to remove the slack before pressurization. The system was designed to operate up to a pressure of 1500 psi (the original Monkey's Fist system operated up to about 500 psi).

The projectile must be prevented from completely exiting the barrel after impact to ensure that the projectile shaft and pusher plate are undamaged after each shot. For this purpose, several aluminum honeycomb disks, approximately 11 in. in diameter and 3 in. thick, are positioned behind the target (far enough away to avoid affecting the wave
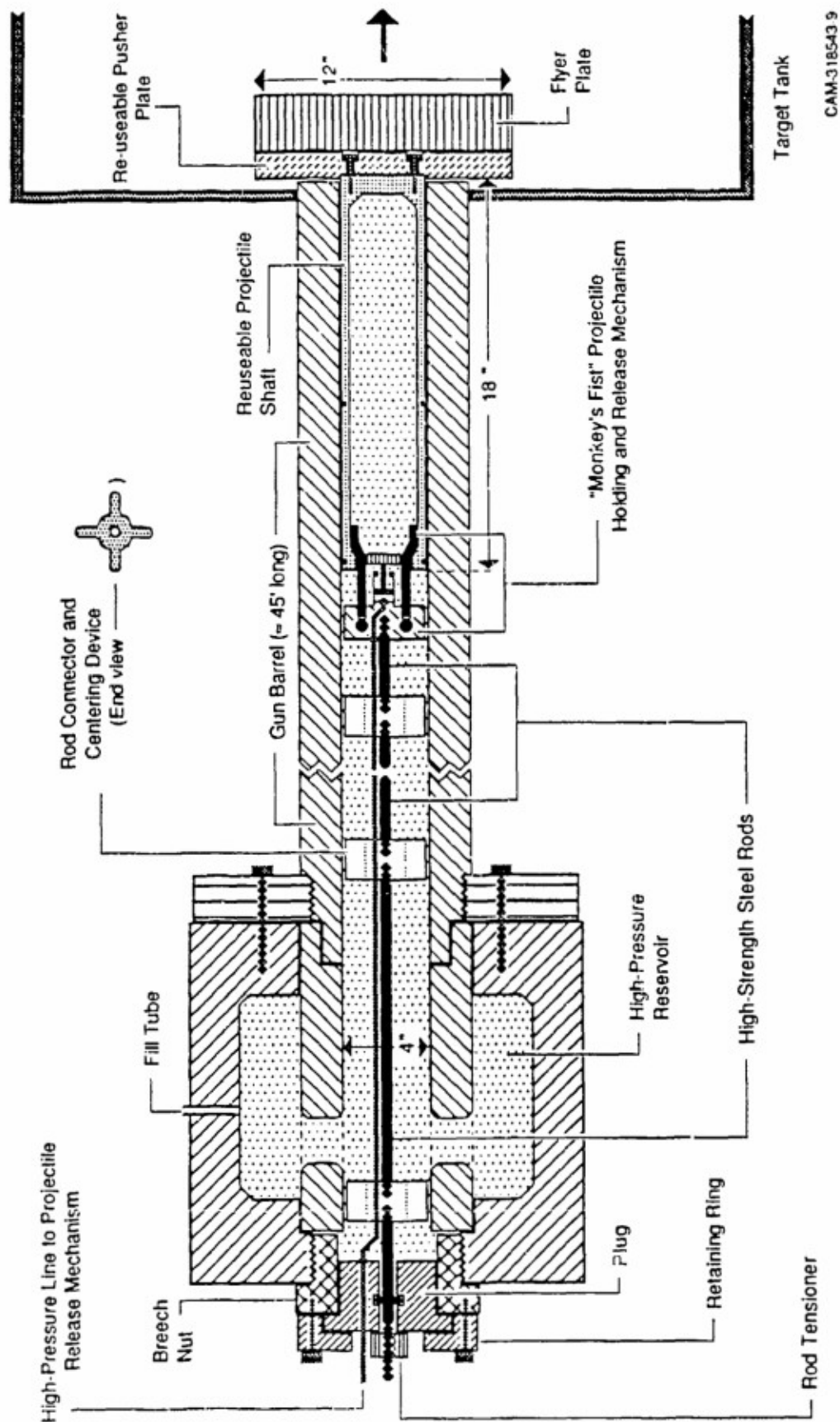
Figure 9. 4-in. gas gun configuration for planar impact of 12-in.-diameter plates: breech section.

Re-useable Pusher Plate

Flyer Plate

Target Tank

CAM-318543 9

12"

Reuseable Projectile Shaft

18"

"Monkey's Fist" Projectile Holding and Release Mechanism

Rod Connector and Centering Device (End view)

Gun Barrel (≈ 45' long)

High-Pressure Line to Projectile Release Mechanism

Fill Tube

High-Pressure Reservoir

High-Strength Steel Rods

4"

Breech Nut

Plug

Retaining Ring

Rod Tensioner

18
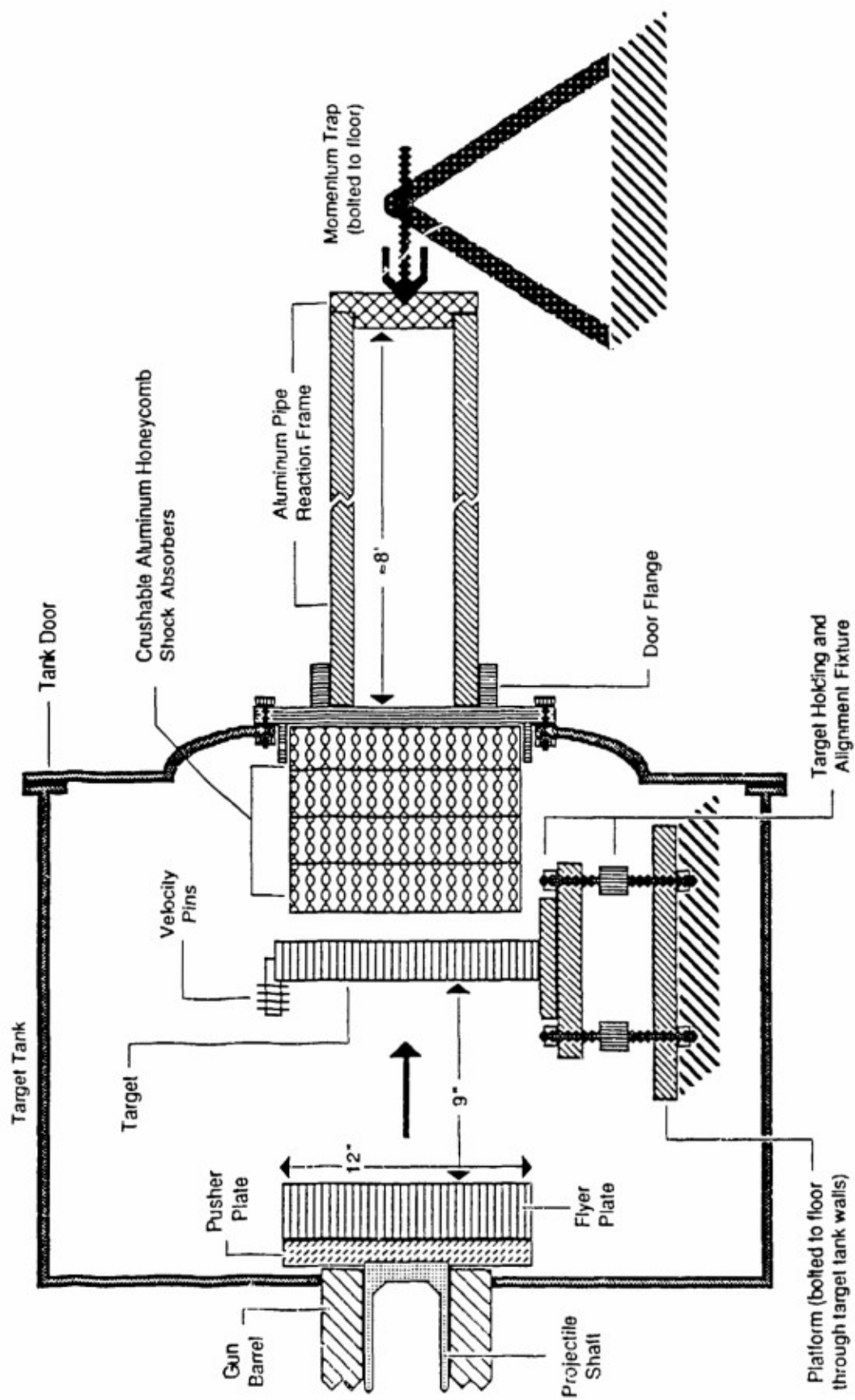
Figure 10. 4-in. gas gun configuration for planar impact of 12-in.-diameter plates: target section.

CAM-318543-110

19

propagation in the target during times of interest) to act as shock absorbers. The first layer or two of the honeycomb crushes on impact and stops the projectile/target mass after it has traveled several inches, leaving a substantial length of the projectile shaft within the barrel.

Honeycomb layers are available in several different strengths, depending on the mass of the projectile and the intended impact velocity. The honeycomb shock absorbers are attached to a flange on the target tank door, and the momentum from the stopped impact is transmitted through a massive reaction frame to a momentum trap bolted to a concrete pad in the floor.

Thus far, seven tests have been performed using the new 12-in.-diameter plate impact system. Impact velocities have spanned a range from 13 to 42 m/s, as shown in Figure 11. The impact tilt has been ..bout 0.5 mRad. The tests so far have involved gage package validations in both dry and saturated limestone. Future tests may call for the use of large Helmholtz-type coils on both sides of the target to create a uniform magnetic field and allow the use of particle velocity gages.
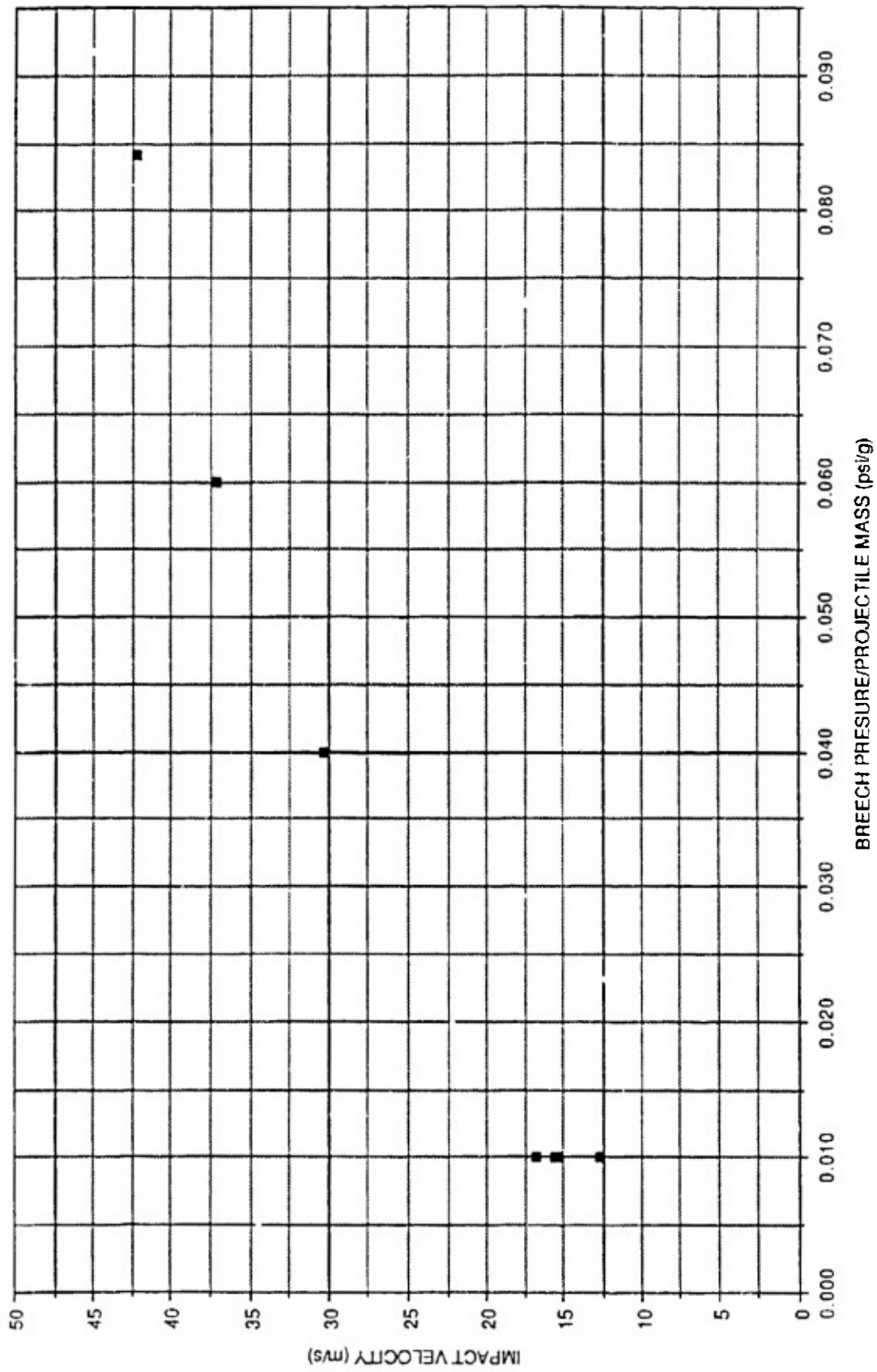
Figure 11. 4-in. gas gun: 1-ft-diameter impact data (1990).

CAM-318543-11

**THE STRENGTH BEHAVIOR OF GRANULATED SILICON CARBIDE
AT HIGH STRAIN RATES AND CONFINING PRESSURE**

The strength behavior of granulated silicon carbide at high strain rates and confining pressure

R. W. Klopp and D. A. Shockey
SRI International, 333 Ravenswood Avenue, Menlo Park, California 94025-3493

The dynamic Mohr–Coulomb behavior of silicon carbide (SiC) was inferred from symmetric pressure/shear plate-impact experiments which entail planar impact of two SiC plates inclined at 15° to the impact direction. The transverse velocity of the free rear surface of the target plate was recorded using a laser Doppler velocimeter system, and the experiments were simulated using a postulated viscoplastic constitutive model that accounts for comminution and dilatancy. Model parameters were varied until the computed and measured velocity histories agreed. The results indicate that comminution occurred soon after loading, and thus the experiment measures the behavior of granulated material at shear strain rates of $\approx 10^5$ s^{-1} and mean stress ranging from 1 to 9 GPa. A friction coefficient of 0.23 was obtained, which is about half the value for quasistatic compression of precomminuted ceramic reported in the literature. The simulation results were strongly affected by the values chosen for the friction coefficient and yield strength parameters; changes in the dilatancy, rate-sensitivity, and strain-hardening parameters had a lesser effect.

INTRODUCTION

Examination of confined ceramic targets that have been impacted by long tungsten rods suggests that the comminution and granular flow behavior of the ceramic governs the resistance to penetration.[1] A penetrator can advance in a ceramic target that is confined on all sides by steel plates only if ceramic material at the leading penetrator surface is moved out of the penetrator path. Fractographic observations of targets sectioned after ballistic testing indicate that this occurs by the crushing of a small quantity of the ceramic within about two penetrator radii ahead of the advancing penetrator and the subsequent flow of the comminuted material lateral to and then opposite the direction of attack. Thus the shear strength of comminuted as well as intact material contributes to penetration resistance. Hydrocode simulations show that the mean stress in this zone, which we shall call the Mescall zone after John Mescall who first deduced its existence,[2,3] is on the order of the confined compressive strength of the ceramic. For silicon carbide the confined compressive strength, i.e., the Hugoniot elastic limit (HEL), is around 13 GPa.[4,5] Simulations also indicate that equivalent shear strain rates in the zone are on the order of 10^4–10^5 s^{-1}. Thus the penetrability of armor ceramics is controlled by their resistance to comminution and fragment flow at high loading rates and at high compressive mean stress levels.

Computational simulations can make armor material and package design more efficient by eliminating trial-and-error ballistic testing. These simulations require material models that reflect the micromechanisms of deformation and failure and experimental measurements of properties controlling these mechanisms. However, relatively few techniques are available, particularly for ceramics, to make measurements of comminution and granular flow properties under penetration conditions. The objective of this work was to perform pressure/shear plate-impact experiments on an armor ceramic to measure the comminution and flow properties under conditions of confining pressure and strain rate representative of those at the tip of an advancing penetrator.

Up to now, the properties of armor ceramics have been measured using quasistatic and dynamic compression of small cylinders, with or without confining stress, or using uniaxial strain impact of plates. Heard and Cline[6] investigated the quasistatic mechanical behavior of BeO, Al$_2$O$_3$, and AlN cylinders in axial compression with a radial confining pressure and constructed stress-strain curves and stress-difference versus confining-stress curves. Lankford[7] and Johnson et al.[5] performed similar tests on armor ceramics, but used a Hopkinson bar apparatus to achieve strain rates near 10^3 s^{-1}. However, neither of the cylinder compression techniques can reach the mean-stress levels thought to exist ahead of an advancing penetrator. The radial confining stress is always well below the axial failure stress, and thus the mean stress is dominated by the axial stress. Posttest examination of the specimens showed failure occurred by faulting, which on a macroscopic level is a different failure mechanism than comminution and flow of fragments.[8] In the Hopkinson bar tests, reported strengths are for the onset of failure, i.e., plastic strains are negligible.

Johnson et al.[5] performed quasistatic compression tests on comminuted SiC that was prepared by ball milling. The data are reported in terms of Von Mises equivalent compressive stress σ_Y as a function of mean stress p, and when converted to equivalent shear stress $\tau_Y = \sigma_Y/\sqrt{3}$, as a function of mean stress and fitted with a straight line, a friction coefficient of 0.46 is indicated.

Brar and Bless[9] reported a bar-impact test for measuring the high-strain-rate compressive strength of ceramics and glass. Two slender, constant-diameter bars were impacted axially at a relative velocity of 100–300 m/s, and

the impact was photographed using a high-speed framing camera. The photographs indicated the velocity of deformation and fracture waves traveling along the target bar. A piezoresistant stress gauge sandwiched in the target bar several diameters from the impact end provided a measure of the dynamic compressive strength. Unfortunately, mean stresses and strain rates in these tests are not accurately known, and so the results are difficult to interpret.

Gust, Holt, and Royce,[10] Kipp and Grady,[4] and Johnson et al.[5] performed uniaxial-strain shock compression and release experiments on several ceramics, in which they recorded free surface or window interface particle velocities. Kipp and Grady constructed constitutive models by iteratively varying a proposed stress-strain path until computer simulations using the path reproduced the measured velocities. Kipp and Grady were able to simulate their measurements on SiC by using an elastic-plastic model adapted from metals. However, because theirs were uniaxial strain experiments, plastic strains were small, being on the order of 1%, and because velocities were high, mean stresses were higher than those in the zone ahead of a penetrator, which are on the order of 30 GPa.

Klopp and Shockey[11] reported shear stress-strain curves for aluminum nitride (AlN) at a mean stress of 11 GPa and a shear rate of 1.3×10^5 s^{-1} for shear strains to 8%. These values were obtained using the high-strain-rate pressure/shear plate-impact technique,[12] in which an inclined flyer plate carrying a thin layer of specimen material impacts a similarly inclined anvil plate such that the specimen is compressed and sheared between the plates. Before waves arrive at the middle of the plates from the peripheries, and if the flyer and anvil plates remain elastic while the specimen yields and flows, an analysis very similar to that for the Hopkinson bar applies, and a stress-strain curve can be directly obtained for conditions like those at the tip of a penetrator. Unfortunately, this "sandwich" test cannot be used for the strongest ceramics, since no materials that will remain elastic (except perhaps diamond) are available for the flyer and anvil plates.

To enable evaluation of very strong ceramics, the high-strain-rate pressure/shear plate-impact experiment must be modified. By impacting one plate of the specimen material directly with a second plate, i.e., a symmetric pressure/shear experiment (Fig. 1), both longitudinal and shear waves are produced in the plates, and material behavior can be inferred from velocity-time profiles recorded in the interior of the anvil or at its rear surface. The transverse velocity profile due to shear waves is especially indicative of the resistance of a material to deformation at high mean-stress levels and loading rates. Conditions such as those at the tip of a penetrator can be produced. A drawback of the symmetric pressure/shear experiment is that computer simulations are required to infer material properties from the recorded velocity histories for all but the very simplest constitutive behaviors.[13]

This paper describes two symmetric pressure/shear plate-impact experiments on SiC ceramic. We first describe the experimental procedure and the results. The interpretation of the results by numerical simulations is then pre-
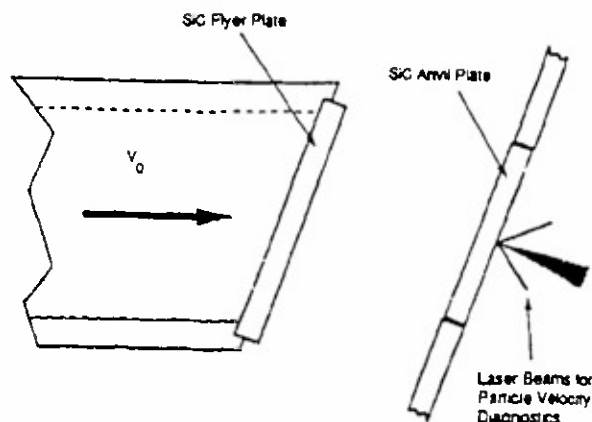

FIG. 1. The symmetric pressure/shear experiment.

sented and a material model is proposed. Finally, the results and model are discussed in relation to data obtained by other researchers.

PRESSURE/SHEAR EXPERIMENTS

Two experiments were performed using plates prepared from a single tile of sintered α-SiC supplied by Carborundum. The density of the SiC was 3.2 g/cm^3 and the grain size approximately 3 μm. Both flyer and anvil plates were disks nominally 55.4 mm in diameter, and the flyers were 5.3 mm thick. The anvil plates for experiments 1 and 2 were 5.06 and 2.51 mm thick, respectively. The impact and rear faces of the anvils were initially lapped to a flatness of 2.5 μm, with a roughness of about 20 nm root mean square (rms). Then the rear face of the anvils was further polished to a roughness of about 6 nm rms to improve reflectivity.

The flyers were mounted at an angle of 15° on the leading end of a 6-in.-long aluminum projectile and launched from SRI's 2.5-in.-bore slotted gas gun at 0.913 and 0.715 mm/μs. A key on the projectile engages the slot to prevent rotation and loss of parallelism. Before launch, the anvil plates were inclined at an angle of 15° and aligned to be parallel with the flyers within 0.2 mrad. Four gold contacts that had been vapor-deposited onto the periphery of the plates indicated parallelism and triggered recording instruments. The impact velocity was measured using spaced shorting pins located at the gun's muzzle. Impact occurred in an evacuated tank to reduce the lubricating effect of gas trapped between the flyer and anvil.

In previous pressure/shear experiments performed on metals, the transverse motion of the anvil rear surface has been measured using either a transverse displacement interferometer[14] (TDI) or two VISARs.[15] The TDI requires a diffraction grating on the anvil rear surface, but because of the fragility of polymer diffraction gratings and the difficulty of etching gratings directly into the ceramic, the TDI could not be used for these experiments. Although the VISAR technique could probably be used, we chose instead to adapt a laser Doppler velocimeter (LDV) system, commonly used in fluid-mechanics experiments, to
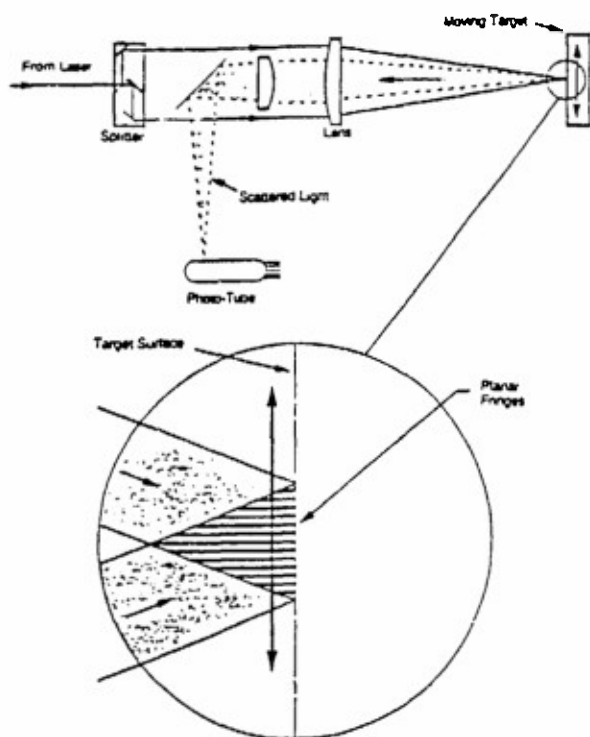
FIG. 2. The laser Doppler velocimeter (LDV) system.

	Experiment 1	Experiment 2
Impact velocity (mm/μs)	0.913	0.715
Skew angle (deg)	15	15
Tilt (mrad)	36	0.6
Anvil thickness (mm)	5.06	2.51

the rear surface of the target (which had a 6-nm-rms finish) had enough scratches and pits to scatter light and provide measurable signals.

The electrical signal from the PMT was amplified and split so that half could be recorded directly and the other half processed with a 10-MHz high-pass filter to remove meaningless large, lower-frequency excursions. Signals were recorded on 250-MHz-bandwidth analog oscilloscopes. The transverse velocity was determined by measuring the times of the peaks and valleys of the sinusoidal signal. We divided the displacement between consecutive peaks (7.9 μm) by the time between those peaks to determine the velocity history.

Parameters of the two experiments are given in Table I, and the oscilloscope traces and transverse velocity histories are shown in Fig. 3. Where the sinusoid is clear and has relatively constant frequency, such as in experiment 2, the velocity is known to within $\pm 5\%$. Where it is not clear—such as near wave arrival and near times when scattering objects enter or leave the measurement volume—the uncertainty is greater. For example, the uncertainty is nearly 100% between 0.80 and 0.90 μs in Fig. 3(a) (experiment 1), where the LDV sinusoid contains a segment of high-frequency, low-amplitude noise, presumably caused by the absence of light scatterers in the measurement volume. Similarly, the uncertainty is at least 50% at 1.03 μs, where the phase of the LDV signal suddenly jumps, presumably as a result of scatterers entering or leaving the measurement volume. We believe that in experiment 1 the transverse velocity was around 0.17 $\pm$ 0.03 mm/μs and probably steady between 0.4 and 1.2 μs.

ANALYSIS

We used an iterative computational procedure to deduce the stresses and strains within the anvil plates from the measured rear-surface transverse velocities. In this procedure we propose a material model with associated parameters and simulate the experiments with it. If the calculated transverse particle velocity histories match those measured in the experiments, then we suggest that the model is appropriate—at least for the conditions in the experiments—and correctly infers the histories of stress and strain within the anvils. This iterative procedure has been often applied. Examples include the Taylor test, in which a constitutive model is varied until the computed deformed rod profiles match those observed;[16] shock-compression and release experiments, in which a loading path is varied until computed and experimental particle velocities agree;[4] and previous symmetric pressure/shear experiments on metals.[17]

these shock-physics experiments (Fig. 2). In this system two parallel laser beams pass through an objective lens that focuses them and causes them to intersect and form an ellipsoidal measurement volume. Within the measurement volume, the two intersecting beams interfere and form a pattern of equispaced bright and dark planar fringes. As a light-scattering object moves transversely through the measurement volume, the scattering intensity is modulated by the fringes. When the object moves at a constant velocity, the scattered light intensity history is sinusoidal. Since the fringe spacing is fixed by the laser wavelength and beam intersection angle, the modulation frequency gives the speed of the scattering object. The fringes in the measurement volume are parallel to a plane that contains the bisector of the beam intersection angle and is perpendicular to the plane of the intersecting beams. Thus, if the bisector is made to be perpendicular to the surface of a solid target, the modulation frequency will be insensitive to the normal motion of the target. Another attractive feature of the system is that the results are independent of the condition of the anvil rear surface, provided that this surface scatters light toward the detector and the reflectivity changes relatively slowly so as not to be confused with intensity changes due to motion through the fringes.

In our system the 514.4-nm argon-laser beams were spaced 52 mm apart before entering the objective. The objective had a focal length of 800 mm, giving a fringe spacing of 7.9 μm. The measurement volume was about 150 μm in diameter. The scattered light was collected through the center of the objective lens and converted to an electrical signal with a photomultiplier tube (PMT). We found that
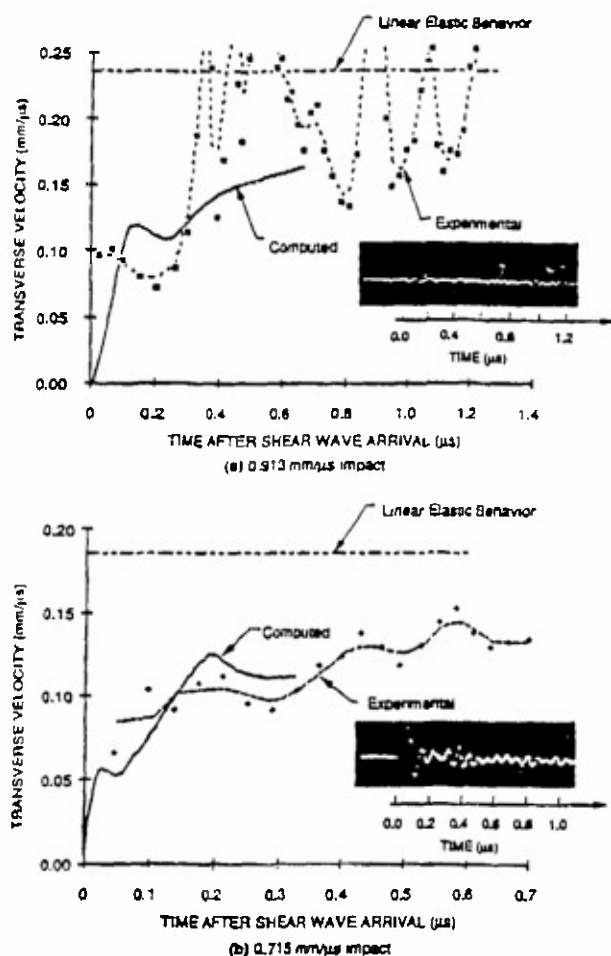
FIG. 3. LDV oscilloscope records and measured and computed transverse velocity histories.

For this project we simulated the pressure/shear experiments following the analysis of Abou-Sayed and Clifton for aluminum.[17] However, we expanded their analysis to include dilatancy, comminution, and mean-stress-dependent yielding, because these phenomena are thought to be important in the flow of ceramics. We consider the specimen as an infinite plate normal to the x axis, with $x = 0$ being the impact face, and the y axis extending in the direction of the imposed transverse velocity. Considering symmetry and that the motion is independent of the y and z coordinates, there is no motion in the z direction (z-direction velocity $w = 0$), and the shear stresses σ_{xz} and σ_{yz} must be zero. Furthermore, if the dilatancy is isotropic, then we can show that the in-plane normal stresses are equal ($\sigma_{yy} = \sigma_{zz}$). Thus there are five unknowns: the normal velocity u, the y transverse velocity v, the normal stresses σ_{xx} and σ_{yy}, and the shear stress σ_{xy}. The governing equations include the momentum equation, the compatibility equation, and a constitutive relation. These equations can be combined to yield the five necessary to find the unknowns.

We use the constitutive framework developed by Perzyna,[18] in which the total strain rate is additively decomposed into elastic and plastic parts and the plastic part is determined by the overstress (the difference between the applied equivalent stress and the current yield equivalent stress). The resulting constitutive equation has the form

$$\dot{\varepsilon}_{ij} = \frac{1+\nu}{E}\dot{\sigma}_{ij} - \frac{\nu}{E}\delta_{ij}\dot{\sigma}_{kk} + \langle\phi(\bar{\tau},\bar{\gamma}^p,p,D)\rangle\frac{\partial f}{\partial\sigma_{ij}}, \quad (1)$$

where $\dot{\varepsilon}_{ij}$ is the total strain rate, ν is Poisson's ratio, E is Young's modulus, δ_{ij} is the Kronecker delta, $p = -\sigma_{kk}/3$ is the negative of the mean stress or hydrostatic pressure, ϕ is the equivalent plastic strain rate, $\bar{\tau}$ is the effective shear stress, $\bar{\gamma}^p$ is the equivalent plastic shear strain, D is the amount of comminution, and f is a flow potential. The effective stress is given in the usual way in terms of the deviatoric stress, $S_{ij} = \sigma_{ij} - \delta_{ij}\sigma_{kk}/3$:

$$\bar{\tau} = (\tfrac{1}{2}S_{ij}S_{ij})^{1/2}, \quad (2)$$

and the equivalent plastic shear strain is defined as

$$\bar{\gamma}^p = \int_0^t \langle\phi\rangle dt. \quad (3)$$

The bracket function $\langle\phi\rangle$ is defined such that

$$\langle\phi\rangle = \begin{cases} 0, & \text{for } \phi<0, \\ \phi, & \text{for } \phi>0. \end{cases} \quad (4)$$

The first two terms on the right-hand side of the constitutive equation (1) determine the elastic part of the strain rate and the third term gives the plastic strain rate.

Following Rudnicki and Rice,[19] we define our flow potential to be

$$f = (\tfrac{1}{2}S_{ij}S_{ij})^{1/2} + \frac{\beta}{3}\sigma_{kk} \quad (5)$$

where β is the so-called dilatancy, which is defined as the increment in volumetric strain resulting from a unit increment of plastic shear strain.

The experimental results of Heard and Cline[6] and Lankford[7] for AlN and Al_2O_3 and of Johnson et al.[5] for SiC show rather weak elevation of the overstress with increasing strain rate. Thus we choose the overstress to be proportional to the logarithm of the plastic strain rate, such that

$$\phi = \frac{\dot{\gamma}_0}{\sqrt{3}}\exp\left[\left(\frac{\bar{\tau}-\tau_y}{\tau_0}\right)^{1/m}\right], \quad (6)$$

where τ_y is the equivalent shear yield stress and $\dot{\gamma}_0$, τ_0, and m are constants.

We choose the equivalent shear yield stress to depend on the mean stress, amount of comminution, and strain hardening:

$$\tau_y = F(p,D)\tau_{y0} + \frac{h}{3}\bar{\gamma}^p, \quad (7)$$

where F is the mean stress-damage function, h is the tangent modulus of a uniaxial stress-strain curve, and τ_{y0} is the initial shear yield stress at atmospheric pressure. As the material changes from an intact to a fully comminuted

7321   J. Appl. Phys., Vol. 70, No. 12, 15 December 1991

R. W. Klopp and D. A. Shockey   7321

state, D goes from zero to one and F simultaneously changes from a form appropriate to undamaged material (F_U) to a form appropriate to comminuted material (F_D):

$$F = (1 - D)F_U + DF_D. \tag{8}$$

The function F_U is chosen so that the yield stress smoothly increases with mean stress up through the HEL point:

$$F_U = \begin{cases} 1, & \text{for } p < p_0, \\ \dfrac{\tau_{HEL} - \tau_{y0}}{\tau_{y0}(1 - e^{-1})} \left[1 - \exp\left[-\left(\dfrac{p - p_0}{p_{HEL} - p_0} \right) \right] \right] + 1, \\ & \text{for } p > p_0, \end{cases} \tag{9}$$

where τ_{HEL} and p_{HEL} are the shear yield stress and mean stress, respectively, at the Hugoniot elastic limit and p_0 is a constant.

The function F_D is chosen so that, below a limiting mean stress, yield stress varies linearly with mean stress according to Mohr–Coulomb behavior. Above the limiting mean stress, the yield stress is assumed to be constant. The limiting mean stress is chosen such that the shear strength cannot exceed the theoretical strength (chosen to be $G/20$, where G is the shear modulus):

$$F_D = \begin{cases} \dfrac{p\mu}{\tau_{y0}}, & \text{for } p < p_{max}, \\ \dfrac{G}{20\tau_{y0}}, & \text{for } p > p_{max}, \end{cases} \tag{10}$$

where μ is the Mohr–Coulomb friction coefficient and $p_{max} = G/20\mu$.

The amount of comminution, D, is initially zero and increases toward one if the square root of the second invariant of the *total* stress $I_2 = \sqrt{\sigma_{ij}\sigma_{ij}/2}$ exceeds some constant limit I_{lim}. The rate of increase of D is proportional to the amount by which I_2 exceeds I_{lim}. Thus

$$\dot{D} = \frac{(I_2 - I_{lim})}{\rho c_1 t_0}(1 - D), \tag{11}$$

where ρ is the density, c_1 is the longitudinal-wave speed, and t_0 is a time constant. The choice of I_2 as the driving force for comminution is based on the notion that even purely hydrostatic loadings comminute ceramic. Hydrostatic loading causes comminution because neighboring grains often have different crystallographic orientations and thus have different strain fields as a result of anisotropy. Cracks form when stresses necessary to enforce compatibility of these strain fields across grain boundaries exceed some failure stress.

Constitutive equations (1)–(11) are combined and, together with the momentum and compatibility equations, are rewritten as equations along characteristics. We solved the equations using a modification of the method of Ranganath and Clifton[20] The boundary conditions for the anvil plates are that the rear surface is traction free and the impact face has an imposed velocity of one-half the impact velocity.

RESULTS

The solid lines in Figs. 3(a) and 3(b) are the free-surface transverse velocity histories for the two experiments, computed using the parameters in Table II. The computed histories follow the measured histories reasonably well. Figure 4 shows the mean stress p as a function of position through the anvil (as a percentage of the anvil thickness) at various times. Similar plots for equivalent plastic strain rate $\dot{\gamma}$, equivalent plastic strain $\bar{\gamma}^p$, and comminution D are shown in Figs. 5–7. The travel of the longitudinal waves through the anvil to the rear surface and back is readily apparent. At 0.913 mm/μs, a large portion of the specimen sees a mean stress of about 9.2 GPa before dropping to roughly half that level. At 0.715 mm/μs, the mean-stress wave front is less sharp, rising to a peak level of about 7 GPa before dropping by half. Less of the specimen reaches the peak mean-stress levels in the 0.715-mm/μs simulation. From Fig. 5 it is clear that plastic shear strain rates of the order of 3×10^5 s^{-1} are achieved, although these rates are sustained for only a short duration at any given location. Figure 6 shows that the cumulative effect of those strain rates are plastic shear strains of 3.3% and 2.6%, respectively, at the impact faces, and 6.5% and 4.5% peak levels, respectively, for 0.913- and 0.715-mm/μs impacts. Figure 7 shows that the comminution level D rapidly approaches 1 in the interiors of the anvils for both impacts, and comparison with Fig. 5 shows that this occurs before the peak in strain rate. Thus the majority of the deformation takes place in highly comminuted material.

DISCUSSION

The results of experiment 2 (0.715 mm/μs) are relatively unambiguous. The transverse velocity time record [Fig. 3(b)] looks similar to those reported previously for rocks and metals, although the initial plateau followed by a later rise is more reminiscent of the double-wave structure seen in longitudinal waves. This double-wave structure

TABLE II. Simulation parameters.

Density (kg/m^3)	ρ	3.20[a]
Longitudinal-wave speed (mm/μs)	c_1	11.1[a]
Shear-wave speed (mm/μs)	c_2	7.2[a]
Initial yield stress (GPa)	τ_{y0}	10.0
Friction coefficient	μ	0.23
Shear modulus (GPa)	G	164.0[a]
Poisson's ratio	ν	0.14[a]
Mean stress at HEL (GPa)	p_{HEL}	6.3[b]
Shear stress at HEL (GPa)	τ_{HEL}	6.4
Square root of second stress invariant at damage limit (GPa)	I_{lim}	3.1
Strain-rate constant (s^{-1})	γ_0	3.0
Shear stress constant (MPa)	τ_0	1.5
Strain-rate power	m	2.0
Pressure constant (GPa)	p_0	1.0
Time constant (ns)	t_0	1.0
Hardening modulus (GPa)	h	10.0

[a]Reference 21.
[b]Reference 4.

FIG. 4. Computed mean stress as a function of position within the anvil.

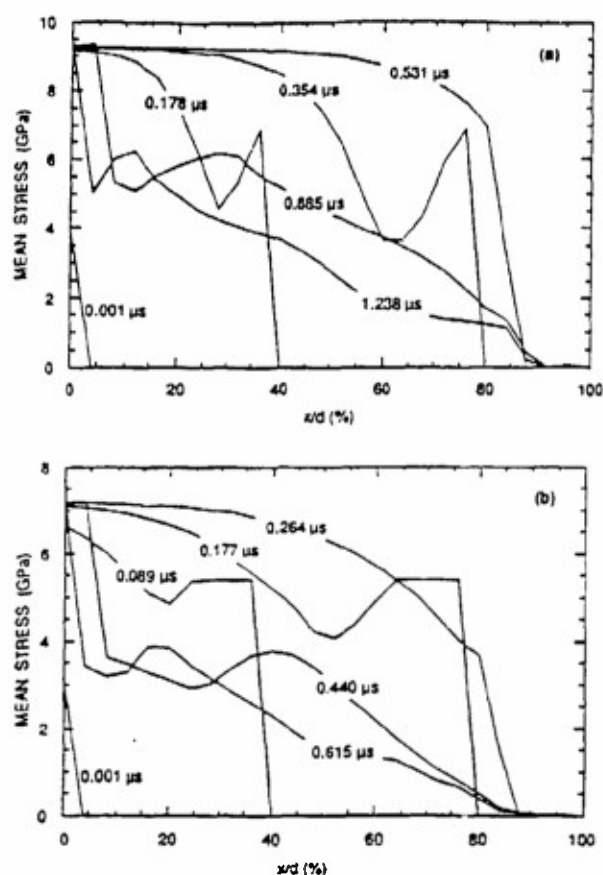FIG. 5. Computed equivalent plastic strain rate as a function of position within the anvil.

may result from strong coupling between the shear and longitudinal waves, which would provide evidence that the flow stress of comminuted SiC is controlled by the mean stress. We could investigate this issue further by performing experiments in which the anvil thickness varies widely. If true double waves are present, the lengths of the plateaus separating the waves will vary with the anvil thickness.

Because the transverse velocity record of experiment 2 has a plateau structure and the velocity is well below that expected if the SiC were elastic, we infer that the SiC yielded. If the SiC had remained elastic, the transverse velocity would have jumped to a level of 0.185 mm/μs upon shear-wave arrival. The normal stress would have been 12.0 GPa, the in-plane normal stress 1.95 GPa, and the shear stress 2.09 GPa. The equivalent normal stress would have been 10.4 GPa. This value is below the value at the reported HEL,[4,5] i.e., $\simeq$13 GPa. Thus we can conclude independently of the simulations that the SiC appears to have yielded at an equivalent stress near, but below, that of the HEL. We do not know if the SiC would yield at even lower stress levels. Rosenberg, Yeshurun, and Brandon[22] have reported evidence of plasticity in Coors AD-85 alumina loaded below the HEL. whereas Rosenberg, Brar, and Bless[23] found no evidence of plasticity in porous or nonporous B$_4$C loaded below the HEL.
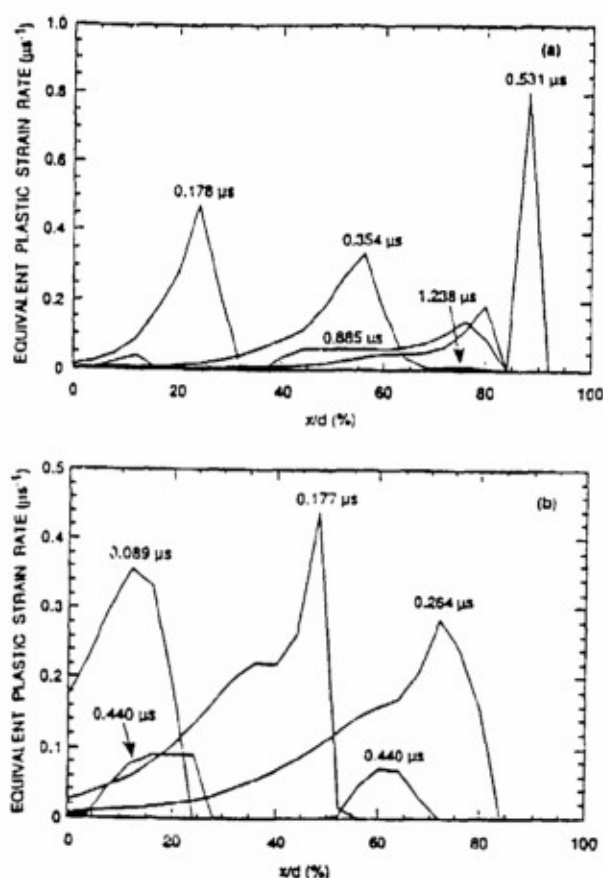
Plots of shear stress as a function of mean stress from

the simulations, that is, loading paths for material elements in the anvil, do not present a very clear picture of the response of SiC to high-strain-rate, high-mean-stress loading, because the plastic strain, strain rate, and comminution all vary simultaneously. A clearer picture emerges if we plot the response of the model when constant values for plastic strain, strain rate, and comminution are assumed. The response of the model at two extremes, (1) a strain rate of 10^3 s^{-1} and strain of 0 and (2) a strain rate of 10^5 s^{-1} and strain of 0.04, both for a comminution of 1.0, is shown in Fig. 8. Also included in this plot are the data of Johnson et al.[5] for intact and powdered material and that of Kipp and Grady for intact ceramic.[4] From this plot we conclude that the inferred response, i.e., the flow strength at a given pressure, is softer than even the response of powdered material at quasistatic loading rates.

In the simulations the response is only transiently affected by the properties of the intact ceramic, as can be seen by the steep front and high speed of the comminution wave as it traverses the anvil (Fig. 7). The effects of the intact ceramic are transient because the comminution time constant (t_0) is only 1.0 ns. The response is dominated by the friction coefficient ($\mu = 0.23$) and the combination of parameters that determine the overall flow stress ($\tau_0 = 1.5$ MPa, $\dot{\gamma}_0 = 3.0$ s^{-1}, and $m = 2$). Varying the dila-
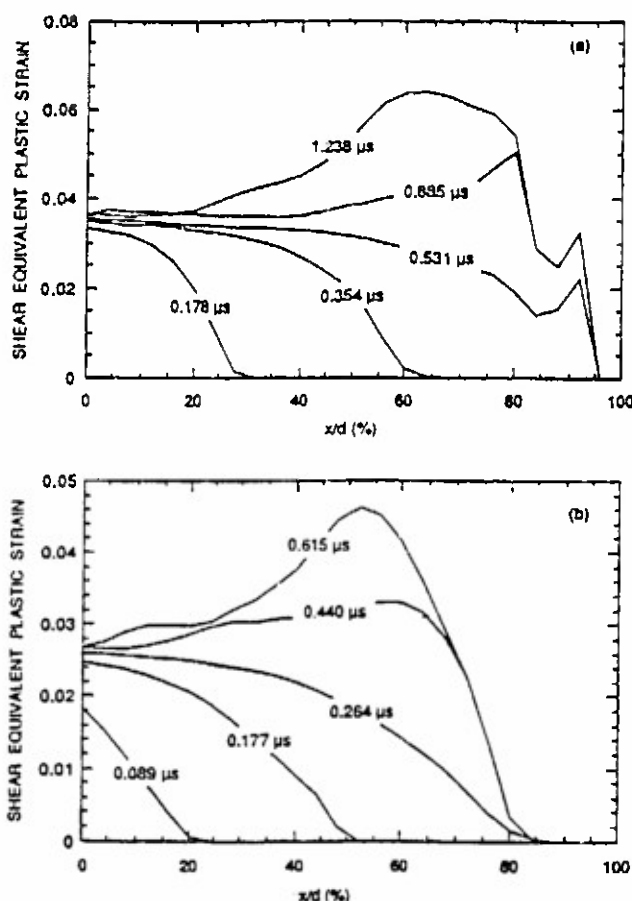
FIG. 6. Computed equivalent plastic shear strain as a function of position within the anvil.

FIG. 7. Computed comminution as a function of position within the anvil.

tan. $'$ (β), rate-sensitivity ($\dot{\gamma}_0, m$), and strain-hardening (h) parameters while keeping the friction coefficient and overall flow stress constant has a lesser effect on the results. A short relaxation time seems reasonable when one considers the high wave speeds and short crack propagation distances involved in comminution. The value $\mu = 0.23$ is below the range $0.4 < \mu < 0.9$ quoted by Rudnicki and Rice[19] for mineral-on-mineral sliding and is one-half the value obtained by Johnson et al.[5] on precomminuted SiC.

We suggest that the reason the flow strength at a given pressure is less than that measured in cylinder-compression and uniaxial strain plate-impact tests is that plastic strains in the latter tests are of the order of 1% or less, whereas plastic strains in our tests were 4.5%–6.5%. Such large differences in plastic strains imply large differences in the amount of fragment sliding that has occurred and the amount of concomitant interfragment debris that has been generated. Interfragment debris might tend to act as rollers between the fragments. Shear localization in the pressure/shear experiments might also account for the low inferred strength. Indeed, numerical overflow of the plastic strain rate occurred in the simulations when impact velocities much above 0.913 mm/μs were input.

The reason that the flow strength we inferred is less than that measured quasistatically on ball-milled SiC by

Johnson et al.[5] might be the differences in fragment sizes, shear localization, strain-rate effects, or the fact that our mean stresses were an order of magnitude higher. At high strain rates, fragment interfaces could melt if frictional heat builds up there. At high mean stresses, interfragment debris would form more readily than at low stresses.

FIG. 8. Equivalent flow stress as a function of mean stress for SiC.

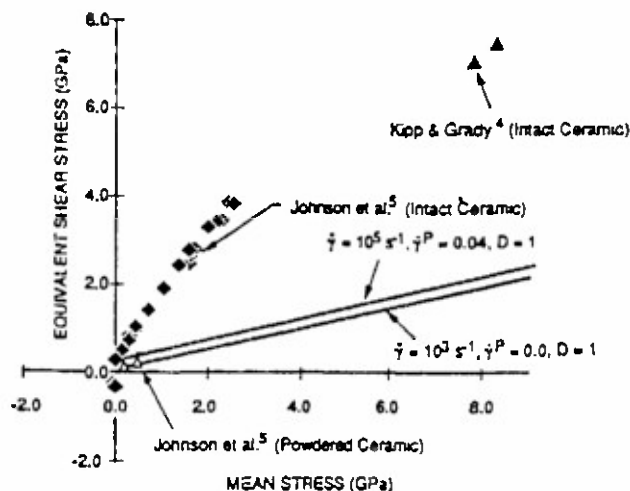Our simulations show clearly that the SiC specimen experiences a range of mean stresses, strain rates, and shear stresses, all of which contribute to the wave profile recorded at the free surface. Thus a simulation that adequately reproduces experimental results requires a material model that is effective over a relatively broad range of conditions. We have not varied the model parameters widely and thus do not know whether other combinations of model constants would give the same results or whether a Mohr–Coulomb model is the only appropriate one. To reduce the uncertainty, more experiments with different anvil thicknesses, impact velocities, and skew angles are required. However, we believe the model reasonably represents the stresses within the anvil, because the model reasonably reproduces velocity measurements at the anvil rear surface. However, extrapolation from the test conditions should be done with caution.

The results of experiment 1 (0.913 mm/μs) show two disturbing features. First, the shear wave arrived late so that the free surface did not attain a high transverse velocity until well after it was expected to. The late arrival suggests that the impact faces initially slipped because they were lubricated by gas that leaked past the projectile. Two other pieces of evidence that suggest gas leaked ahead of the projectile are the large (36 mrad) tilt and the fact that the target was moving, albeit slowly, before impact. In the absence of gas leakage (presumably the case for experiment 2), we believe that the impact faces would not slip. One reason is that the maximum possible ratio of shear stress to normal stress for a 15° impact, obtained assuming the plates remained elastic, is 0.17, which is below our inferred friction coefficient of 0.23. Furthermore, in experiments on metals, slippage only occurred for impact angles above 23° (Ref. 12) and was associated with a sudden drop in transmitted shear stress.

The second disturbing feature of experiment 1 is the oscillation of the transverse velocity. If the flyer and anvil remained elastic or if the longitudinal and shear waves were otherwise uncoupled, the velocities normal and transverse to the anvil rear surface would remain constant after the initial transient arrived, because the anvil is thinner than the flyer. We have not seen unsteady behavior reported for similar tests on metals or rocks. It is probably an artifact of scattering objects moving in and out of the LDV measurement volume. This effect is known to give false indications of turbulence in fluid anemometry.[24] The behavior may be an indication of stick-slip of the impact faces or of heterogeneous cracking of the anvil. If moving cracks emitted waves that traversed the measurement volume of the LDV, then the transverse velocity would have been perturbed. If we had measured the transverse velocity at two locations, we could tell whether the oscillations were due to a phenomenon that was uniformly distributed over a plane parallel to the plates, such as stick-slip, or to phenomena that were heterogeneously distributed, such as fracturing and LDV artifacts.

CONCLUSIONS

Comminution of sintered silicon carbide under shock loading occurs at a stress level slightly below the HEL. The strength of the highly comminuted material increases monotonically with mean stress (confining pressure) in the 1–9 GPa range and is three to six times less than the strength of uncomminuted material. The strength of comminuted material at high shear strain rates (10^5 s^{-1}) is significantly lower than at quasistatic rates and may result from rate dependence of interfragment friction. The friction coefficient of 0.23 inferred from the pressure/shear experiments reported here is smaller than that reported for quasistatic mineral-on-mineral sliding by a factor of 2–4.

A laser Doppler velocimeter is a viable cost-effective alternative to the transverse displacement interferometer and the VISAR for measuring the transverse motion of the rear surface of shock-loaded ceramic targets.

A simple nonassociated continuum model that includes dilatancy, rate dependence, and a one-parameter measure of the extent of comminution reasonably describes the measured results.

Using the experimental measurements and model, we have demonstrated a method for deducing flow properties of a fragment bed under high strain rate and confining pressure.

ACKNOWLEDGMENTS

[1] D. A. Shockey, A. H. Marchand, S. R. Skaggs, G. E. Cort, M. W. Burkett, and R. Parker, Int. J. Impact Eng. 9(3), 1 (1989).

[2] J. Mescall and C. Tracy, in Proceedings of the 1986 Army Science Conference, U.S. Military Academy, West Point, 17–20 June 1986 (unpublished).

[3] J. Mescall and V. Weiss, in Proceedings of the 29th Sagamore Army Conference, Army Materials and Mechanics Research Center, Watertown, MA, 1984 (unpublished).

[4] M. E. Kipp and D. E. Grady, "Shock Compression and Release in High-Strength Ceramics," Sandia Report No. SAND89-1461-UC-704, July 1989 (unpublished).

[5] G. R. Johnson, T. J. Holmquist, J. Lankford, C. E. Anderson, and J. Walker, "A Computational Constitutive Model and Test Data for Ceramics Subjected to Large Strains, High Strain Rates, and High Pressures," Final Technical Report on Optional Task I, Department of Energy Contract No. DE-AC04-87AL-42550, August 1990 (unpublished).

[6] H. C. Heard and C. F. Cline, J. Mater. Sci. 15, 1889 (1980).

[7] J. Lankford, J. Hard Mater. 2, 55 (1991); see also Proceedings of the 4th International Conference on the Science of Hard Materials, Madeira, November 1991 (unpublished).

[8] On a microscopic level, however, faulting is comminution and flow of fragments (fault gouge).

[9] N. S. Brar and S. J. Bless, in Proceedings of the International Conference on Shock-Wave and High-Strain-Rate Phenomena in Materials (EXPLOMET 90), edited by M. A. Meyers, L. E. Murr, and K. P. Staudhammer (Dekker, New York, 1991).

[10] W. H. Gust, A. C. Holt, and E. B. Royce, J. Appl. Phys. **44**, 550 (1973).

[11] R. W. Klopp and D. A. Shockey (unpublished); see also D. A. Shockey and R. W. Klopp, "Tests for Determining Failure Criteria of Ceramics under Ballistic Impact," Quarterly Progress Report No. 2, U.S. Army Research Office, Research Triangle Park, 15 January 1990 (unpublished).

[12] R. J. Clifton and R. W. Klopp, in *Metals Handbook*, 9th ed. (ASM International, Metals Park, OH, 1985), Vol. 8, pp. 230–239.

[13] T. C. T. Ting and N. Nan, J. Appl. Mech. **36**, 189 (1969).

[14] K. S. Kim, R. J. Clifton, and P. Kumar, J. Appl. Phys. **48**, 4132 (1977).

[15] L. M. Barker and R. E. Hollenbach, J. Appl. Phys. **43**, 4669 (1972).

[16] D. C. Erlich and P. Chartagnac, J. Phys. (Paris) Colloq. C 5, C5-455 (1985).

[17] A. S. Abou-Sayed and R. J. Clifton, J. Appl. Mech. **44**, 79 (1977).

[18] P. Perzyna, Adv. Appl. Mech. **9**, 243 (1966).

[19] J. W. Rudnicki and J. R. Rice, J. Mech. Phys. Solids **23**, 371 (1975).

[20] S. Ranganath and R. J. Clifton, Comput. Methods Appl. Mech. Eng. **1**, 173 (1972).

[21] B. D. Trott and J. G. Dunleavy, Ceram. Aware. Bull. 1970, 13 (November–December 1970), extracted from W. H. Gust and E. B. Royce, "Dynamic Yield Strengths of Light Armor Ceramics," Lawrence Radiation Laboratory Report No. UCRL-50901, 1 July 1970 (unpublished).

[22] Z. Rosenberg, Y. Yeshurun, and D. G. Brandon, J. Phys. (Paris) Colloq. C 5, C5-331 (1985).

[23] N. S. Brar, Z. Rosenberg, and S. J. Bless, "Dynamic Properties of Porous B_4C," University of Dayton Research Institute Technical Report No. UDR-TM-89-15 to U.S. Army Research Office on Contract No. DAAL03-88-K-0203, January 25, 1990 (unpublished).

[24] W. K. George and J. L. Lumley, J. Fluid Mech. **60**, 321 (1973).

FAILURE PHENOMENOLOGY OF CONFINED CERAMIC TARGETS AND IMPACTING RODS

FAILURE PHENOMENOLOGY OF CONFINED CERAMIC TARGETS AND IMPACTING RODS

Donald A. Shockey,* A. H. Marchand,* S. R. Skaggs,† G. E. Cort,†
M. W. Burkett† and R. Parker†

*SRI International, 333 Ravenswood Avenue, Menlo Park, CA 94025-3493, U.S.A.; and
†Los Alamos National Laboratory, Los Alamos, NM 87545, U.S.A.

Summary—The mechanism by which a long rod penetrates a steel-encased ceramic block was sought by performing impact experiments at a range of velocities and examining the fracture and deformation in the recovered targets and impactors. The key processes are the crushing of a small volume of ceramic adjacent to the leading surface of the advancing penetrator, and the subsequent flow of the fine fragments lateral to and then opposite the direction of attack. The results suggest that nonconventional material properties such as the dynamic compressive failure energy and the friction, flow and abrasive properties of the finely fragmented material govern the penetration resistance of confined ceramics. This understanding of penetration mechanisms can be used to guide development of specialized tests and failure models to measure pertinent material properties and to predict penetration behavior, respectively.

INTRODUCTION

When ceramic plates are used as overlays or incorporated as a layer within conventional monolithic steel armor, the ballistic protection is significantly enhanced [1]. This finding has encouraged the use of ceramics as a component of advanced armor structures and has motivated researchers to identify materials and structural configurations that maximize ballistic performance.

The design of current ceramic armors is based predominantly on empirical ballistic performance data. Test firings using the threat of interest (long rod, shaped charge jet, or small caliber ammunition) are conducted against armor specimens in which ceramic component parameters, such as type of ceramic, thickness, and spacing of plates, are varied independently and systematically. The combination of parameters that produce maximum ballistic protection is determined from test results and used to design the armor package. This procedure is lengthy and expensive, and because the number of potentially influential material and geometry variables is large, a comprehensive test matrix is not practical and so it is doubtful that armor packages affording optimal protection are attained.

A more efficient procedure is to combine experiments with computational simulations of experiments. Computations of the ballistic behavior for various impact conditions and target geometries indicate which target parameters are important and suggest combinations of target parameters that will give favorable performance. A limited matrix of ballistic experiments based on these guidelines are performed. The results are used to modify the models and the code; then a second generation of computational simulations is conducted and used to design a second set of test firings. This procedure is repeated until an armor package with acceptable performance is obtained. The reduction in the number of required test firings reduces substantially the expense and time required to attain a suitable armor, and the understanding gained promotes optimum armor design.

Implementation of the iterative computational/experimental procedure, however, requires reliable models for the microfailure behavior of ceramics and penetrators under penetration conditions. These models should be based on an understanding of the failure phenomenology during penetration. In particular, the material properties governing penetration resistance must be known. Unfortunately, conventional material properties such as fracture toughness, strength, and hardness correlate poorly with penetration behavior [2, 3], suggesting that under the complex, high-rate, multiaxial load produced by the penetrator one or more nonconventional material properties control penetration.

The goal of the work reported here was to establish the failure phenomenology of confined ceramic targets and impacting long rods during penetration, and to deduce the ceramic properties governing penetration resistance. Our approach was to perform impact experiments on confined ceramic specimens at several velocities to produce damage ranging from incipient to severe. Very early stages of damage were studied by performing experiments with low velocity spherical particles. From fractographic and metallographic examination of the targets and rods after impact, we inferred the failure mechanisms and speculate on the properties controlling penetration behavior. The study was aimed at ceramics as a class of materials and sought a qualitative understanding of penetration phenomenology to provide the basis for a computational model; therefore, experiments were performed on a variety of ceramics and details of microstructure and mechanical properties of the individual materials are not presented.

ROD IMPACT EXPERIMENTS

Tungsten–nickel–iron rods, 0.770 mm in diameter and 7.70 mm long, having hemi-spherical noses were accelerated in a powder gun to desired velocities in the $0.8-1.4$ km s^{-1} range and caused to impact a steel-encased block of ceramic at approximately zero degrees obliquity (Fig. 1). Ceramics investigated included Al_2O_3, SiC, B_4C and TiB_2.

After the impact event, the target assemblies were carefully removed from the mounting fixture and placed on the floor of the bunker with the impact surface facing up. A two-component epoxy was poured into the hole on the front cover plate to fill the crater and run into the cracks in the ceramic. This procedure was intended to strengthen the fractured ceramic block so that the confining steel could be removed and the ceramic block could be sectioned without crumbling of the fractured ceramic. We found in later

25 mm
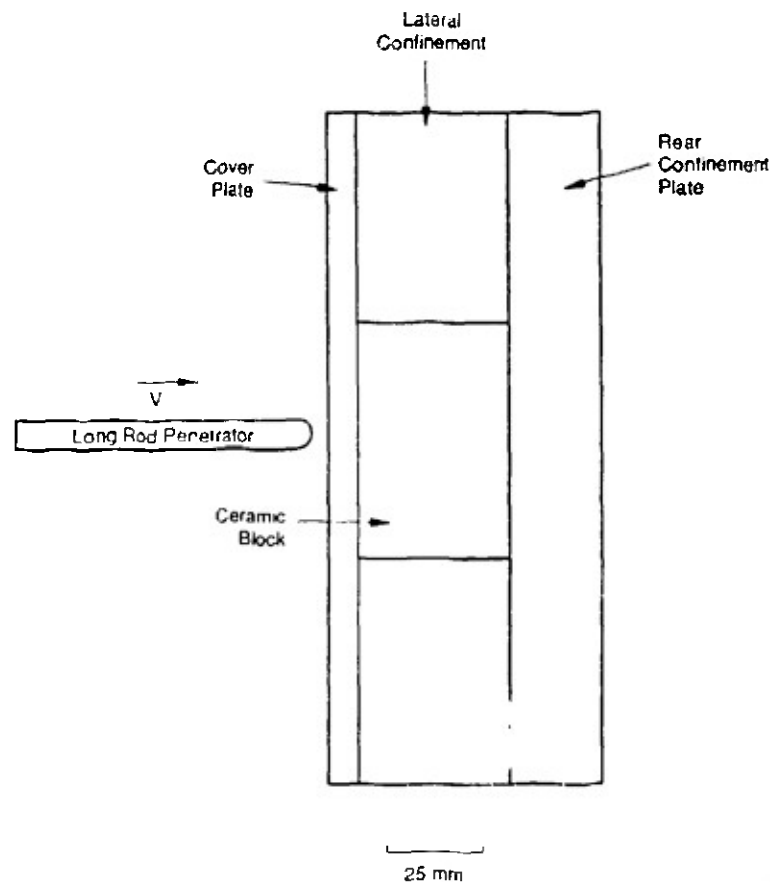
RA-M-7525-6

FIG. 1 Arrangement for rod impact experiments
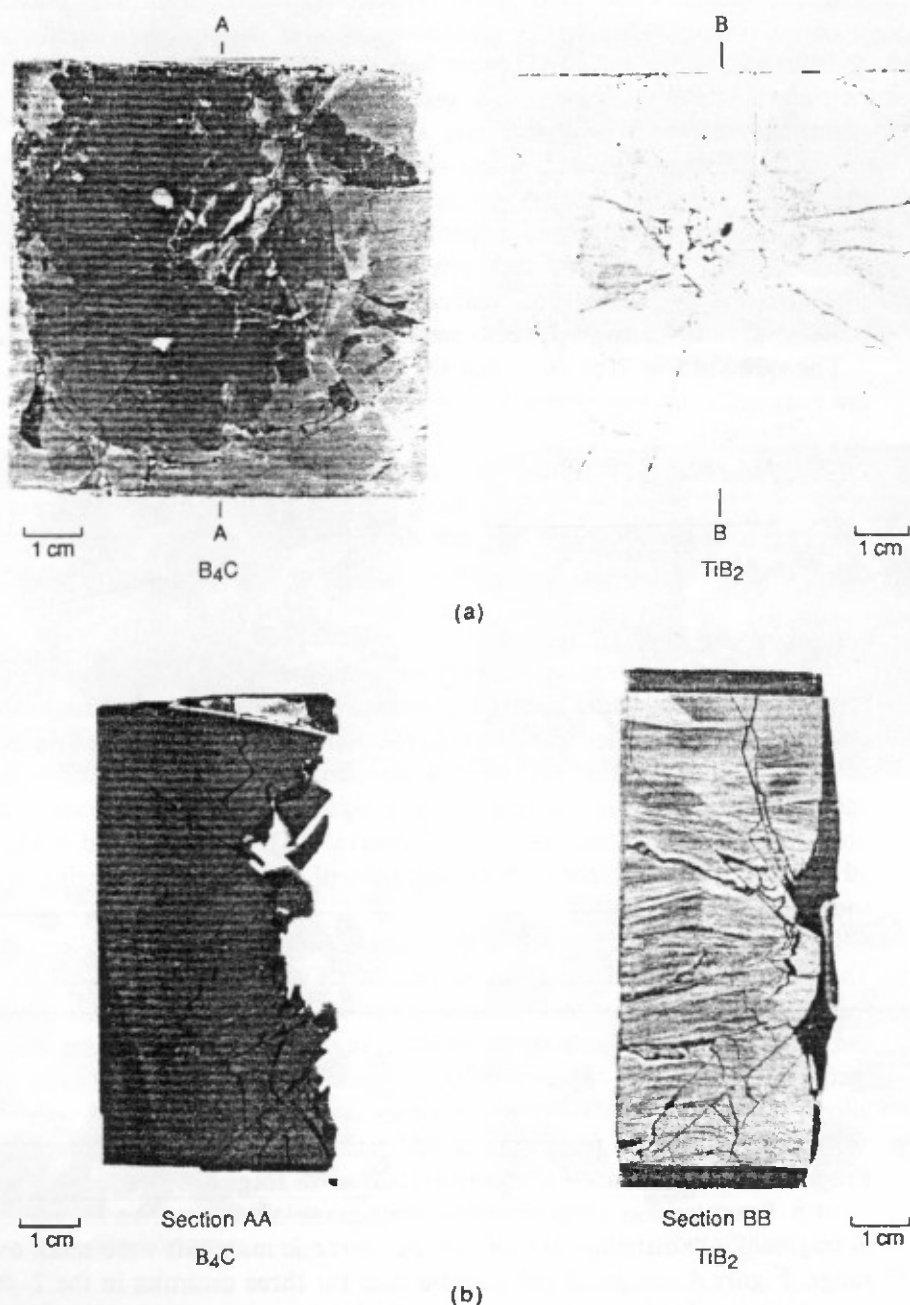
(a)

(b)

RP-3345-28

FIG. 2. Rear surface crack pattern (a) and crack patterns on cross-sections (b) in targets of B_4C and TiB_2.

experiments that impacted targets were often strong enough to be disassembled, sectioned, and even wafered without infiltration of epoxy.

The front surface of the ceramic block and the inside surface of the steel cover plate showed a starburst pattern of linear markings radiating outward from the impact site. These markings were produced by ceramic and tungsten rod fragments originating near the leading edge of the penetrator.

All ceramics tested exhibited qualitatively similar cracking patterns; however, the numbers and sizes of cracks generally differed. The crack patterns on the rear surfaces of a B_4C and TiB_2 specimen impacted at 0.8 km s^{-1} are shown in Fig. 2(a). Two main types of cracks are evident: circular cracks and radial cracks. Three to four dominant circular cracks were observed in both ceramics; however, approximately 50% more radial cracks were produced in the B_4C (23 cracks) than in the TiB_2 (15 cracks). Fracture damage was heaviest in both materials in a region directly beneath the impact site.

A diamond saw was used to cut through the crater centers on a plane containing the impact direction. Cutting the ceramic block was difficult. The diamond wheel wore out quickly and stopped cutting about halfway through the block. The wheel needed to be redressed several times before the sectioning was completed.

Orthogonal views of the craters and crack patterns were obtained on the as-sawn, unpolished section surfaces. These surfaces for a B_4C and a TiB_2 specimen are shown in Fig. 2(b). Crater size was greater in the B_4C. Material directly beneath the crater in the TiB_2 specimen remained intact, probably because of the triaxial compressive stress state and the higher compressive yield strength of TiB_2. At higher velocities resulting in deeper rod penetration, the material in advance of the tip of the penetrator was crushed to a fine powder. Similar damage patterns were observed in Al_2O_3 and SiC targets.

The views in Fig. 2(b) show that the circular cracks in Fig. 2(a) are traces of cracks that ran outward at an angle from the impact site. The resulting cone configuration corresponds to the Hertzian cracks observed in the particle impact experiments reported in the following section and observed by others in ceramics and glasses under static indentation and particle impact [4, 5]. The lateral cracks lying roughly parallel to the surface apparently formed after the cone cracks, since they are discontinuous across the cone cracks. Thus, lateral cracks may be produced by tensile stress waves reflecting from the specimen boundaries or by later unloading of the target. Radial cracks are not revealed on cross-sections containing the impact direction.

In several instances, tungsten fragments were observed lodged between faces of Hertzian cone cracks. That these fragments were not moved into the cracks by the sectioning operation was confirmed by computed tomography results that showed fragments in cracks in unsectioned specimens. Such observations suggest that debris emanating from the eroding end of the penetrating rod can have a significant forward velocity component. These observations support the premise of Hauver [6], who observed tungsten fragments in advance of the penetrator in X-radiographs of ceramic blocks during impact by tungsten rods.

Loose fragments produced in the impact experiments were collected for examination. The size distribution of the collected fragments was determined by a sieve analysis (placing the recovered fragments on the topmost of a stack of successively finer screens and vibrating the stack for 1 h). We separated ceramic fragments from penetrator fragments by passing a strong magnet over the sieved fragments and extracting the slightly magnetic tungsten alloy fragments from the ceramic debris.

Figure 3 shows the fragments of SiC retained on screens with various mesh openings. Fragment shape did not vary substantially with fragment size: aspect ratios ranged from 1-ca 3. Fracture was predominantly transgranular rather than intergranular. Differences in fragment size distributions for the four ceramic materials were small over the entire size range. Figure 4 compares the distributions for three ceramics in the 2-40 μm size range.

In higher velocity experiments, in which the rod penetrated 60-100 mm, the crushed ceramic material produced at the leading edge of the rod flowed around and behind the rod, closing the hole made by the rod (Fig. 5). So well consolidated were these fine fragments that no fragments were loosened during sectioning and individual fragments were not easily discernible by high magnification examination. Hardness and scratch tests indicated strengths of the compacted powder comparable to that of the unimpacted material. In Fig. 5, the penetrator has stopped just short of the rear confinement plate.

The debris from several targets was searched for distal portions of the penetrator. Distal portions ranging in length from 3-20 mm were found [Fig. 6(a)]. Proximal ends had either a mushroom shape or a sharpened pencil shape. We speculate that a penetrator tip may alternate shapes between that of a mushroom and a pencil point several times during the penetration process. Initially, we expect plastic deformation of the leading edge to produce a mushroom shape. The mushroom zone then shears away on roughly a 45 conus, producing a pencil point. The pencil point then deforms plastically and the tip acquires a mushroom shape again; this mushroom shape becomes unwieldy and shears to a pencil point. This alternating shape change continues until penetration ceases. The

<38 μm

43-74 μm

74-175 μm

246-594 μm

991-2794 μm

Over 2794 μm
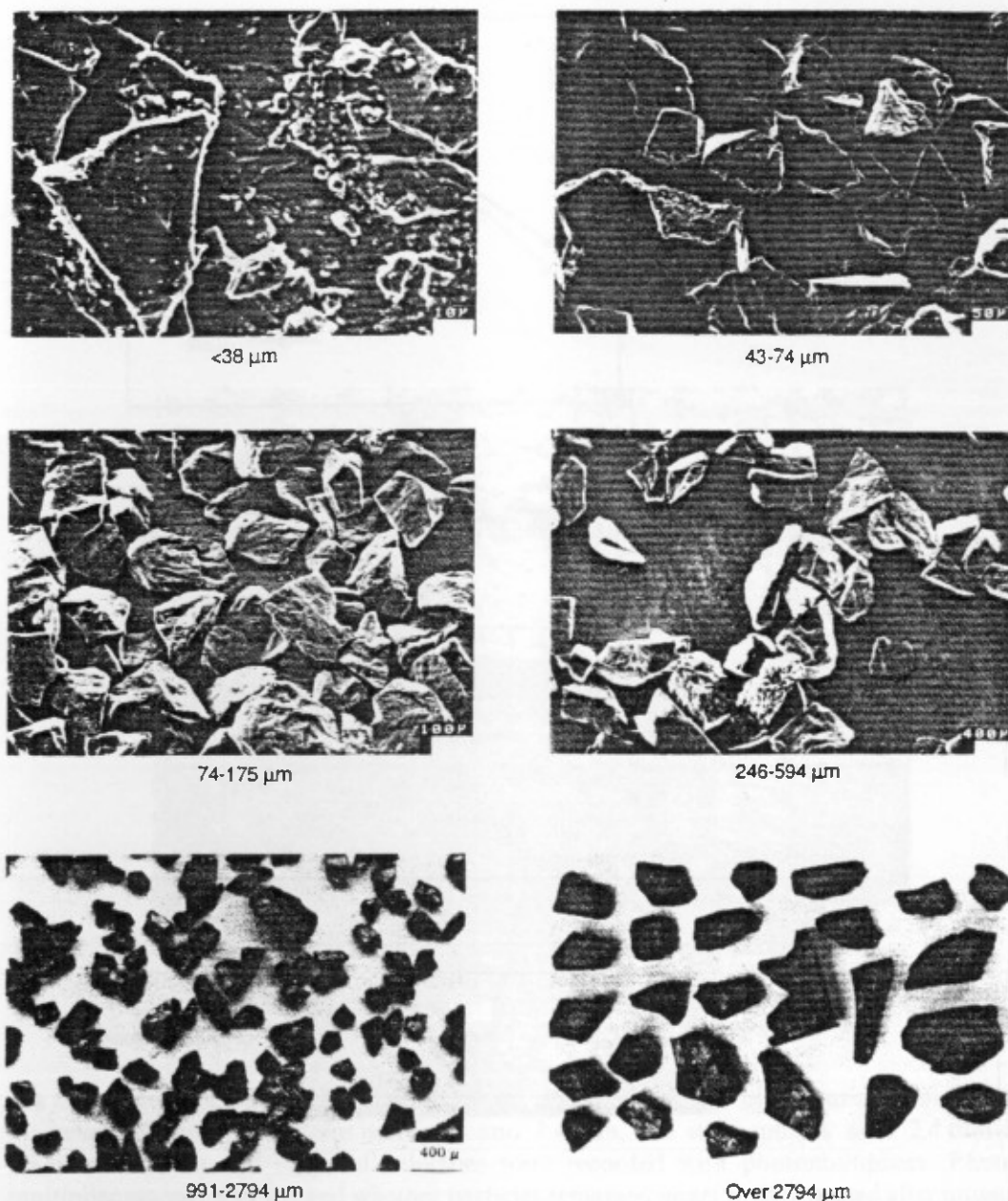
RP-7525-9

FIG. 3. Fragments from a SiC target retained on screens with different mesh openings.

proximal end surfaces of all recovered penetrators were faceted and gouged, suggestive of shear failure. The lateral surfaces were unscored.

Polished and etched cross-sections on planes containing the rod axis revealed that the tungsten particles in this sintered alloy retained their original roughly spherical shape everywhere except near the proximal failure surface. Adjacent to the failure surface, the tungsten particles were greatly elongated, often to aspect ratios of 5 or more. Particle distortion decreased with distance from the failure surface, rather gradually (over a distance of about 4 mm) in the mushroomed region. Thus, the distribution of deformed tungsten particles provides a map of the plastic strain field in a penetrator.

Tungsten fragments extracted magnetically from the debris ejected from the impact surface were also examined with a scanning electron microscope. Failure surfaces and etched cross-sections suggested that fragment formation was by localized shearing of the microstructure, in accord with observations on distal penetrator ends. Tungsten particle distortion in the fragments, however, decreased abruptly (usually within about 300 μm) from the surface of fragments [Fig. 6(b)].
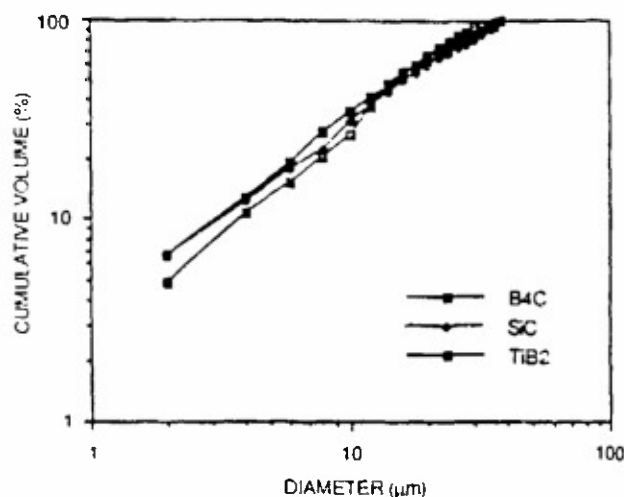
FIG. 4. Distribution of fragments of B₄C, SiC and TiB₂ in the 2-40 μm size range.
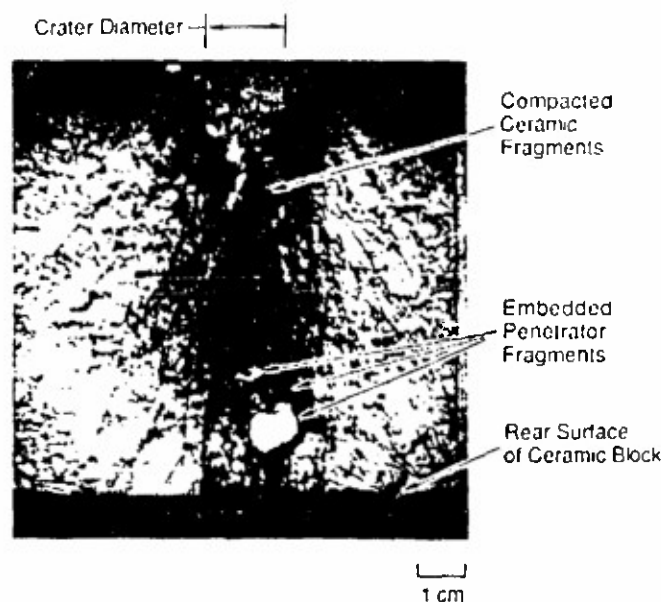
FIG. 5. Cross-section through shot line of 100 mm thick confined B₄C target impacted at a higher velocity showing cracking pattern, compacted ceramic fragments in cavity produced by penetrator and embedded penetrator fragments.

We computationally simulated the experiment depicted in Fig. 1 using a two-dimensional, Lagrangian finite difference code. The results provided an estimate of the distribution and time variation of the stresses and strains produced in the ceramic target by the impacting long rod before failure occurred, and assisted in the interpretation of the fractographic observations.

PARTICLE IMPACT EXPERIMENTS

Low velocity particle impact experiments were performed to study incipient stages of impact damage. The evolution of fracture damage was established in hot pressed (HP) silicon nitride by accelerating single solid spheres of tungsten carbide (WC) or steel onto the polished surfaces of small plate specimens of HP Si_3N_4 at a 90° angle [7]. Particles were accelerated to velocities from 16-368 m s⁻¹ by filling the gun chamber with nitrogen
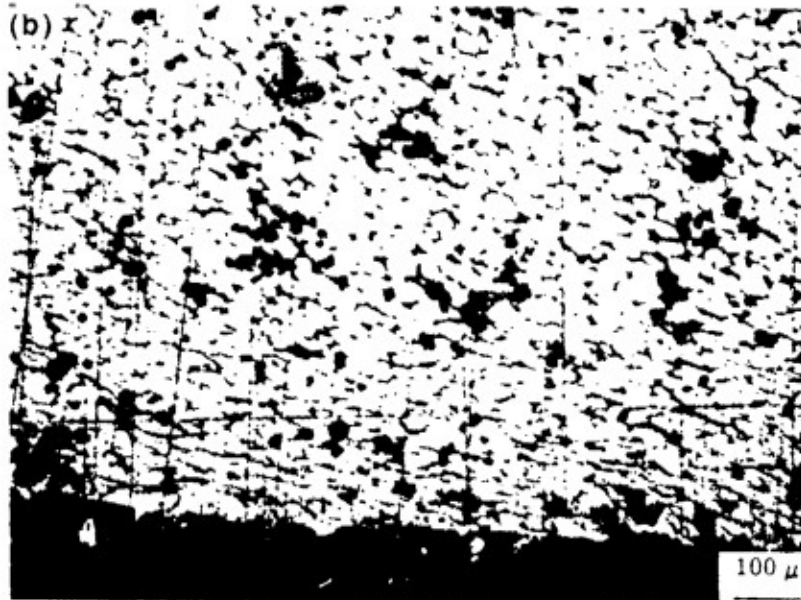
(a)

(b)

100 μ

FIG. 6. Distal portions of tungsten alloy rods recovered from ballistic experiments (a) and polished and etched cross-section showing deformation of the microstructure (b).

gas to various pressures, then suddenly releasing the nitrogen by rupturing a disk. The diameters of the WC spheres were 1.6 and 2.4 mm; the steel spheres were 2.4 mm in diameter. Impact and rebound velocities were recorded with photomultipliers. Photomultiplier records also showed whether particles remained intact or fragmented after impact. The specimen fracture damage was studied by optical and scanning electron microscopy of impact surfaces and polished cross-sections normal to the impacted surfaces.

The impact tests caused several kinds of cracks, small craters and fragmentation in the target plates and eventually plastic deformation or fracture of the impacting spheres. Targets sustained no damage at impact velocities below 17 m s^{-1}, at which point ring cracks appeared. As impact velocity increased, the damage progressed to cone cracks, an inelastic impression, radial cracks, lateral cracks, and median-vent cracks. Ring cracks, as shown in Fig. 7, are circumferential cracks that extend less than a millimeter beneath the surface. As the impact velocity increased, more and longer ring cracks formed [Fig. 7(b)]. The ring cracks are similar to the Hertzian ring cracks formed under quasi-static loading [8]. The surface ring cracks that start approximately normal to the specimen surface veer outward at various angles up to about 75 from the vertical to become Hertzian cone cracks [9]. As the velocity increases, additional cone cracks form both inside and outside the existing damage umbrella, and the innermost cone grows several millimeters in depth.

An inelastic impression and radial cracks [Fig. 7(c)] seemed to form at the same time in the failure sequence. As the impression deepened with increasing velocity, the radial cracks grew in both size and number, although only a small number (8 or 9) of the radial cracks grew to several millimeters [Fig. 7(d)].
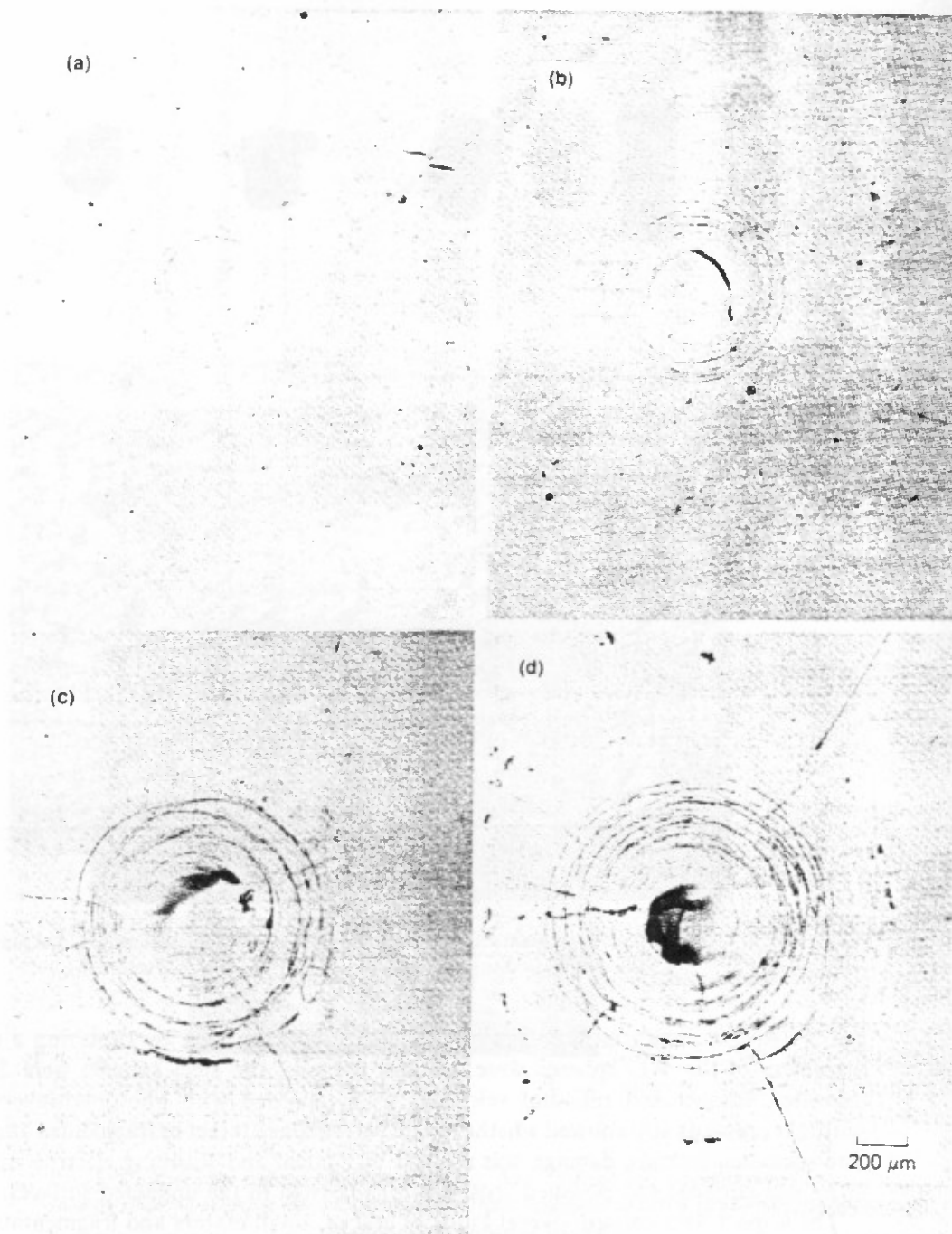
FIG. 7. Cracks on the surface of HP Si_3N_4 caused by impact of 2.4 mm diameter tungsten carbide spheres at velocities of (a) 19.5 m s^{-1} (b) 46.2 m s^{-1} (c) 97.7 m s^{-1} and (d) 159 m s^{-1}.

Figure 8 shows the internal damage and the extent of growth of the various cracks below the specimen surface. The nucleation and growth sequence of the ring/cone cracks is illustrated in Figs 8(a) and 8(b). Under increasingly severe impacts, cone cracks seemed to cease growing; instead, two new types of cracks were created, as shown in Fig. 8(c). Lateral cracks nucleated internally near the contact center and ran approximately parallel to, and eventually veered toward, the impact surface of the specimen. Vertical cracks initiated internally in the region within the innermost cone crack. These latter penny-shaped cracks are similar to the median-vent cracks observed by Evans and Wilshaw in quasi-static indentation experiments on ZnS [8]. Observations with polarized light showed that a zone of densely microcracked material, approximately spherical in shape, was formed beneath
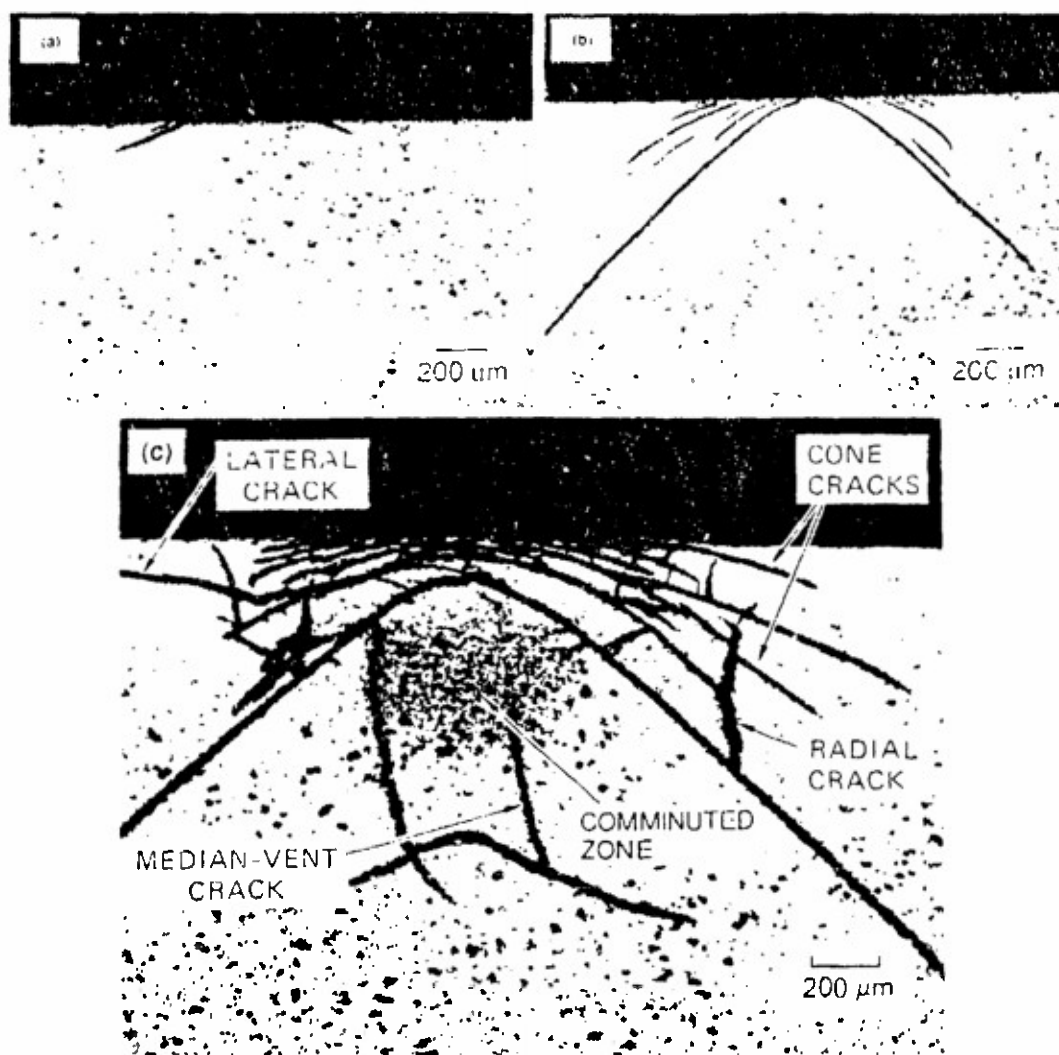
FIG. 8. Sectional views of subsurface cracking pattern in HP Si_3N_4 impacted by 2.4 mm diameter steel spheres at velocities of 56.4 m s^{-1} (a) and 231 m s^{-1} (b) and by a 2.4 mm diameter tungsten carbide sphere at 231 m s^{-1} (c).

the contact area. Zinc sulfide impacted by 0.4 and 0.8 mm WC spheres exhibited a similar microcracked zone [10].

Impacting steel spheres, which are softer than tungsten carbide, caused only ring and cone cracks and introduced little additional damage above 300 m s^{-1}, at which velocity the particle failed by plastic deformation. This limit on the damage inflicted on the ceramic occurs because the particle cannot exert a pressure on the ceramic greater than the particle's yield strength. Since the yield strength of the steel is less than the pressure required for inelastic deformation of the ceramic surface, higher velocity impacts only result in more deformation of the steel sphere.

FAILURE PHENOMENOLOGY OF THE PENETRATION PROCESS

The picture of the penetration process that begins to emerge from these observations and consideration of the initial stress history is as follows.

Calculational simulations of a tungsten alloy rod impacting a target as in Fig. 1 at 1600 m s^{-1} show that at the instant of impact, a shock wave with an amplitude of several hundred kbars is generated at the impact site. Radial divergence and plastic flow and fracture in the steel cover plate quickly and drastically reduce the stress so that the strength of the shock that passes into the ceramic is below the Hugoniot elastic limit. Thus, the

initial shock wave is not expected to condition the ceramic. A steady-state ramp wave follows the shock, loading the ceramic material at the tip of the penetrator to a maximum compressive stress of about 50–60 kbars. The ceramic initially resists the stress in the ramp wave and exerts large stresses on the tungsten rod, which may deform, fracture or be deflected.

Ceramics are substantially stronger in compression than in tension, and consequently, the tensile strength of the ceramic is exceeded at the impact surface near the rod periphery and tensile fracture begins to occur soon after impact. The stress fields in the ceramic are initially elastic, and the largest tensile stresses are in the radial direction (the Boussinesq stress field). Therefore, the cracks that form (normal to the direction of maximum principal stress) are ring cracks concentric about the impact site. These cracks are shallow cracks, extending initially only a millimeter or so beneath the ceramic surface. Upon continued loading, however, several ring cracks continue to grow and, following the paths normal to the direction of the principal tensile stress, assume angled trajectories 25–75° outward from the initial normal-to-the-surface direction. Thus, several large Hertzian cone cracks extend through the ceramic block, intersect the specimen surfaces, and cause structural failure of the target.

Up to this point, the stress fields and the fracture response are elastic. But as the rod continues to advance, the compressive strength is exceeded in material directly beneath the penetrator. Microcracking occurs in a shallow zone near the penetrator tip, and the stress field changes in character. The principal tensile stresses are now in the circumferential direction, and a new type of tensile crack is invoked—six to twelve large radial cracks run outward from the impact site like spokes from a hub [9]. These cracks intersect the impact surface and may extend to all specimen boundaries, resulting in strength degradation and eventual structural failure of the target.

A third crack type, lateral cracks, form beneath the impact surface and propagate roughly parallel to it, probably during ι loading. These cracks intersect cone cracks and radial cracks, thereby providing the orthogonal surfaces necessary for fragment formation. Cratering results when these large fragments are liberated from the vicinity of the impact site.

The tensile cone, radial, and lateral cracks do not provide an easy path for penetrator advance and hence do not assist the penetration process directly. Intact and laterally confined ceramic remains in the penetrator path despite the presence of these tensile cracks, and this material must be moved out of the way for the penetrator to advance. This occurs by pulverization of the ceramic material in a shallow zone immediately ahead of the penetrator and the subsequent flow of this material laterally and opposite to the impact direction, processes that occur under large compressive and shear stresses.

Thus, the development of a densely microcracked zone in a ceramic directly ahead of the impactor is a prerequisite for penetration. Insight into how this zone forms can be gleaned from the observations of Hagan and co-workers [11, 12] of damage zones in soda-lime glass and zinc sulfide produced by quasistatic indentation. These workers observed a curvilinear grid of narrow, fault-like flow lines beneath indentations, and voids and microcracks at many of the nodes in the grid. Flow in the polycrystalline ZnS occurred by slip and twinning within the grains and by grain boundary sliding; voids formed when grain boundary displacements became large either along the flow lines or at flow line intersections.

The finely fragmented material at the leading edge of the penetrator wants to occupy a larger volume (i.e. dilation), but expansion is resisted by the confinement of the steel encased ceramic block. The resulting increase in pressure makes fragment flow more difficult and adds to the resistance exerted on the penetrator. The tensile cracks may assist penetration indirectly by reducing the level of constraint on the pulverized material, thereby allowing easier flow of the material out and away from the advancing penetrator, but the main resistance to penetration is probably coupled to the flow characteristics of highly comminuted ceramic powder. The cracking pattern in the ceramic target envisioned during the steady-state phase of the penetration process is depicted in Fig. 9.

As the ceramic particles flow across the leading surface of the penetrator, they erode
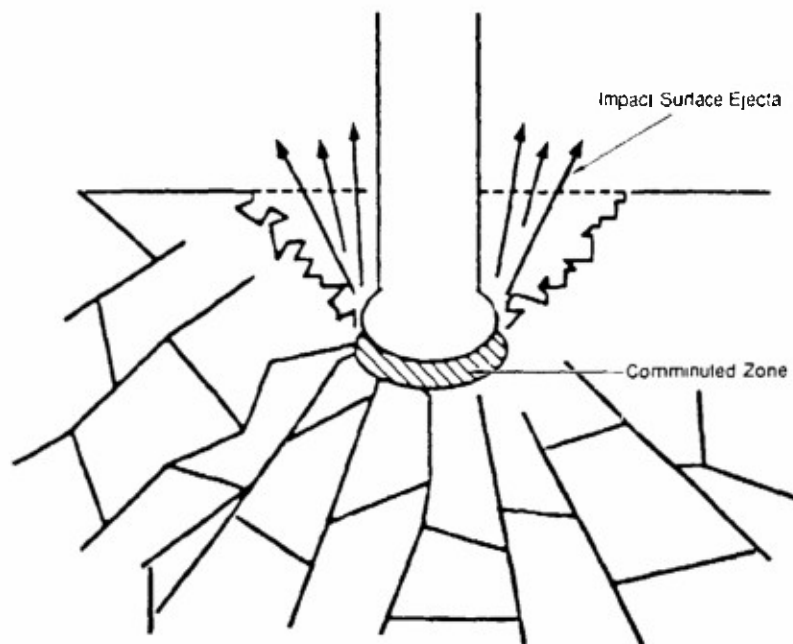
RA-7525-8

Fig. 9. Cracking pattern in ceramic targets during the steady-state phase of the penetration process.

the rod, shortening and eventually consuming it as the rod moves through the ceramic. No scoring or erosion of the sides of the penetrator results from particles flowing opposite the direction of penetration. Fragments of the penetrator fretted from the leading surface generally have an initial forward velocity component and may travel into open cone and radial cracks ahead of the tip of the penetrator. Other penetrator fragments mix with and flow with the ceramic powder, becoming part of the front surface ejecta. The eroded tungsten fragments exhibit greatly elongated grains close to the fragment surfaces, indicative of heavy localized plastic flow.

CONCLUSIONS

According to this concept of penetration phenomenology, the properties of a ceramic that govern penetration resistance include the compressive strength and hardness, the pulverization characteristics, the frictional flow characteristics of fine fragments, and fragment abrasiveness. These properties are consistent with those suggested by Mescall [13, 14].

Initial resistance to penetration is provided by the compressive strength or hardness of a ceramic. High compressive strength is desirable to deform, fracture and deflect an impacting body. Projectiles with low aspect ratios can be defeated if the strength of the ceramic exceeds the strength of the projectile. High aspect ratio projectiles such as long rods, may suffer heavy deformation and fracture damage to the proximal end, but the intact distal portion will continue to advance and penetrate the ceramic. Thus, a high ceramic compressive strength can resist penetration only to a certain extent.

The stresses exerted by a long impacting rod will eventually pulverize the ceramic material in a small zone immediately ahead of the leading surface of the penetrator. As explained in the following paragraph, production of a pulverized zone is a necessary condition for a penetrator to advance in a confined ceramic target. Thus, resistance to comminution is desirable for penetration resistance. Although the specific fracture surface energy for most ceramics is small in tension, the energy required to produce a unit of failure surface area under large dynamic compressive and shear forces may be significantly greater. Thus,

the energy absorbed in creating the surface area of the powder may be a significant ceramic property for penetration resistance.

A penetrator can only advance if the material in its path is pushed ahead of it or to the side. Because of heavy rear confinement, the crushed ceramic cannot be pushed ahead and out the rear surface in the way that metallic armor plates fail by plugging. And if the ceramic is nonporous and snugly confined laterally, the pulverized material cannot be pushed to the side. Indeed, the only recourse is for the powder to flow opposite the penetration direction along the cavity being produced by the penetrator. Thus, the pulverized and dilated ceramic must flow under high pressure, and so the frictional flow property of the comminuted ceramic should influence penetration resistance. We expect this property to depend on pressure, strain rate and size and shape of the fragments, and to be describable by a Mohr–Coulomb type curve. For thick, highly confined ceramic blocks, the friction–flow property of ceramic fragments may be the most important material property for penetration resistance.

Finally, the ability of a ceramic to erode a penetrating rod is a desirable property for penetration resistance. Whereas erosion may be by gross local plastic flow of the leading rod surface, ceramic fragments that gouge, score, shear or otherwise abrade the rod material may reduce the incoming mass and terminate the penetration earlier than non-abrasive target materials. Wear and erosion can occur by a number of mechanisms depending on penetrator and target material, fragment geometry and size, pressure, temperature, and flow rate. Thus, optimal erosive behavior might be achievable by matching the abrasive characteristics of a ceramic material to the threat.

The fractographic observations and the deduced penetration phenomenology reported here can also be used to identify properties governing the penetration capability of rods. To be effective as a penetrator, a material should have high density to produce high stresses in the target, a high yield strength to resist mushrooming at the leading edge, a high work hardening rate to suppress the tendency to shear band and fret, a high fracture toughness to resist the propensity for rod shaft failure, and high abrasion resistance to resist scoring and erosion by ceramic particles.

In future work, this understanding of penetration phenomenology will be used to develop tests that measure dynamic shear strength and flow resistance of intact and fragmented ceramic material under high confining pressure, and to develop computational models of penetration that can be used to assist in designing ceramic armor.

REFERENCES

1. F. S. MASCIANICA, Ballistic technology of lightweight armor materials. U.S. Army Materials Research Agency, AMRA MS 64-07, September 1964. updated in 1981, AMMRC Report 81-20, Army Materials and Technology Laboratory, Watertown, Massachusetts, U.S.A.

2. D. VIECHNICKI, W. BLUMENTHAL, M. SLAVIN, C. TRACY and H. SKEELE, Armor Ceramic—1987. Proceedings of The Third TACOM Armor Coordinating Conference, 17–19 February 1987, Monterey, California, U.S.A.

3. W. RAFANELLO, B. BRUBAKER and R. HOFFMAN, Evaluation of a new low-cost aluminum nitride armor. Proceedings of the Fifth TACOM Armor Coordinating Conference, 7–9 March 1989, Monterey, California, U.S.A.

4. B. LAWN and T. R. WILSHAW, Review of indentation fracture: principles and applications. *J. Mater. Sci.* 10, 1049–1081 (1975).

5. A. G. EVANS, Impact damage in ceramics, in *Fracture Mechanics of Ceramics*, Vol. 3 (Edited by R. C. BRADT, D. P. H. HASSELMANN and F. F. LANGE), p. 302. Plenum Press, New York (1978).

6. G. HAUVER, U.S. Army Ballistic Research Laboratory, personal communication.

7. K. C. DAO, D. A. SHOCKEY, L. SEAMAN, D. R. CURRAN and D. J. ROWCLIFFE, Particle impact damage in silicon nitride. SRI International Annual Report, Part III, to the Office of Naval Research, Arlington, Virginia, Contract N00014-76-C-0657 (1979). A more accessible reference is. D. A. SHOCKEY, D. J. ROWCLIFFE, K. C. DAO and L. SEAMAN, Particle impact damage in silicon nitride. *J. Am. Ceram. Soc.* (1990), in press.

8. A. G. EVANS and T. R. WILSHAW, Quasi-static solid particle damage in brittle solids - I. Observations, analyses and implications. *Acta Metallurgica* **24**, 939-956 (1976).

9. A. G. EVANS, M. E. GULDEN and M. ROSENBLATT, Impact damage in brittle materials in the elastic-plastic response regime. *Proc. R. Soc. Lond.* **A361**, 343 (1978).

10. D. A. SHOCKEY, K. C. DAO, L. SEAMAN and D. R. CURRAN, Nucleation and growth of cracks in CVD ZnS under particle impact. SRI International Annual Report, Part II, to the Office of Naval Research, Arlington, Virginia, Contract N00014-76-C-0657 (1979).

11. J. T. HAGAN, Shear deformation under pyramidal indentations in soda-lime glass. *J. Mater. Sci.* **15**, 1417-1424 (1980).

12. S. VAN DER ZWAAG, J. T. HAGAN and J. E. FIELD, Studies of contact damage in polycrystalline zinc sulphide. *J. Mater. Sci.* **15**, 2965-2972 (1980).

13. J. MESCALL and C. TRACY, Improved modeling of fracture in ceramic armor. Proceedings of the 1986 Army Science Conference, U.S. Military Academy, West Point, 17-20 June 1986.

14. J. MESCALL and V. WEISS, Materials behavior under high stress and ultrahigh loading rates - Part II. Proceedings of the 29th Sagamore Army Conference, Army Materials and Mechanics Research Center, Watertown, Massachusetts, U.S.A. (1984).

A MICROMECHANICAL MODEL FOR GRANULAR MATERIAL AND APPLICATION TO PENETRATION OF CERAMIC ARMOR

A MICROMECHANICAL MODEL FOR GRANULAR MATERIAL AND APPLICATION TO PENETRATION OF CERAMIC ARMOR

Donald R. CURRAN, Lynn SEAMAN, and Thomas COOPER

SRI International, 333 Ravenswood Avenue, Menlo Park, CA 94025, USA

Ceramics and brittle geologic materials can deform nonelastically under compression and shear by sliding and ride-up of fragments, grains, or blocks, with accompanying competition between dilatancy and pore compaction. This paper describes a micromechanical model of such deformation based on an analogy to the dynamics of atomic dislocations and using the slipping processes in a multiple-plane plasticity model. In the analogy, atomic lattice slip planes are replaced by slip on interfaces between blocks, and atoms are replaced by fragments, grains, or blocks. The model treats intact material, a gradual transition to fragments, and then the behavior of the fragments.

The coefficient of friction between the grains (tan $\phi = 0.11$) was determined for aluminum nitride through simulations of a pressure-shear impact experiment. The calibrated model was then used with a finite-element computation of the penetration of a long tungsten rod into an aluminum nitride target. The calculations successfully exhibited the key features observed experimentally, such as the rubblized zone just ahead of the penetrator and the dilatant rebound of the ceramic behind the penetrator. The most important microscopic material property governing depth of penetration was found to be the friction between granules in the rubble ahead of the penetrator.

1. INTRODUCTION

Hard, brittle materials often deform nonelastically by fracture, fragmentation, and subsequent frictional sliding and rotation of fragments. The sliding produces additional ride-up friction and associated dilatancy. The dilatancy is counteracted by pore compaction under confining pressure. These processes are especially evident in the eroding "process zone" or "Mescall zone" at the nose of a long metallic rod penetrating a ceramic armor. Another example is the "block motion" in faulted geologic materials exposed to ground shocks produced by earthquakes or nuclear weapons. Hard sands also deform by grain sliding or rolling, ride-up, and compaction.

We developed a micromechanical model for motion of granular beds and calibrated it by computationally simulating a pressure-shear gas-gun impact. We then used this model to compute the penetration of a long rod into ceramic.

Attempts to develop a micromechanical model for such behavior usually focus on building continuum constitutive relations that average microscopic fracture or grain movement processes.[1-5] For our model, we described the motion of lines of voids between the moving objects, as in atomic dislocation theory. Our model combines fracture and slip-induced softening processes, compressive behavior (including pore compaction), and dilatancy.

2. MODEL DEVELOPMENT

In developing the model, we visualized an aggregate of blocks or grains that are initially tightly packed. When a large shear strain is applied to this aggregate, grains may slide or roll over each other, but as they move, they develop voids because the material cannot remain tightly packed during the motion. The slipping can occur only on the available planes of the blocks and not on the orientations of maximum shear stress. These considerations led us to a model that is based on the Orowan[6] equation relating plastic strain rate to the number, size, and velocity of dislocations. In our case the plastic strain is the inelastic shearing deformation associated with sliding (rolling is not treated), and the dislocations are the blocks or grains. The basic relation, which is derived elsewhere,[7] is

$$d\gamma_i^P/dt = (\tau_i - \mu\sigma_{ni})/(\rho_s C_t^2 T) \qquad (1)$$

where γ_i^P is the plastic strain on the ith plane, τ_i is the shear stress, μ is the tangent of the friction angle, σ_{ni} is the normal stress on the plane, ρ_s is the solid density, C_t is the speed of transverse (shear) waves, and $T = B/(2gf_i C_t)$, a time constant. B is the block dimension, g is a factor on the order

of 1 relating the active slip system to the shear strain direction, and f_i is the fraction of blocks that have an adjacent hole large enough to allow slip into it.

Next we note that the porosity (ϕ) increases in proportion to the plastic shearing strain (a dilatant process) and decreases by compaction. We write the dilatancy expression as

$$d\phi/dt = a\ d\gamma_i^P/dt + d\phi_c/dt \qquad (2)$$

where $d\phi_c/dt$ is a compaction rate and a is a dilatancy coefficient on the order of 1. To define the compaction process, we used the compaction curve developed by Carroll and Holt.[6] The curve is given by an implicit relation between pressure and density. With the formulation represented by Eq. (2) and the compaction curve, when we shear the material at constant volume and cause plastic shearing strain, the pressure rises in accordance with Eq. (2). When this pressure reaches the compaction curve, the pressure ceases to rise and the material maintains that porosity.

Eqs. (1) and (2) are solved with the elastic-plastic deviator stress relations and a Mie-Grüneisen relation for pressure to determine the stress state.

The preceding constitutive model for granular flow was incorporated into a multiple-plane plasticity model for computational simulations of dynamic loading problems. The computational model (termed FRAGBED) has the following features:

- Nine planes on which all slip and fracture occur, as seen in Figure 1.

- The granular flow and dilatancy processes, porosity model, and Mie-Grüneisen relation mentioned above.

- Yield and tensile strengths that are reduced by the developing fragmentation.

3. CORRELATION OF THE MODEL PREDICTIONS WITH EXPERIMENTAL DATA

To test and calibrate the FRAGBED model for ceramic material, we made computational simulations to represent several laboratory experiments for AlN. The static tests of Heard and Cline[9] and the dynamic tests of Lankford[10] were
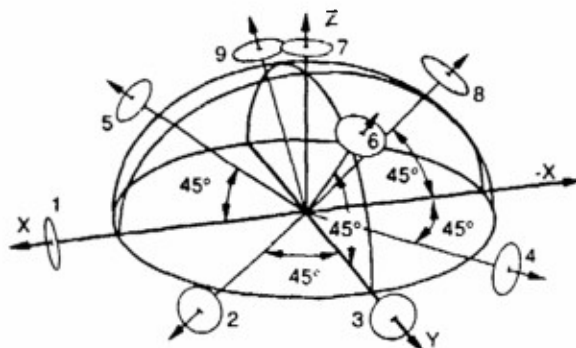
FIGURE 1
Initial orientations of the slip planes in the FRAGBED model.

simulated using the intact properties of the AlN with a Coulomb yield strength of $\mu = 0.33$, density of 3.26 Mg/m^3, bulk modulus of 210 GPa, initial yield of 3.0 GPa, and a shear modulus of 126 GPa.

A more detailed study was made of the pressure-shear impact test of Shockey and Klopp.[11] The geometry of the experiment is shown in Figure 2. A laser interferometric transverse velocity measurement at the rear surface of the boron carbide anvil was interpreted to show a constant normal stress of 10.9 GPa and a nearly constant σ_{xy} in the AlN of 1.78 GPa. Several one-dimensional wave propagation simulations (with the FRAGBED model) were made of this experiment to obtain appropriate parameters.
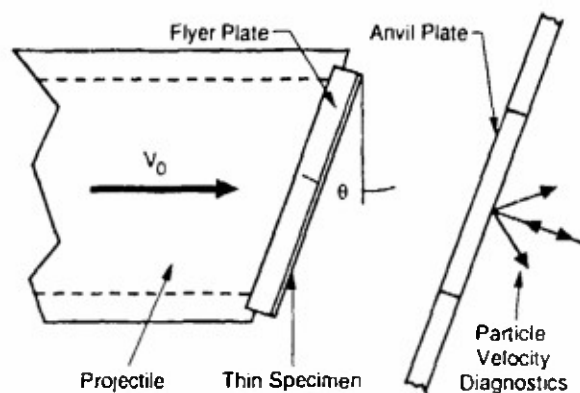
FIGURE 2
Configuration for pressure-shear slanted impactor experiment.

Our results indicate that, during the passage of the initial compressive wave, planes 2, 4, and 5 (all at 45° to the loading axis, as shown in Figure 1) received sufficient shearing strain to eliminate their cohesive strength. The renewed loading that occurred during the passage of the shear wave brought the shear stress on the fifth plane (45° between X and Z) to yield again, but did not cause slip on any other plane; hence, this plane controlled the subsequent yielding and flow. With the coefficient of friction of $\mu \approx 0.11$ (a surprisingly low value), the model represented well the measured motions. The computed normal and shear stress and the yield strength on the plane are shown in Figure 3.
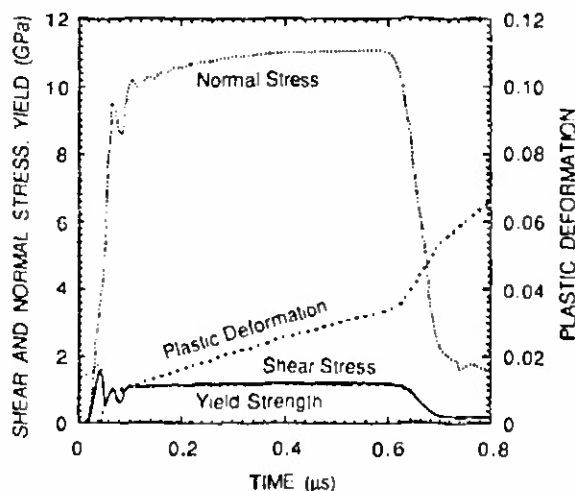

FIGURE 3
Normal and shear stress, yield strength, and plastic deformation on plane 5 in slanted impactor test in aluminum nitride.

4. PENETRATION CALCULATIONS

Penetration calculations were performed to study the ceramic behavior near the head of the penetrator. In the test configuration shown in Figure 4, the tungsten penetrator has a length-to-diameter ratio of 10 and impacts at 1.6 km/s. One sample of the computed results is shown in Figure 5. At 80 µs the penetrator has been heavily deformed and nearly stopped. Surrounding the penetrator is a rubblized zone, partially fractured zone, and an intact zone. The contours labeled "fracturing material" indicate the transition

from intact to fully fragmented. Here it is clear that the model is not following individual large cracks (which may occur in actual penetrations), but represents only a general rubblization of the material.
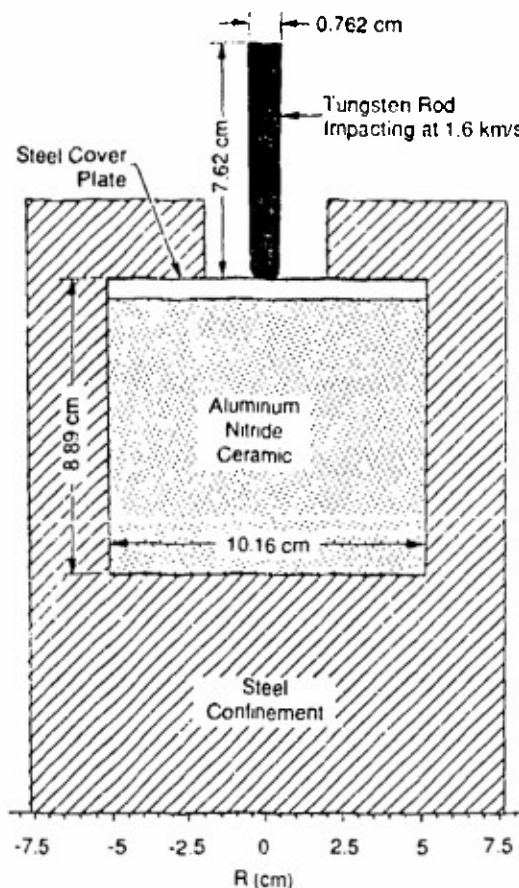

FIGURE 4
Geometry of penetration calculations.

The locations and sizes of these zones correspond well with observations of ceramic targets following penetration tests. Behind the penetrator (top of the figure), the granulated ceramic closes up the hole made by the penetrator (as observed). The flume of highly expanded ceramic powder that rose behind the penetrator is not shown. The most important microscopic material property governing depth of penetration was found to be the friction between granules in the rubble ahead of the penetrator.
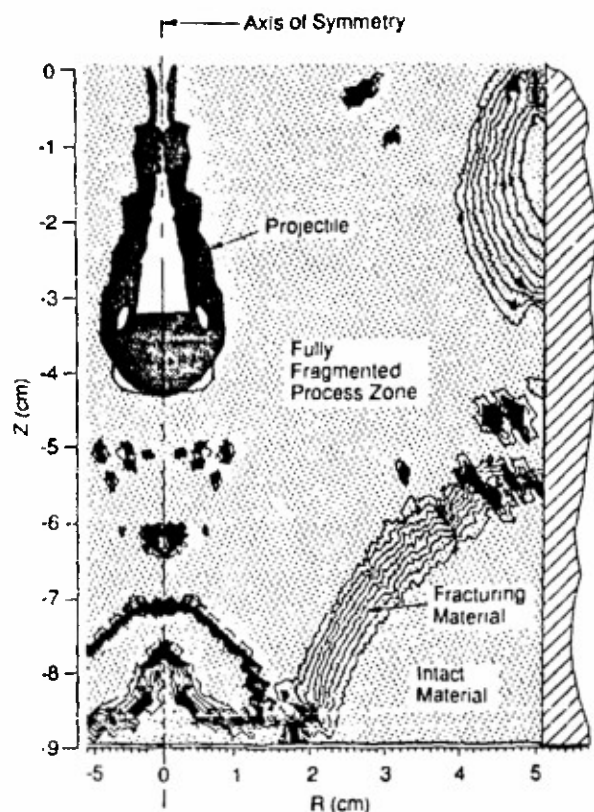
FIGURE 5

Computational result at 80 μs for penetration into AlN, showing intact, fracturing, and rubble regions.

5. CONCLUSIONS

The micromechanical model describing the processes of intergranular sliding, dilatancy, and compaction appears to be appropriate and useful for describing the highly nonlinear, anisotropic, and history-dependent deformation of fragmented beds. For the case of long rods penetrating ceramic armor, the model predicts that the intergranular friction governs the penetration depth. This result suggests that experiments such as the pressure-shear impact test of Shockey and Klopp[11] should be used to examine candidate ceramics for armor applications.

REFERENCES

1. J. T. Jenkins and M. Satake, Eds., Mechanics of Granular Materials, Proc. U.S./Japan Seminar on New Models and Constitutive Relations in the Mechanics of Granular Materials, Ithaca, NY, Aug. 23-27, 1982 (Elsevier, 1983).

2. M. Isida and S. Nemat-Nasser, Acta. Metall. 35 (1987) 2887.

3. S. Nemat-Nasser and M. Obata, Trans. ASME 55 (1988) 24.

4. M. Satake and J. T. Jenkins, Eds., Mechanics of Granular Materials, Proc. U.S./Japan Seminar on the Micromechanics of Granular Materials, Sendai-Zao, Japan, Oct. 26-30, 1987 (Elsevier, 1988).

5. C. C. Chang and A. Misra, J. Eng. Mech., 115 (1989) 704.

6. E. Orowan, Proc. Roy. Soc. London 52 (1940) 23.

7. D. R. Curran and L. Seaman, Final Technical Report to the Office of Naval Research, Contract N0014-88-C-0734 (October 1990).

8. M. M. Carroll and A. C. Holt, J. Appl. Phys. 43 (1972) 1626.

9. H. C. Heard and C. F. Cline, J. Mat. Sci. 15 (1980) 1889.

10. J. Lankford, private communication to R. Klopp at SRI (November 1989).

11. D. A. Shockey and R. Klopp, Tests for Determining Failure Criteria of Ceramics under Ballistic Impact, Quarterly Progress Report No. 2, by SRI for U.S. Army Research Office (January 1990).

**ANALYSIS OF TILT IN THE HIGH-STRAIN-RATE
PRESSURE-SHEAR PLATE IMPACT EXPERIMENT**

Analysis of tilt in the high-strain-rate pressure-shear plate impact experiment

Richard W. Klopp
Poulter Laboratory, SRI International, Menlo Park, California 94025

Rodney J. Clifton
Division of Engineering, Brown University, Providence, Rhode Island 02912

An analysis is presented of the effect of tilt in the high-strain-rate pressure-shear plate impact experiment. Normal and shear tractions and the velocity difference across the specimen are obtained from free-surface particle velocity, tilt angle, closure direction, and impact velocity data. The effect of tilt in high-strain-rate pressure-shear plate impact is shown to be small unless the velocity difference across the specimen is itself small.

The effect of tilt in experiments involving either normal impact or pressure-shear impact of two parallel plates has been analyzed.[1,2] No results have been presented however, on the effect of tilt in the high-strain-rate pressure-shear plate impact experiment, shown in Fig. 1,[3] in which a thin-specimen plate is compressed and sheared between hard, elastic flyer and target plates, and the stress and strain rate in the specimen are inferred from particle velocity measurements at the back of the target. Because of the tilt, the waves generated are inclined with respect to the plate surfaces. In this communication, an analysis is presented of the effect of the inclination of these waves on the calculation of stress, strain, and strain rate in the specimen.

Figure 2(a) shows the pattern of waves generated during tilted impact. The specimen is idealized as a sliding interface of zero thickness. The flyer and target are taken to be linear elastic. The x_1 direction is normal to the impact plane, and the x_2 direction is in the direction of closure. The angle from the x_3 direction to the shearing direction is denoted by Ω [Fig. 2(b)]. With an assumed supersonic closure, a normal (p) wave is generated in the target at angle ψ_1 and two shear (sv,sh) waves as generated at angle ψ_2. For small angles, $\psi_i \approx \alpha c_i/u_0$, where α is the tilt angle, c_i is the wave speed, and u_0 is the component of impact velocity normal to the plates. For a typical pressure-shear experiment, $\alpha = 10^{-3}$ rad, $u_0 = 200$ m/s, and $c_1 = 6000$ m/s, and so $\psi_1 \approx 30 \times 10^{-3}$ rad $\approx 1.7°$.

In the interpretation of the experiments, the measured normal and transverse particle velocities in region 9 are related to the stresses and particle velocities in regions 3 and 4. Let $p^{i,j}$ be the unit polarization vector of the wave traveling in to region i from region j. Let $[u]^{i,j}$ designate the jump in u from regions i to j: $[u]^{i,j} = u^i - u^j$. The usual subscripts designate vector and tensor components. The particle velocity is v and the stress is σ. The jump in particle velocity across a

wave front can be expressed as follows:

$$[v]^{i,j} = |[v]^{i,j}|p^{i,j} = A^{i,j}p^{i,j}, \tag{1}$$

where $A^{i,j}$ are amplitudes to be determined. For isotropic materials, the polarization vectors are normal to the wave front for p waves propagating at speed c_1 and parallel to the wave front for sv and sh waves propagating at speed c_2. For a wave propagating in the direction n in the x_1-x_2 plane at a counterclockwise angle θ from the positive x_1 axis, the three polarizations are

$$\mathbf{p}^p = \begin{Bmatrix} \cos\theta \\ \sin\theta \\ 0 \end{Bmatrix}, \quad \mathbf{p}^{sv} = \begin{Bmatrix} -\sin\theta \\ \cos\theta \\ 0 \end{Bmatrix}, \quad \mathbf{p}^{sh} = \begin{Bmatrix} 0 \\ 0 \\ 1 \end{Bmatrix}, \tag{2}$$

for the p wave, the sv wave, and the sh wave, respectively.

The respective polarization vectors for the stresses are given by

Laser Interferometer
Particle Velocity Diagnostics
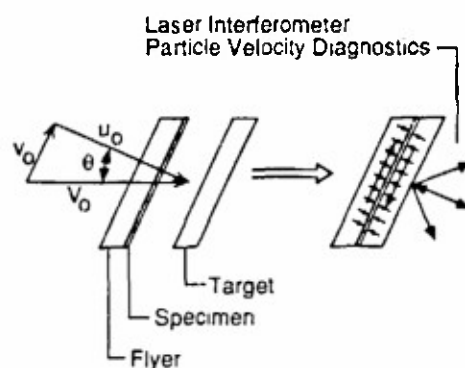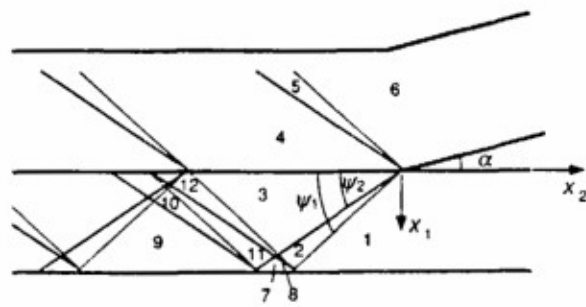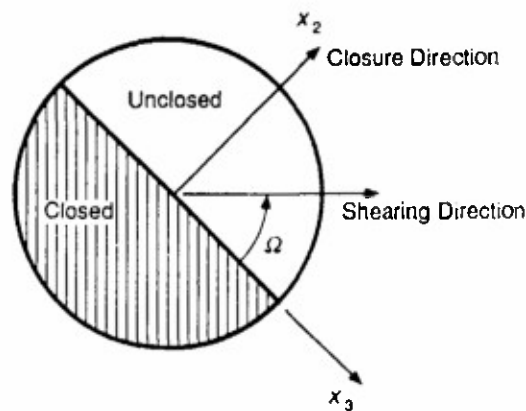
Target
Specimen
Flyer

FIG. 1. Schematic of the high-strain-rate pressure-shear plate impact experiment.

(a)

(b)

FIG. 2 Schematic of tilted impact of inclined plates. (a) Wave pattern generated. (b) Orientation of closure direction relative to shearing direction.

$$
\mathbf{s}^p = -\rho c_1 \left\{ \begin{array}{c} 1 - 2\eta^2 \sin^2 \theta \\ 1 - 2\eta^2 \cos^2 \theta \\ 1 - 2\eta^2 \\ 0 \\ 0 \\ \eta^2 \sin 2\theta \end{array} \right\},
$$

$$
\mathbf{s}^{sv} = -\rho c_2 \left\{ \begin{array}{c} -\sin 2\theta \\ \sin 2\theta \\ 0 \\ 0 \\ 0 \\ \cos 2\theta \end{array} \right\}, \quad \mathbf{s}^{sh} = -\rho c_2 \left\{ \begin{array}{c} 0 \\ 0 \\ 0 \\ \sin \theta \\ \cos \theta \\ 0 \end{array} \right\}, \quad (3)
$$

where $[s_1,...,s_6]^T$ corresponds to $[\sigma_{11},\sigma_{22},\sigma_{33},\sigma_{23},\sigma_{13},\sigma_{12}]^T$, p is the flyer and target density, and $\eta = c_2/c_1$.

The stress and particle velocity in the various regions in Fig. 2(a) can be expressed as the sum of jumps across successive wave fronts. Thus

$$
\mathbf{v}^3 = \mathbf{v}^1 + A^{p1,2}\mathbf{p}^{p1,2} + A^{sv2,3}\mathbf{p}^{sv2,3} + A^{sh2,3}\mathbf{p}^{sh2,3},
$$

$$
(4)
$$

$$
\mathbf{v}^4 = \mathbf{v}^6 + A^{p6,5}\mathbf{p}^{p6,5} + A^{sv5,4}\mathbf{p}^{sv5,4} + A^{sh5,4}\mathbf{p}^{sh5,4}.
$$

The surface tractions on the two sides of the specimen are given by similar relations, with σ_{11}, σ_{12}, and σ_{13} replacing v_1, v_2, and v_3 and s_1, s_6, and s_5 replacing p_1, p_2, and p_3, respectively.

Tractions are expected to be continuous across the boundary between regions 3 and 4 once sufficient wave reflections have occurred to establish a homogeneous stress state in the specimen. The flyer and target are initially stress free and the target is at rest. Thus

$$
A^{p1,2}s_1^{p1,2} + A^{sv2,3}s_1^{sv2,3} + A^{sh2,3}s_1^{sh2,3} - A^{p6,5}s_1^{p6,5}
$$
$$
- A^{sv5,4}s_1^{sv5,4} - A^{sh5,4}s_1^{sh5,4} = 0
$$

$$
A^{p1,2}s_6^{p1,2} + A^{sv2,3}s_6^{sv2,3} + A^{sh2,3}s_6^{sh2,3} - A^{p6,5}s_6^{p6,5}
$$
$$
- A^{sv5,4}s_6^{sv5,4} - A^{sh5,4}s_6^{sh5,4} = 0 \quad (5)
$$

$$
A^{p1,2}s_5^{p1,2} + A^{sv2,3}s_5^{sv2,3} + A^{sh2,3}s_5^{sh2,3} - A^{p6,5}s_5^{p6,5}
$$
$$
- A^{sv5,4}s_5^{sv5,4} - A^{sh5,4}s_5^{sh5,4} = 0.
$$

The normal velocity and the transverse velocity perpendicular to the shearing direction are expected to be continuous across the specimen. Thus

$$
A^{p1,2}p_1^{p1,2} + A^{sv2,3}p_1^{sv2,3} + A^{sh2,3}p_1^{sh2,3}
$$
$$
- A^{p6,5}p_1^{p6,5} - A^{sv5,4}p_1^{sv5,4} - A^{sh5,4}p_1^{sh5,4}
$$
$$
- v_1^6 = 0, \quad (6)
$$

$$
A^{p1,2}(p_2^{p1,2}\cos\Omega - p_3^{p1,2}\sin\Omega) + A^{sv2,3}(p_2^{sv2,3}\cos\Omega - p_3^{sv2,3}\sin\Omega) + A^{sh2,3}(p_2^{sh2,3}\cos\Omega - p_3^{sh2,3}\sin\Omega)
$$
$$
- A^{p6,5}(p_2^{p6,5}\cos\Omega - p_3^{p6,5}\sin\Omega) - A^{sv5,4}(p_2^{sv5,4}\cos\Omega - p_3^{sv5,4}\sin\Omega) - A^{sh5,4}(p_2^{sh5,4}\cos\Omega - p_3^{sh5,4}\sin\Omega)
$$
$$
- v_2^6 \cos\Omega + v_3^6 \sin\Omega = 0. \quad (7)
$$

The velocity in the shearing direction is expected to have a jump across the specimen of γh, where γ is the shearing rate to be determined and h is the specimen thickness. Thus

$$
A^{p1,2}(p_2^{p1,2}\sin\Omega + p_3^{p1,2}\cos\Omega) + A^{sv2,3}(p_2^{sv2,3}\sin\Omega + p_3^{sv2,3}\cos\Omega) + A^{sh2,3}(p_2^{sh2,3}\sin\Omega + p_3^{sh2,3}\cos\Omega)
$$
$$
- A^{p6,5}(p_2^{p6,5}\sin\Omega + p_3^{p6,5}\cos\Omega) - A^{sv5,4}(p_2^{sv5,4}\sin\Omega + p_1^{sv5,4}\cos\Omega) - A^{sh5,4}(p_2^{sh5,4}\sin\Omega + p_3^{sh5,4}\cos\Omega)
$$
$$
- v_2^6 \sin\Omega - v_3^6 \cos\Omega = \gamma h. \quad (8)
$$

Equations (5)–(8) relating tractions and particle velocities on the two sides of the specimen provide six equations for relating the six unknown amplitudes $A^{p1,2}$, $A^{sv2,3}$, $A^{sh2,3}$, $A^{p6,5}$, $A^{sv5,4}$, and $A^{sh5,4}$, and the unknown velocity jump γh.

A seventh equation is obtained by relating the wave amplitudes to the free-surface velocity measured in region 9:

$$\mathbf{v}^9 = \mathbf{v}^1 + A^{p1,2}\mathbf{p}^{p1,2} + A^{sv2,3}\mathbf{p}^{sv2,3} + A^{sh2,3}\mathbf{p}^{sh2,3} + A^{p2,8}\mathbf{p}^{p2,8} + A^{sv8,7}\mathbf{p}^{sv8,7} + A^{sh8,7}\mathbf{p}^{sh8,7} + A^{p11,10}\mathbf{p}^{p11,10}$$
$$+ A^{sv10,9}\mathbf{p}^{sv10,9} + A^{sh10,9}\mathbf{p}^{sh10,9}. \tag{9}$$

Equation (9) contains six additional amplitudes, $A^{p2,8}$, $A^{sv8,7}$, $A^{sh8,7}$, $A^{p11,10}$, $A^{sv10,9}$ and $A^{sh10,9}$, which can be eliminated by considering diffraction at the target free surface.[4] Diffraction of the 1,2 p wave from the target free surface provides three relations for the amplitudes $A^{p2,8}$, $A^{sv8,7}$, $A^{sh8,7}$, and $A^{p1,2}$. Similarly, diffraction of the 2,3 sv and sh waves from the rear surface provides three relations for the amplitudes $A^{p11,10}$, $A^{sv10,9}$, $A^{sh10,9}$, $A^{sv2,3}$, and $A^{sh2,3}$. For $\alpha \approx \sin\alpha$, application of these relations to Eq. (9) gives

$$A^{p1,2}\left[p_2^{p1,2}\sin\Omega + p_3^{p1,2}\cos\Omega - p_2^{p2,8}\sin\Omega - p_3^{p2,8}\cos\Omega - 4\eta\psi_1(p_2^{sv8,7}\sin\Omega + p_3^{sv8,7}\cos\Omega)\right]$$
$$+ A^{sv2,3}\left[p_2^{sv2,3}\sin\Omega + p_3^{sv2,3}\cos\Omega + 4\eta\psi_2(p_2^{p11,10}\sin\Omega + p_3^{p11,10}\cos\Omega) - p_2^{sv10,9}\sin\Omega - p_3^{sv10,9}\cos\Omega\right]$$
$$+ A^{sh2,3}\left[p_2^{sh2,3}\sin\Omega + p_3^{sh2,3}\cos\Omega + p_2^{sh10,9}\sin\Omega + p_3^{sh10,9}\cos\Omega\right] = v_2^9\sin\Omega + v_3^9\cos\Omega, \tag{10}$$

where $v_2^9\sin\Omega + v_3^9\cos\Omega$ is the measured transverse velocity. From Eqs. (5)–(8) and (10), $\dot{\gamma}h$ and the unknown amplitudes can be obtained from the measured velocity components in region 9 and the projectile velocity of region 6. The tractions on the specimen can then be evaluated from relations analogous to those of Eqs. (4).

As an illustration of the above analysis, consider an example in which an AlN specimen (thickness $h = 0.577$ mm) is impacted between B_4C flyer and target plates ($\rho = 2.51$ g/cm^3, $c_1 = 13.8$ mm/μs, $c_2 = 8.5$ mm/μs) at a skew angle of $\theta = 20°$. The impact velocity is $V_0 = 672$ m/s, and the tilt is $\alpha = 4$ mrad. Closure occurs nominally in the shearing direction, with $\Omega = 97°$. The average target free-surface transverse velocity is 167 m/s. From these data, the wave amplitudes and $\dot{\gamma}h$ can be obtained from Eqs. (5)–(8) and (10), resulting in a shearing rate of 1.13×10^5 s^{-1}. From the amplitudes, one calculates a specimen normal stress of -10.938 GPa and a specimen shear stress of 1.776 GPa. If no tilt correction is made,[5] then one obtains a normal stress of -10.945 GPa, a shear stress of 1.781 GPa, and a shearing rate of 1.09×10^5 s^{-1}. The maximum error of approximately 3.5% is in the shearing rate.

The magnitude of the error depends on Ω. If Ω is 0° so that the shearing is normal to the closure direction, the motion used to derive the shear stress and shearing rate is carried by sh waves uncoupled from the p waves. Thus a tilted normal wave has little effect on the shear stress and shearing rate. When Ω is near $\pm 90°$, most of the motion used to derive the shear stress and shearing rate is carried by sv waves coupled to the p waves by diffraction. In this case, the error is still small but is larger than in the $\Omega = 0°$ case. If one sets $\Omega = 0°$ in the example, then one obtains a shear stress of 1.779 GPa from which the uncorrected value of 1.781 GPa differs by only 0.1%, and the corrected and uncorrected shearing rates are identical.

The errors are small, even in large-tilt case considered in the example, because the excess x_2 component of the free-surface velocity is the same as the excess x_2 component of the flyer velocity that is approximately the x_1 component of flyer

velocity v_1^6 multiplied by the tilt angle. The contribution of αv_1^6 to the free-surface transverse velocity is usually small. In cases in which the shearing rate is low, however, contributions of αv_1^6 to the free-surface transverse velocity $v_{fs} = v_2^9\sin\Omega + v_3^9\cos\Omega$ can lead to large relative errors in the shearing rate. This effect can be made evident by considering the fractional derivative of the equation for the shearing rate which, for $\alpha = 0$, becomes

$$\frac{d\dot{\gamma}}{\dot{\gamma}} = \frac{-dv_{fs}}{v_0 - v_{fs}},$$

where $v_0 = v_2^6\sin\Omega + v_3^6\cos\Omega$. If the $v_0 - v_{fs}$ is small, $d\dot{\gamma}/\dot{\gamma}$ could be large.

The tilt error in high-strain-rate pressure-shear plate impact has been shown to be small except when the shearing rate is low. The above example shows that the excess target free-surface transverse motion induced by the tilt is very small. Because the transverse momentum resulting from flyer tilt is very small, the small effect of the tilt on the transverse motion of the target free surface is not unexpected.

[1]K. S. Kim and R. J. Clifton, J. Mater. Sci. 19, 1428 (1984).

[2]Y. M. Gupta, "Theoretical and Experimental Studies to Develop a Piezoelectric Shear Stress Interface Gage," SRI International Technical Report DNA-TR-84-342 prepared on Contract Nos. DNA 001-80-C-0145 and DNA 001-82-C-0297 (Defense Nuclear Agency, Washington, DC, 1984).

[3]R. J. Clifton and R. W. Klopp, *Metals Handbook*, 9th ed (ASM International, Metals Park, OH, 1985), Vol. 8, p. 230.

[4]See, for example, J. D. Achenbach, *Wave Propagation in Elastic Solids* (North Holland, Amsterdam, 1973), p. 168ff.

[5]One way is to simply let $\psi_i = 0$ in Eq. (5)–(8) and (10).

PRESENTATIONS

PRESENTATIONS

1. D. A. Shockey, R. W. Klopp, and D. R. Curran, "Tests for Determining Failure Criteria of Ceramics Under Ballsitic Impact," presented at the DoD/DARPA Coordination Meeting on Advanced Armor/Anti-Armor Materials and Advanced Computational Methods, Alexandria, Virginia, December 13-15, 1988.

2. D. A. Shockey, "Tests for Determining Failure Criteria of Ceramics Under Ballistic Impact," presented at the Review of BTI Program on Advanced Armor/Anti-Armor Materials, Alexandria, Virginia, November 8-9, 1989.

3. R. W. Klopp and D. A. Shockey, "Response of Aluminum Nitride to High Strain Rate Pressure-Shear Impact," presented at the 92nd Annual Meeting and Exposition of The American Ceramic Society, Dallas, Texas, April 22-26, 1990.

4. D. C. Erlich, "Adaptations to Existing Gas Guns to Increase Impact Velocity and Flyer Plate Diameter," presented at the 41st Meeting of the Aeroballistic Range Association, San Diego, California, October 22, 1990.

5. R. W. Klopp and D. A. Shockey, "Dynamic, High Pressure Failure Response of Silicon Carbide," presented at the 93rd Annual Meeting and Exposition of The American Ceramic Society, Cincinnati, Ohio, April 28-May 2, 1991.